APPLICATION OF GNSS PRECISE POINT POSITIONING TO LOW-COST HARDWARE FOR CM-LEVEL POSITIONING

PRAGATI BASNET

A THESIS SUBMITTED TO THE FACULTY OF GRADUATE STUDIES IN PARTIAL FULFILLMENT OF THE REQUIREMENTS FOR THE DEGREE OF

MASTER OF SCIENCE

GRADUATE PROGRAMME IN EARTH AND SPACE SCIENCE
YORK UNIVERSITY

TORONTO, ONTARIO

DECEMBER 2024

Abstract

Precise Point Positioning (PPP) offers high-precision GNSS positioning solutions. The advent of low-cost hardware provides an affordable alternative to costly geodetic-grade hardware, broadening the accessibility of high-precision positioning across many applications. However, this hardware produces measurements with higher noise levels, reduced multipath suppression, and lower carrier-to-noise density ratios (C/N_0), restricting its ability to achieve cm-level accuracy. This study addresses these limitations by developing a novel C/N_0-based empirical observation weighting model to accompany the signal characteristics of low-cost hardware. This model enhances positioning accuracy by emphasizing high-quality signals above a nominal C/N_0 threshold and down-weighting observations below it. The proposed model reduces float to carrier-phase integer ambiguity resolution (fixed) convergence time by 71% for 5 cm and 38% for 2.5 cm horizontal error thresholds for the static dataset tested, demonstrating the potential of low-cost GNSS devices as viable, high-precision positioning solutions.

Acknowledgements

Throughout my life, many teachers have recognized and nurtured the potential in me, even when I couldn't see it myself. Their faith and encouragement have created a deep sense of connection and respect. Among them, Professor Sunil Bisnath stands out as an inspiring figure. His expertise and rigour in research, combined with his kindness and sense of humour, have left a lasting impact and set a standard I deeply admire. I am sincerely grateful to him and all my professors for their invaluable support and the opportunity to pursue my dreams.

I also want to extend my heartfelt gratitude to Professor Spiros Pagiatakis for his insightful comments, guidance, and thoughtful suggestions throughout this journey. His expertise and invaluable feedback have significantly enriched my research, and our discussions provided clarity and depth that have been instrumental to my work. Those discussions during the REC were my motivations to boost my limits.

In addition, I am deeply grateful to the members of the York GNSS Lab, who became like family and enriched my journey with their support, diverse perspectives, and invaluable research discussions. Thanks to Sudha, Nacer, Anurag, Ding, Jiahuan, Sihan, Soroush, Sandesh, Ben, Sogand, Narin, Caitlyn, Lingmin, and Jihang- I will always cherish the memories and camaraderie we have shared. I am especially thankful for the last-minute support from Ding, Lingmin, and Caitlyn, which I will never forget.

I am deeply grateful to my family, whose unwavering support has been the foundation of my journey. To my husband, thank you for your patience, love, and sacrifices, which made this accomplishment possible. And to my young daughter, whose joyful spirit has been my constant motivation, thank you for being my light through it all.

Table of Contents

List of Tables

List of Figures

List of Acronyms

AC	Analysis Centre
AGC	Automatic Gain Control
ANTEX	ANTenna Exchange
APC	Antenna Phase Centre
AR	Ambiguity resolution
ARP	Antenna Reference Point
C/A	Coarse Acquisition
CMC	Code-Minus-Carrier
DCB	Differential Code Bias
DCM	Decoupled Clock Model
DGNSS	Differential Global Navigation Satellite System
DOY	Day Of Year
ECEF	Earth-Centred Earth-Fixed
EOP	Earth orientation parameter
FCB	Fractional Cycle Baises
GLONASS	GLObal NAvigation Satellite System
GMF	Global Mapping Function
GNSS	Global Navigation Satellite System
GPS	Global Positioning System
IF	Ionosphere-Free
IGR	IGS Rapid

IGS	International GNSS Service
IRC	Integer Recovery Clock
ITRF	International Terrestrial Reference Frame
LAMBDA	Least-squares AMBiguity Decorrelation Adjustment
MLAMBDA	Modified LAMBDA
NLOS	Non-Line of Sight
NRTK	Network RTK
OSB	Observable-Specific signal Biases
PCO	Phase Centre Offset
PCV	Phase Centre Variation
PDOP	Position Dilution of Precision
PLL	Phase Lock Loop
PNT	Positioning, Navigation, and Timing
PPP	Precise Point Positioning
PRN	Pseudo-Random Number
RF	Radio Frequency
rms	Root Mean Square
RTK	Real-Time Kinematics
TGD	Time Group Delay
ZHD	Zenith Hydrostatic Delay
SNR	Signal-to-Noise Ratio

Chapter 1 Introduction

Global Navigation Satellite System (GNSS)-based precise positioning has become essential in applications requiring high accuracy, such as geodetic surveying, autonomous vehicle navigation, precision agriculture, and geoscientific research. GNSS systems provide positioning, navigation, and timing (PNT) services through constellations of satellites broadcasting signals to GNSS receivers on or above the Earth's surface. Precise positioning aims to achieve accuracy at the centimetre or even millimetre level. This chapter explores GNSS positioning techniques in detail, outlines the research problem, and discusses the study's contributions and significance.

1.1 Overview of advanced GNSS-based positioning techniques

The evolution of Global Navigation Satellite Systems (GNSS) from the initial transit system to today's multi-constellation framework marks a significant technological achievement, with global navigation and timing now available to users worldwide. The integration of multiple constellations, advanced augmentation systems, and ongoing modernization ensures that GNSS can support a diverse range of applications with high accuracy and reliability.

GNSS signals propagate at the speed of light, operating within the L-band radio frequency spectrum, especially between 1.2 and 1.6 GHz. The reason for choosing L-band frequency ranges is that they allow for precise measurements with simple instruments and maintain signal integrity under normal atmospheric conditions. The wavelength for a GNSS signal at this frequency is approximately 19-25 cm (Teunissen & Montenbruck, 2017a, p. 5). Pseudorange, carrier-phase, and Doppler observation are foundational data for calculating position, velocity, and the receiver's time offset. Pseudorange measures the time delay from signal transmission to reception, providing satellite-receiver distance. Carrier-phase is the range between the satellite and receiver measured by tracking the difference in phase between transmitting and receiving oscillators. Doppler measurements are the measure of line-of-sight velocity. These measurements are complemented by the broadcast navigation message, which includes the GNSS satellite's orbit and clock offsets. This information lets the receiver calculate the transmitting satellite's position and velocity at signal transmission time. The GNSS framework allows GNSS receivers to calculate their positions by trilaterating multiple satellite signals. To determine position accurately, the receiver needs four simultaneously observed pseudorange measurements to solve for four unknowns: the three coordinates of position and clock bias (Hofmann-Wellenhof et al., 2007, p. 4).

Each GNSS system operates independently but follows similar principles. The first GPS satellites were launched in the 1970s and have since become the most widely used GNSS globally. GLONASS, developed by Russia, is the second operational GNSS, while Galileo and BeiDou have emerged more recently, contributing additional coverage and signal redundancy to the global system. All GNSS constellations have space, control, and user segments. The space segment has the satellite constellation, which serves as a platform for atomic clocks, transmitters, and auxiliary systems, including solar panels and propulsion systems. Control stations include master control stations, monitoring stations for tracking, and ground antennas for satellite communication. The user segment encompasses different user categories, receiver types, and informational services.

GNSS has become indispensable across applications, delivering precise positioning, navigation, and timing (PNT) information crucial to various sectors worldwide. High accuracy is achieved using two main techniques: relative positioning, commonly through real-time kinematic (RTK), and precise point positioning (PPP). RTK relies on a base station that continuously provides observed state representation (OSR) corrections, based on pseudorange and carrier-phase measurements, to a rover in real-time (van Diggelen, 1997). However, the performance and reliability of RTK decrease as the distance between the base and the rover increases. To overcome this limitation, Network RTK (NRTK) extends the RTK concept using a network of base stations, which can interpolate corrections across a larger area. NRTK leverages the network to estimate various error components, including satellite orbits, clock biases, and atmospheric delays, transmitting these corrected states to the rover for improved positioning accuracy over larger regions. Despite this enhancement, NRTK's reliance on numerous fixed reference stations limits its applicability outside established networks, particularly in remote or poorly connected areas (Zumberge et al., 1997). This means that the performance of NRTK can be compromised in remote areas or areas with poor network coverage.

In contrast, PPP offers similar accuracy without needing a local base station by using precise satellite orbit and clock corrections. PPP is a state space solution that generates precise positioning using a single receiver, satellite orbit, and clock corrections from global reference stations regardless of the region (Zumberge et al., 1997). Therefore, PPP is a cost-effective and attractive alternative. However, it has the drawback of long convergence times due to the high number of parameters that need estimation. Meanwhile, extensive research on this technique has proven that ambiguity resolution is crucial to reducing convergence time and reaching RTK-like performance (Collins, 2008; Naciri & Bisnath, 2021), overcoming the hurdle of longer convergence time. These results have now made PPP a reliable approach.

Geodetic hardware is traditionally known for delivering highly accurate measurements essential for critical tasks where errors at the mm- or cm-level are intolerable. However, in recent years, low-cost GNSS receivers have undergone transformative advancements, expanding their capabilities beyond basic navigation. Early GNSS devices were limited to single-frequency signals from the GPS constellation, but modern low-cost receivers now integrate multi-frequency and multi-constellation support (Aggrey et al., 2021). These advancements have unlocked new possibilities for employing low-cost hardware in applications that require precise positioning.

1.2 Problem statement

Despite the superior positional accuracy of RTK positioning systems, their high cost significantly limits accessibility for budget-constrained applications. This challenge is particularly pronounced in rugged terrain, such as hills and mountains, where extending RTK networks can be costly and resource intensive. One promising, cost-effective solution is PPP, which eliminates the need for extensive ground infrastructure by relying solely on satellite-based corrections to achieve high positional accuracy. Advances in multi-frequency and multi-constellation GNSS have enhanced PPP, enabling it to achieve rapid convergence to cm-level accuracy when using high-cost geodetic-grade hardware (Naciri & Bisnath, 2021, 2023). Low-cost hardware, though traditionally used in applications like resource tracking, fleet management, and basic surveying, now possesses the potential to be utilized in precise positioning applications due to advancements in multi-frequency and multi-constellation tracking capabilities. These technological improvements are narrowing the gap between low-cost and geodetic-grade receivers, offering cost-sensitive solutions for applications where cm-level accuracy was previously unattainable with low-cost devices. However, with low-cost hardware, achieving cm-level accuracy remains challenging due to increased measurement noise and reduced multipath suppression capabilities inherent to low-cost hardware components (Romero-Andrade et al., 2021).

A well-tuned stochastic model can minimize the effects of noise and multipath on the adjustment process by weighting observations based on the quality and reliability of incoming signals (B. Li et al., 2008; Yuan et al., 2022). High-end geodetic receivers typically benefit from models that account for signal elevation angles. This approach assumes that higher-elevation satellites provide higher-quality signals as the noise and multipath effects inherent to the GPS signal increase toward the horizon (Collins & Langley, 1999). Researchers in low-cost GNSS hardware studies have often applied the same elevation-based stochastic models used for high-end receivers (Cui et al., 2017; Wielgocka et al., 2021; Marut et al., 2024). However, for ultra-low-cost devices like smartphones, studies have revealed the correlation of noise and multipath with carrier-to-noise density ratio rather than elevation angles (Banville et al., 2019). Consequently, the potential of the C/N_0-based weighting scheme is explored (Shinghal & Bisnath, 2021).

Comparative studies have been conducted on low-cost hardware to assess signal quality differences with high-end geodetic hardware. The low-cost hardware exhibits a significantly lower carrier-to-noise density ratio (C/N_0) compared to geodetic receivers, with an average difference of 7.2 dB Hz. This disparity is observed approximately 98.9% of the time (Wielgocka et al., 2021). Additionally, measurements from low-cost hardware exhibit approximately two times higher multipath than geodetic hardware, with deviation reaching up to a metre. There is a significant signal quality issue, as multipath in geodetic grade hardware are typically up to decimeters (Hamza et al., 2023). Applying the same observation weighting scheme design for geodetic hardware across devices with differing signal fidelity leads to compromised positioning accuracy as the model does not adequately capture the variance in signal quality evident in hardware. Observation weighting schemes rely on the variance-covariance matrix (VCM), where variance must include all unmodelled effects and is affected by factors such as tracking loop behaviour, the performance of receiver and antenna components, signal quality, receiver dynamics, multipath, and atmospheric delays. These factors directly influence how observation weights are assigned, with higher weights given to observations with higher precision and reliability. Therefore, a dedicated study is necessary to develop a PPP observation model for low-cost hardware observation that accurately reflects the signal quality and supports cm-level accuracy.

1.3 Research contributions and significance

The primary goal of this research is to obtain cm-level positioning using PPP with low-cost hardware. The key distinction of this study lies in its unique contributions to this objective. Unlike prior work, which often focuses on using the existing observation weighting model design for geodetic hardware, this study explicitly introduces a C/N_0-based empirical observation weighting model design for the measurement of low-cost hardware. This approach is novel because it directly links signal quality indicators like carrier-to-noise density ratio (C/N_0) to hardware performance, enabling a model that more accurately reflects the variances in low-cost measurements. By analyzing the C/N_0 distribution patterns from the observations of low-cost hardware, a C/N_0-based empirical observation weighting model was introduced. Furthermore, ambiguity resolution is applied, reducing convergence time and enhancing accuracy. The following three research questions lead to three contributions:

1. How does the measurement quality of low-cost GNSS hardware differ from that of high-end geodetic hardware?
2. Do current elevation-based and C/N$_0$-based weighting schemes adequately represent the quality of observations from low-cost GNSS devices?
3. Can low-cost hardware achieve cm-level positioning?

Contribution 1: Comparative analysis of low-cost and geodetic GNSS hardware performance

This research thoroughly compares the measurement from low-cost and geodetic GNSS hardware, focusing on key performance metrics like carrier-to-noise density ratio, code multipath and measurement noise, cycle slips, and data availability. Analyzing these metrics clarifies the differences in measurement quality, highlighting the performance of low-cost hardware. Comparing measurements from geodetic and low-cost devices is a foundational step in understanding and assessing new hardware capabilities, and it has been a common approach in academic research. Similarly, this research starts with understanding and differentiating the signal characteristics of different-grade hardware.

Significance: By comparing low-cost and geodetic GNSS hardware performance, this research identifies critical areas where low-cost devices fall short regarding signal quality and noise suppression capability. The comparative analysis highlights the need for customized stochastic models for low-cost devices.

Contribution 2: C/N$_0$-based empirical observation weighting scheme for low-cost GNSS hardware for cm-level positioning

The novel C/N$_0$-based empirical weighting scheme proposed in this study enhances GNSS observation processing for low-cost receivers. By strategically downweighing measurements with a C/N_0 below 44 dB Hz and emphasizing higher-quality signals, this scheme effectively minimizes the impact of the signal noise within the adjustment filter. The choice of 44 dB Hz as the critical C/N_0 threshold is grounded in theoretical signal detection limits. Research indicates that the minimum power level at which a GNSS signal can be reliably distinguished from noise is approximately -204 dBW/Hz, corresponding to a C/N_0 value of 44 dB Hz ((Hartinger & Brunner, 1999; Hofmann-Wellenhof et al., 2007, p. 86). This approach incorporates the empirical findings that most measurements from low-cost hardware exhibit a C/N_0 between 40-50 dB Hz. In contrast, geodetic-grade hardware typically captures stronger signals, with the majority falling between 50-60 dB Hz. Unlike traditional models, this scheme supports the inclusion of low-elevation observations (below 10°).

Using C/N_0 in observation weighting is well-established in academic research. Hartinger and Brunner (1999) and Luo et al. (2009) developed a C/N_0-based model for geodetic measurements, while Ng et al. (2020) and Sui et al. (2022) applied similar methods for smartphones. However, no specific weighting scheme has been designed for measurements from medium-grade, low-cost hardware. This study introduces a novel approach by leveraging carrier-to-noise density ratio to formulate an empirical C/N_0-based weighting method tailored to such hardware.

Significance: By addressing the typical distribution of C/N_0 density ratios in observations from low-cost receivers, this scheme balances the inclusion of weaker measurements with prioritizing reliable, high-quality measurements. It provides a refined approach to low-cost GNSS data processing, leading to cm-level positioning.

Contribution 3: Analysis of the C/N_0-based empirical model

This study contributes a rigorous comparative analysis of the proposed C/N_0-based empirical stochastic model with the available elevation-based and C/N_0-based analytical stochastic models to 2.5 cm and 5.0 cm errors.

Significance: This analysis underscores the relevance of the proposed C/N_0-based empirical stochastic model to established stochastic models. Additionally, it offers valuable insights into the factors influencing the model's performance, particularly the reasons behind cases that do not achieve cm-level accuracy.

Novelty: The novelty of this research is finding an enhanced C/N_0-based empirical stochastic model for the low-cost dataset.

The study is guided by the following objectives:

Primary objective: To achieve cm-level GNSS positioning with low-cost hardware using PPP techniques.

Secondary objectives

1) To assess and compare the quality of the raw GNSS measurements from low-cost and geodetic hardware, thereby understanding the signal quality discrepancies.
2) To evaluate the efficacy of existing elevation-based and C/N_0-based weighting schemes for low-cost devices.
3) To develop an improved stochastic weighting model that addresses low-cost hardware's signal quality characteristics.

1.4 Thesis outline

Chapter 2 explores GNSS-based positioning techniques in depth, detailing the foundations of relative positioning and PPP. It includes detailed discussions on mathematical modelling, error sources, and ambiguity resolution in PPP. The literature review further highlights the potential of low-cost GNSS hardware for precise applications. This foundation establishes the framework for further research into PPP with low-cost hardware.

Chapter 3 provides the details on the experimental setup and data collection processes for evaluating the observations from low-cost and geodetic GNSS hardware. The chapter concludes with a discussion of performance between the two hardware types, highlighting the limitations of low-cost GNSS receivers.

Chapter 4 provides a detailed discussion on the need and development of the C/N_0-based empirical stochastic model. The empirical model's effectiveness is demonstrated by comparing it against elevation-based and C/N_0-based analytical stochastic models.

Chapter 5 comprehensively evaluates the developed C/N_0-based empirical model, emphasizing its effectiveness in reaching 2.5 cm and 5.0 cm horizontal accuracy thresholds. Additionally, an in-depth examination is conducted on datasets that failed to meet the 2.5 cm accuracy threshold, discussing factors influencing these discrepancies.

Chapter 6 summarizes key findings and highlights the contribution of the C/N_0-based empirical model to enhancing low-cost GNSS performance for precise positioning applications. It also provides recommendations for future research directions.

Chapter 2 GNSS-based positioning techniques

GNSS has advanced the development of navigation and positioning. It offers various positioning and navigation modes ranging from the basic single-frequency, pseudorange-based method used in consumer devices to advance multi-frequency, carrier-phase-based methods that achieve cm to sub-cm accuracy for precise tasks. GNSS encompasses three primary positioning techniques: single-point positioning (SPP), relative point positioning, and precise point positioning, as shown in Figure 2.1.

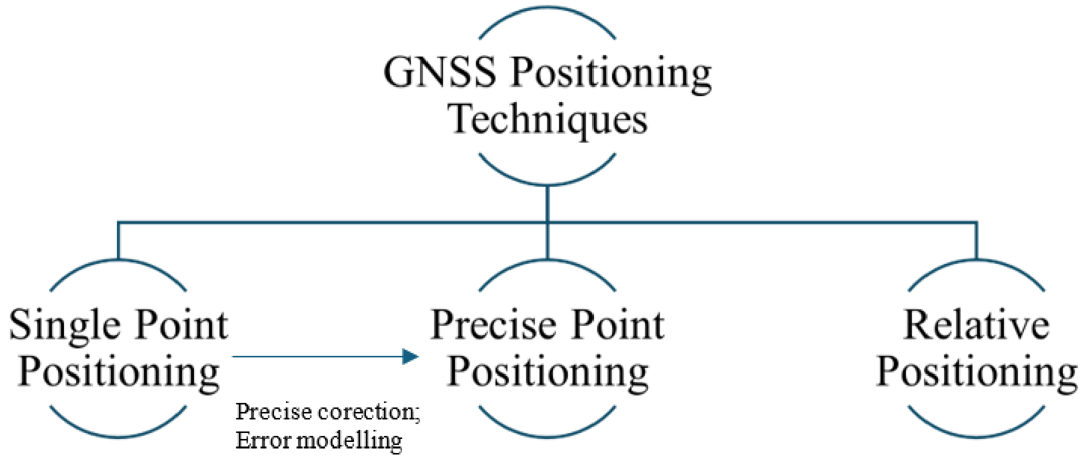

Figure 2.1: GNSS positioning techniques

2.1 Single Point Positioning (SPP)

SPP calculates the positioning of a receiver, solving single frequency pseudorange measurements with signals from at least four satellites using satellite positions and clock corrections derived from either the broadcast navigation message or precise IGS data. SPP solutions can also be based on dual or multi-frequency code measurements. Trilateration is applied to calculate the receiver's position, where each satellite's position is treated as the centre of a sphere, and the measured distance to each satellite (pseudorange) becomes the sphere's radius. The receiver's position is then calculated where these spheres intersect, allowing for location calculation through the overlap of distances to multiple satellites. The general pseudorange equation for SPP is simplified as:

$$\left.\begin{aligned}
P_s^1(t) &= \sqrt{(X^1 - X_r)^2 + (Y^1 - Y_r)^2 + (Z^1 - Z_r)^2} + c.d_{tr} + \varepsilon^1 \\
P_s^2(t) &= \sqrt{(X^2 - X_r)^2 + (Y^2 - Y_r)^2 + (Z^2 - Z_r)^2} + c.d_{tr} + \varepsilon^2 \\
P_s^3(t) &= \sqrt{(X^3 - X_r)^2 + (Y^3 - Y_r)^2 + (Z^3 - Z_r)^2} + c.d_{tr} + \varepsilon^3 \\
P_s^4(t) &= \sqrt{(X^4 - X_r)^2 + (Y^4 - Y_r)^2 + (Z^4 - Z_r)^2} + c.d_{tr} + \varepsilon^4
\end{aligned}\right\} \tag{2-1}$$

where $P_r^s(t)$ is the measured pseudorange between receiver r and satellite $s = 1,2,3,4$, (X^s, Y^s, Z^s) is satellite position at time t, and (X_r, Y_r, Z_r) is the receiver position. SPP provides 5-10 m accuracy, making it ideal for everyday tasks due to its simplicity and low cost (Teunissen & Montenbruck, 2017a, p. 623). In contrast, despite their higher costs and complexity, precise positioning techniques like RTK or PPP are used in fields requiring high accuracy, such as surveying, precision agriculture, environmental monitoring, and deformation analysis. Regarding precise positioning, RTK and PPP are industry-standard techniques that can achieve cm-level positioning. These methods utilize carrier-phase measurement to estimate the receiver positioning and differ in handling the error sources.

2.2 Relative positioning techniques

Relative positioning is a technique utilized in GNSS positioning to determine the location of the rover relative to the base station with a known position. It requires the use of two GNSS receivers. This process involves calculating the vector between these two points, commonly referred to as the baseline vector. The baseline vector provides the spatial relationship between the two points, allowing for high-precision positioning. The final output of the positioning process is the coordinates of the unknown point in a specified reference frame. If R is the reference (known) point, U is the unknown point, and b_{RU} is the baseline vector between them. The position vector X_R and X_U is coordinates of the reference and unknown points, respectively, and the relationship can be represented by:

$$\boldsymbol{X}_U = \boldsymbol{X}_R + \boldsymbol{b}_{RU} \tag{2-2}$$

The baseline vector b_{RU} components are:

$$\boldsymbol{b}_{RU} = \begin{bmatrix} X_U - X_R \\ Y_U - Y_R \\ Z_U - Z_R \end{bmatrix} = \begin{bmatrix} \Delta X_{RU} \\ \Delta Y_{RU} \\ \Delta Z_{RU} \end{bmatrix} \tag{2-3}$$

In relative positioning, the primary goal is to estimate the baseline vector $\boldsymbol{b}_{RU}$, which involves calculating the differences in coordinates between the two points. Once the baseline vector is accurately determined, the coordinates of the unknown point $\boldsymbol{X}_U$ can be obtained. Relative positioning requires observations from both the known and the unknown points, meaning the observation timestamps must match for both points. With simultaneous observations at two points R and U for satellites k and l , it is possible to create linear combinations, leading to single-differencing, double-differencing, and triple-differencing.

A single difference is formed by subtracting the observations of the same satellite made by two different receivers at the same epoch. Across-receiver differencing reduces satellite clock errors and similar biases, as the errors are nearly identical for both receivers at the same observation time. If the base station is (b) and the rover station is (r), then between receiver differencing can be obtained using:

$$\left.\begin{aligned}\Delta \mathrm{P}_{br,i}^{s} &= P_{b,i}^{s} - P_{r,i}^{s} = \Delta\rho_{br}^{s} + c\left(\Delta dt_{r,br}\right) + \gamma_i \Delta I_{br,1}^{s} + \Delta\, T_{br} + \Delta b_{rbr}, P_i + \Delta\epsilon P_{br,i} \\ \Delta \mathrm{L}_{br,i}^{s} &= L_{b,i}^{s} - L_{r,i}^{s} = \Delta\rho_{br}^{s} + c\left(\Delta dt_{r,br}\right) - \gamma_i \Delta I_{br,1}^{s} + \Delta\, T_{br} + \lambda_{\mathrm{i}}(\Delta N_{br,i}^{s} + \Delta b_{r_{r_{br,L_i}}}) + \Delta\epsilon P_{br,i}\end{aligned}\right\} \tag{2-4}$$

where Δ is the single-differencing between base (b) and receiver (r). Across-satellite differencing is useful for removing receiver clock errors, as the clock bias is common to both satellite observations when observations from a single station on two different satellites are differenced (Leick et al., 2015, p. 272).

A double difference is formed by taking the difference between two single differences of observations from two satellites observed by two receivers. In other words, a double difference is created when two receivers observed two satellites simultaneously or nearly so. Double differencing can be derived either from across-receiver or across-satellite differences. Assume that two different receivers simultaneously observe the same satellite. The measured pseudorange and carrier-phase observations from the base station b and the rover r can be expressed as:

$$\left.\begin{aligned}\nabla\Delta \mathrm{P}_{br}^{s} &= \nabla\Delta\rho_{br}^{js} + \gamma_i \nabla\Delta I_{br,1}^{js} + \nabla\Delta\, T_{br}^{js} + \nabla\Delta\epsilon_{Pi,br}^{js} \\ \nabla\Delta \mathrm{L}_{br}^{s} &= \nabla\Delta\rho_{br}^{js} - \gamma_i \Delta I_{br,1}^{js} + \nabla\Delta\, T_{br}^{js} + \lambda_{\mathrm{i}} \nabla\Delta N_{br,i}^{js} + \nabla\Delta\epsilon_{Li,br}^{js}\end{aligned}\right\} \tag{2-5}$$

where the subscript br is the single-differencing between the rover and the base station, and js is the double-differencing between the reference satellite j and s. The resulting double-differenced observations effectively eliminate receiver and satellite clock errors and hardware delays for both the receiver and satellite. One of the most significant advantages of double differencing is its ability to "cancel out" receiver and satellite clock errors and receiver and satellite hardware delays (Leick et al., 2015, pp. 273–274). Eliminating clock and hardware delays is particularly valuable in improving accuracy since the residual errors are minimal. This reduction is especially effective for ionospheric and tropospheric errors in short-baseline setups, where these errors tend to cancel due to spatial proximity.

2.3 Precise Point Positioning (PPP)

Precise Point Positioning allows for high-precision positioning using a single GNSS receiver by leveraging precise state space representation (SSR) corrections provided by the IGS analysis centre (Zumberge et al., 1997). Unlike relative positioning methods that rely on differential corrections from nearby base stations. PPP utilizes a network of global reference stations separated by tens to thousands of kilometres apart. The analysis centre uses these reference stations and leverages PPP processing by generating the precise orbit and clock correction necessary for accurate positioning (Dow et al., 2009; Griffiths & Ray, 2009). The International GNSS Service (IGS) coordinates the efforts of multiple analysis centres worldwide. Some prominent centres include the Centre for Orbit Determination in Europe (CODE), the Jet Propulsion Laboratory (JPL), the GeoForschungsZentrum (GFZ), the Centre National d'Etudes Spatiales (CNES), and Natural Resources Canada (NRCan).

PPP can be implemented in real-time and post-processed modes. Real-time PPP provides immediate positioning solutions by applying corrections as observations are received. Real-time PPP methods require access to real-time precise products. Real-time PPP is beneficial for applications such as marine navigation, airborne surveying, and precision agriculture (K. Chen, 2004; Ramachandran et al., 2019). Post-processed PPP involves applying corrections to stored GNSS data after collection. Users download precise products from the analysis centre after they become available, usually with some latency (e.g., final products are available after 12-18 days).

Post-processed PPP is suitable for applications where immediate results are not necessary, such as geodetic research and deformation monitoring(Gao & Shen, 2002; Choy, 2009).

Single-frequency PPP relies on observations from a single-frequency band, such as L1 for GPS. It uses ionospheric models to correct ionospheric delays (Choy, 2009). In contrast, dual-frequency PPP utilizes observations from two frequency bands, L1 and L2. Additionally, multi-frequency PPP extends the concept further by incorporating signals from multiple frequency bands across different GNSS constellations.

2.3.1 Mathematical model

The standard PPP models consist of both pseudorange and carrier-phase measurements. Considering receiver as r and satellites as s, using frequencies as f_i, i denoting the 1, 2, 3…, the standard PPP equation is provided. Notation of these state terms is taken from (Naciri & Bisnath, 2023).

$$\left.\begin{aligned} P^{s}_{r,i} &= \rho^{s}_{r} + c(\,dt_r - dt^{s}) + \gamma_i\, I^{s}_{1} + M^{s}_{r}.T_r + \left(b_{r,i} - b^{s}_{i}\,\right) + \varepsilon_{P_i} \\ \phi^{s}_{r,i} &= \rho^{s}_{r} + c(\,dt_r - dt^{s}) - \gamma_i\, I^{s}_{1} + M^{s}_{r}.T_r + \lambda_i(N^{s}_{i} + B_{r.i} - B^{s}_{i}) + \varepsilon_{\phi_i} \end{aligned}\right\} \tag{2-6}$$

where,

- $P^{s}_{r,i}$ is pseudorange measurements and $\phi^{s}_{r,i}$ is carrier-phase measurements,
- ρ^{s}_{r} is a geometric range between the receiver and satellite,
- c is the speed of light in a vacuum,
- dt_r is receiver clock offset and dt^{s} is satellite clock offset,
- γ_i is the ratio of the frequency applied to the first frequency ionosphere delay,
- I^{s}_{1} is ionosphere delay at first frequency,
- M^{s}_{r} is tropospheric wet delay mapping functions and T_r tropospheric delay,

- $b_{r,i}$ pseudorange receiver hardware bias and b_i^s is pseudorange satellite hardware bias,
- $B_{r.i}$ is receiver phase bias and B_i^s is satellite-related phase bias,
- λ_i is signal wavelength and N_i^s is integer ambiguity on frequency,
- ε_{P_i} residual unmodelled pseudorange error and ε_{ϕ_i} is a residual unmodelled phase error

Additionally, a dual-frequency ionospheric PPP model can be developed by extending the standard PPP equation.

$$\left.\begin{aligned} P_{IF}^s &= \rho_r^s + c(\,dt_r^* - dt^s) + M_r^s.T_r + \varepsilon_{P_i} \\ \phi_{IF,r}^s &= \rho_r^s + c(\,dt_r - dt^s) + \lambda_i(N_i^{s^*}) + \varepsilon_{\phi_i} \end{aligned}\right\} \tag{2-7}$$

States terms dt_r^* and $N_i^{s^*}$in Equation (2- 5) with * include the other quantities. This research uses one of the popular methods: the Decouple Clock Model (DCM) (Collins, 2008). DCM separates the pseudorange and carrier-phase clocks as it assumes that carrier-phase and pseudorange measurements do not maintain the same level of synchronization precision. Decoupling the clock leads to carrier-phase datum loss, which is recovered by selecting the reference satellites and setting their ambiguity to arbitrary values. It is later used for implicit differencing for other satellites. All estimated ambiguities are made relative to reference satellites.

The uncombined dual-frequency decoupled clock model (Seepersad, 2018) and uncombined triple-frequency decoupled clock model (Naciri & Bisnath, 2021) are the mathematical models used for the study. The triple-frequency model is derived from the dual-frequency model. The third frequency f_3 is included in the model. Considering receiver r and satellites s, the pseudorange and carrier-phase measurements on frequency $i, i \in 1,2,3, \ldots n$

$$\left.\begin{aligned}
P_1^s &= \rho_r^s + c\left(\overline{dt_r} - dt^s\right) + \gamma_1\overline{I_1^s} + M_r^s.T_r - b_1^s + \varepsilon_{P_1}\\
P_2^s &= \rho_r^s + c\left(\overline{dt_r} - dt^s\right) + \gamma_2\overline{I_1^s} + M_r^s.T_r - b_2^s + \varepsilon_{P_2}\\
p_3^s &= \rho_r^s + c\left(\overline{dt_r} - dt^s\right) + \gamma_3\overline{I_1^s} + M_r^s.T_r - IFB_r - b_3^s + \varepsilon_{P_3}\\
\phi_1^s &= \rho_r^s + c\left(\overline{\delta\, t_r} - dt^s\right) - \gamma_1\overline{I_1^s} + M_r^s.T_r + \lambda_1\left(\overline{N_1^s} - B_1^s\right) + \varepsilon_{\phi_1}\\
\phi_2^s &= \rho_r^s + c\left(\overline{\delta\, t_r} - dt^s\right) - \gamma_2\overline{I_1^s} + M_r^s.T_r + \lambda_1\left(\overline{N_2^s} - B_2^s\right) + \delta t_{12} + \varepsilon_{\phi_2}\\
\phi_3^s &= \rho_r^s + c\left(\overline{\delta\, t_r} - dt^s\right) - \gamma_3\overline{I_1^s} + M_r^s.T_r + \lambda_3\left(\overline{N_3^s} - B_3^s\right) + \delta t_{13} + \varepsilon_{\phi_3}
\end{aligned}\right\} \tag{2-8}$$

With: $c\overline{dt_r} = cdt_r + \frac{f_1^2}{f_1^2-f_2^2} b_{r,1}, 1 - \frac{f_2^2}{f_1^2-f_2^2} b_{r,2}$

$$c\overline{\delta t_r} = c\delta t_r + \lambda_1\left(\delta N_1^{ref} + B_{r,1}\right) - \frac{f_2^2}{f_1^2 - f_2^2}\left(b_{r,1} - b_{r,2}\right)$$

$$\overline{I_1^s} = I_1^s - \frac{f_2^2}{f_1^2 - f_2^2}\left(b_{r,1} - b_{r,2}\right)$$

$$\delta t_{1,2} = \lambda_2\left(\delta\, N_2^{ref} + B_{r,2}\right) - \lambda_1\left(\delta\, N_1^{ref} + B_{r,1}\right) - \left(b_{r,1} - b_{r,2}\right)$$

$$IFB_r = \frac{f_3^2 - f_1^2}{f_1^2 - f_2^2} b_{r,1} - \frac{f_3^2 - f_2^2}{f_1^2 - f_2^2} b_{r,2} + b_{r,3}$$

$$\delta t_{13} = \frac{f_2^2 - f_3^3}{f_1^2 - f_2^2}\left(b_{r,1} - br, 2\right) - \lambda_1\left(\delta N_1^{ref} + B_{r,1}\right) + \lambda_3\left(\delta N_3^{ref} + B_{r,3}\right)$$

$$\overline{N_1^s} = N_1^s - \delta N_1^{ref}$$

$$\overline{N_2^s} = N_2^s - \delta N_2^{ref}$$

$$\overline{N_3^s} = N_3^s - \delta N_3^{(ref)}$$

In equation (2-6), $IFB_{3,r}$ is Inter-Frequency pseudorange Biases (IFB) on the third frequency, estimated to be white noise. The pseudorange receiver clock and the ionospheric delays absorb the first and second frequency's receiver code biases. However, the third frequency's receiver biases must be estimated as an additional term. $\overline{N_1^s}$ is the integer single differenced ambiguity satellite s relative to the reference satellite. Compared to the dual-frequency model, pseudorange receiver biases are absorbed by additional receiver-dependent terms, and phase receiver biases are absorbed by carrier-phase-related bias terms (Naciri & Bisnath, 2023).

2.3.2 PPP error sources

Different sources of error impact the performance of PPP solutions. The errors impacting PPP solutions are systematic in nature and are mitigated either by modelling or by estimating. PPP error models need to be well understood. The details of these error sources are illustrated (Figure 2.2) and discussed in detail.

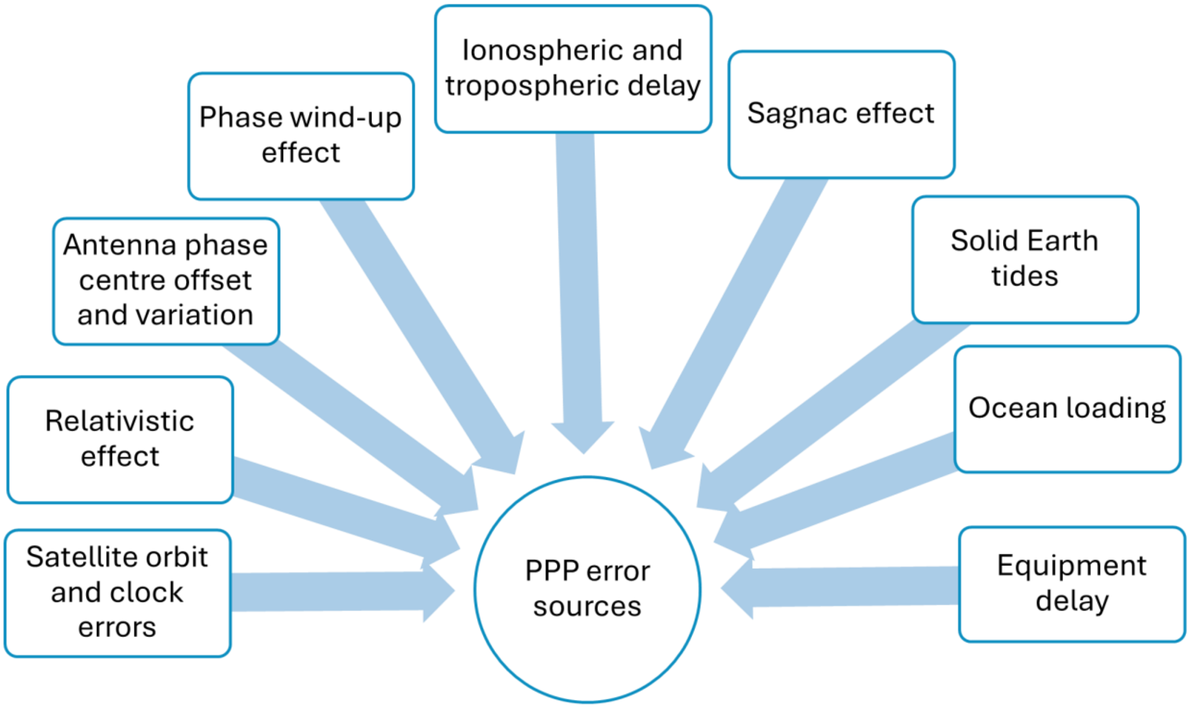

Figure 2.2: Different error sources in PPP estimates

2.3.2.1 Satellite orbit and clock errors

IGS centres provide satellite orbit and clock products. Broadcast ephemeris and IGS precise products are two categories of products available. The satellite's ephemeris is broadcast in a navigation message while disseminating a signal from the satellite to a receiver. However, the broadcast satellite orbit and clock are not precise enough for high-accuracy applications.

Therefore, using precise orbit and clock data is essential for achieving precise positioning in PPP.

The official combined products from the IGS are available in three categories for satellite orbit and clock data: IGS final products, IGS rapid products, and IGS ultra-rapid products (https://igs.org/products/). Table 2.1 provides a brief summary of satellite orbits and products and their accuracy. The update frequency of these corrections is typically every 5 minutes for orbits and every 30 seconds for the clock (Prange et al., 2020). The current final clock products have a rms error of 75 ps (IGS, 2024).

Table 2.1 Satellite orbit and clock product summary for GPS (IGS, 2024)

Product Type	Description	Latency	Update frequency	Typical accuracy
IGS final products	▪ Combined precise satellite orbits and clock corrections ▪ Earth orientation parameters	12-19 days	every Friday	orbits: ~2.5 cm clocks: ~75 ps (picoseconds)
IGS rapid products	▪ Combined precise satellite orbits and clock corrections ▪ Earth orientation parameters	~17-41 hours	at 17 UTC daily	orbits: ~2.5 cm clocks: ~75 ps
IGS ultra-rapid products	▪ Combined precise satellite orbits and clocks (half observed, half predicted) Earth orientation parameters	Predicted: real time; observed: 3-9 hours	at 03, 09, 15, 21 UTC	observed orbits/clocks: ~3 cm/1.5 ns SDev predicted orbits/clocks: ~5 cm / 150 ps
Broadcast	▪ Combined precise satellite orbits and clocks	real time	-	orbits: ~100 cm clocks: ~5ns

2.3.2.2 Relativistic effect

Relativistic effects arise from Albert Einstein's theory of relativity, introduced in 1905. This theory states that time synchronization is impossible in a rotation frame, which necessitates the synchronization of the clocks in the non-rotating frame. In GNSS, continuous relativistic corrections are required to address the impact of relative motion between satellites and the receiver. Due to relativistic effects, the satellite's clock rate appears offset when viewed from Earth; hence, satellite fixed offset is pre-corrected in satellite clock products, ensuring that signals are received at the correct frequencies on Earth without requiring adjustment from the user. However, users must calculate a periodic correction component by utilizing parameters broadcast in the satellite ephemeris or by using the satellite's position and velocity data. Accounting for these relativistic effects is essential when aiming for cm-level positioning accuracy. A detailed description and the corresponding adjustment relationships are provided in Ashby (2003).

2.3.2.3 Antenna phase centre offset and variations

In GNSS, the signals are broadcast from the phase centre of satellite antennas, but in estimation with a global network, the satellites' centres of mass are used as reference points. Therefore, users must apply a correction to account for the lever arm distance between the satellite's center of mass and its antenna phase center. Similarly, the lever arm between the antenna reference point (ARP) and the antenna phase centre (APC) should be considered. The ARP is typically a well-defined, fixed point on the antenna, while the APC is where the actual signal measurements are made. These two points' differences can introduce ~ 5 mm of variation in position calculations. The IGS releases satellite antenna phase offsets and variations in the international terrestrial reference frame (ITRF 2005) (Schmid et al., 2007). The precise lever arm values for the satellite and receiver are documented and made available through the standard ANTenna Exchange (ANTEX) format (Schmid et al., 2007).

Correction for the phase centre offsets (PCO) must also be done in the receiver. PCO is not fixed and can vary based on the antenna design and the elevation angle of the incoming signals (Hofmann-Wellenhof et al., 2007, p. 148). This variation means different satellites can contribute differently to the measured position, mainly when signals come from low elevation angles. For geodetic antennas, PCV can be smaller at around 2 cm to 10 cm (Willi et al., 2018). The influential factor for PCO and PCV is the antenna type. Low-cost antennas may not be designed to minimize these effects, making them more susceptible to positioning errors (Krzan et al., 2024). Thus, proper calibration of the receiver's antenna phase centre is essential to mitigate these errors. Calibration involves measuring the phase centre offset for various elevation angles and applying corrections to the positioning data.

2.3.2.4 Phase wind-up effect

Phase wind-up is a phenomenon that affects carrier-phase measurements in GNSS due to the circular polarization of the signals transmitted from satellites. This effect becomes evident when the receiver antenna rotates, causing variations in carrier-phase measurements. As a satellite moves in orbit and the receiver changes its orientation often due to adjustments to keep the antenna pointed toward the Earth, the observed carrier-phase can shift even if there is no change in the actual distance between the satellite and the receiver. Specifically, a full 360^0 antenna rotation can change the phase measurement by one complete wavelength, which is approximately 20 cm for the GPS L1 frequency (Kim et al., 2005). In practice, the satellite's orientation is adjusted to keep its solar panels facing the sun, while the receiver antenna is designed to remain directed toward the Earth's surface. The phase wind-up effect must be corrected in the carrier-phase measurements to ensure accurate positioning. The wind-up correction can be computed using carrier-phase measurements (Tetewsky & Mullen, 1993).

2.3.2.5 Ionospheric and tropospheric delay

The ionosphere and troposphere are two atmospheric layers that significantly impact GNSS signal propagation. The ionosphere is between 50 and 1,000 km above the earth's surface. This layer acts as a dispersive medium and can significantly affect GNSS signals, particularly at higher frequencies. As GNSS signals travel through the ionosphere, variations in the density of free electrons cause changes in signal speed. This effect introduces a delay in pseudorange measurements. In contrast, due to its refractive properties, the ionosphere causes a phase advance in the carrier-phase measurement. GNSS systems often employ dual-frequency measurements to minimize ionospheric delays. The ionospheric delay can be estimated and corrected by comparing the delays experienced by signals at two different frequencies. For the uncombined mode of processing, ionospheric effects are considered as one of the state terms and are estimated.

The troposphere is an atmospheric layer up to 50 km from the earth's surface and causes delays in both pseudorange and carrier-phase signals of the same magnitude. Tropospheric delay consists of two components: a hydrostatic component (90%), which can be modelled, and a wet component (10%), which needs to be estimated (Hopfield, 1969). In the uncombined mode of PPP processing, a dry component is modelled using the global mapping function (GMF), tropospheric zenith hydrostatic delay (ZHD) is corrected, and a wet component is estimated to be a random walk process. The wet component, though smaller, requires dynamic estimation as it fluctuates based on local humidity and atmospheric conditions.

2.3.2.6 Sagnac effect

The Sagnac effect arises from the Earth's rotation and has essential implications for GNSS. The ECI (Earth-Centered Inertial) and ECEF (Earth-Centered Earth-Fixed) coordinate systems are essential frameworks for representing the positions and velocities of objects in space and on Earth. The ECI system is inertial, remaining fixed relative to the stars and not rotating with the Earth, while the ECEF system rotates with the Earth's surface, originating at the Earth's center and using the mean equatorial plane as its reference. Both systems originate at Earth's center of mass but differ in their angular orientation, quantified by the Earth Rotation Angle (ERA) or Greenwich sidereal angle (Teunissen & Montenbruck, 2017, p. 150). Satellite orbits are defined within an ECI reference frame, accounting for changes in Earth's rotation axis due to precession, nutation, and rotation. User locations are determined in the ECEF reference frame, whose coordinates change over time due to the Earth's rotation. This discrepancy between the two reference frames introduces a challenge in synchronizing time between satellites and receivers. The Earth rotates when a signal travels from a satellite to a receiver. This rotation creates a situation where the timing of the signal is affected, leading to discrepancies in clock synchronization. This phenomenon, known as the Sagnac effect, results in time delays that reach several hundred nanoseconds. The significance of this effect is underscored by the fact that a time error of just one nanosecond corresponds to an error of approximately 30 cm in distance calculations. GNSS systems implement correction algorithms that adjust the timing of the received signals based on the calculated rotation of the earth during the signal's travel time to account for the Sagnac effect. The detailed use of the formula can be found in (Hofmann-Wellenhof et al., 2007, p. 147).

2.3.2.7 Solid Earth tides

The effects of gravitational forces from celestial bodies like the moon and the sun must be accounted for in PPP. These tidal forces lead to slight displacements in the earth's crust that can reach up to 0.4 m in magnitude, affecting GNSS measurements (Teunissen & Montenbruck, 2017, p. 727). The tidal displacements can be substantial, reaching approximately 30 cm vertically and about 5 cm horizontally. The models that describe these tidal effects can be found in the works of (Kouba, 2009a; McCarthy et al., 2004).

2.3.2.8 Ocean loading

Ocean loading is caused by ocean tides, which can cause the displacement of the Earth’s crust. As ocean tides rise and fall, they can cause measurable displacements in the Earth’s crust, typically at the mm level. This effect is particularly significant in coastal areas, where the crust is more responsive to changes in water load.

2.3.2.9 Equipment delays

Equipment delays differ in frequencies and modulations within the same frequency. These delays are estimated in the form of time group delay (TGD) corrections, differential code bias (DCB) corrections or observable-specific signal biases (OSB) corrections. TGD refers to the delay introduced by the receiver's hardware when processing satellite signals. This delay is generally frequency-dependent, meaning it can vary between different frequency bands (e.g., L1, L2, L5) used in GNSS systems. DCB corrections account for the discrepancies between the signal travel times for different frequencies received by the same antenna. These biases can arise due to differences in signal processing and transmission paths. OSB corrections are related to specific signal characteristics and can vary with different modulation techniques. These biases are significant when dealing with various GNSS signals that may have unique properties affecting their reception. Hardware delay at the receiver can be eliminated through between-satellite single differencing. This technique involves comparing measurements from two satellites to eliminate common errors, including hardware delays. By differencing the signals, the receiver can effectively cancel out the systematic biases introduced by its hardware.

2.3.3 Precise Point Positioning ambiguity resolution (PPP-AR)

A primary limitation of traditional PPP is the long convergence time, ranging from tens of minutes to an hour, depending on satellite visibility, atmospheric conditions, and user dynamics. This convergence time arises because, initially, the model relies on less precise pseudorange measurements to estimate the various states, including the position states. After using carrier-phase measurements over time, the quality of the ambiguity estimate improves and subsequently reduces the convergence time (Collins et al., 2008; Laurichesse et al., 2009; Teunissen et al., 2010). This integer ambiguity resolution enhances the robustness of GNSS positioning, making it well-suited for real-time applications. Ambiguity resolution in PPP significantly reduces the convergence time by resolving the carrier-phase ambiguities rather than floating-point estimates.

PPP-AR can be done with three models in current practices: the Fractional Cycle Baises (FCB) method (Ge et al., 2008; Geng et al., 2011), the Decoupled Clock Model (DCM) (Collins et al., 2008), and the Integer Recovery Clock (IRC) (Laurichesse et al., 2009). A float solution is obtained through a least-squares adjustment. Once the float ambiguities are estimated by adopting these models, fixing integer values can be done using the ambiguity-fixing algorithm. Finally, the float solution for position, satellite, and receiver clock parameters and any additional correlated parameters is adjusted to yield a fixed solution. The most widely used method used for ambiguity resolution is Least squares AMBiguity Decorrelation Adjustment (LAMBDA)

(Teunissen, 1993). Figure 2.3 illustrates the typical workflow of ambiguity resolution (AR). As shown in the figure, LAMBDA takes float ambiguities and their covariance as input, decorrelates them, and identifies possible candidates using least squares adjustments. Once the candidate is validated, the float estimates state terms, including receiver coordinates, are updated.

This research is based on applying the Decoupled Clock Model (DCM) for PPP-AR. The DCM approach does not rely on predefined assumptions about receiver biases. Instead, it eliminates receiver biases within ambiguities by applying an implicit differencing through selecting a reference satellite. This technique results in estimated ambiguities being relative to the reference satellite, allowing for the estimation of receiver biases rather than removing them entirely.

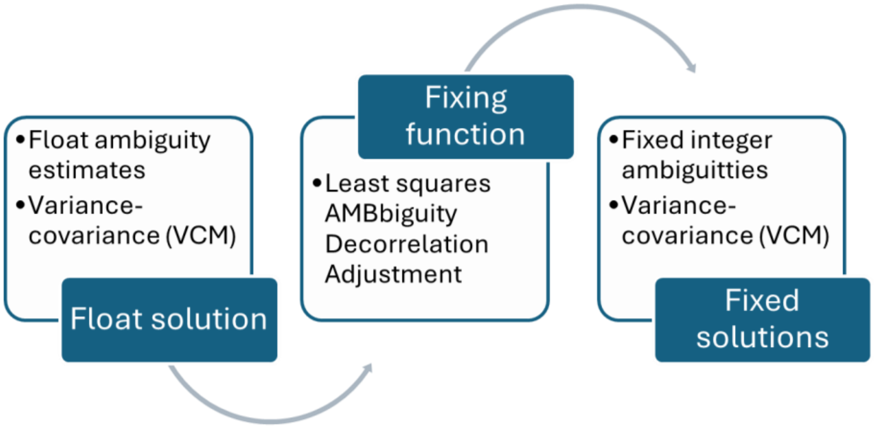

Figure 2.3: Fundamental process of fixing ambiguities in GNSS with LAMBDA

2.4 Advancements in high-precision, low-cost GNSS positioning

The advent of low-cost GNSS hardware has opened new possibilities for high-precision positioning applications traditionally dominated by expensive geodetic-grade receivers. Low-cost GNSS hardware occupies a middle ground between geodetic receivers and mass-market sensors found in devices like smartphones. Initially, only the single-frequency low-cost receivers were available, with no phase observations and limited to basic navigation. However, developing dual-frequency multi-constellation low-cost receivers for handling ionospheric error was possible and integrated into different RTK engines (Hamza et al., 2024). Today's low-cost receivers are multi-frequency and multi-constellation, offering improved precision (Septentrio, 2024.; u-blox, 2022).

The commercial growth of low-cost hardware has led to integration with different RTK and PPP-RTK solutions. PPP-RTK, a hybrid approach, combines the advantages of both PPP and RTK by using the SSR correction rather than OSR. These corrections include the clock and orbit adjustment, making PPP-RTK compactible with PPP, satellite phase bias correction for PPP-AR, and atmospheric correction for rapid, cm-level performance. Services such as point perfect, skylark cx, and Mosaic-CLAS provide PPP-RTK services with cm-level precision (u-blox, 2022; *Skylark Cx | Swiftnav*, 2024; *Mosaic-CLAS GNSS*, 2024). This advancement makes reliable, high-accuracy GNSS accessible to a broader range of industries.

PPP using low-cost devices are increasingly utilized in fields requiring dm- to cm-level accuracies, such as precision agriculture mapping (Nguyen et al., 2021), unmanned aerial vehicles (UAVs) (Falco et al., 2014) and environmental monitoring (Cui et al., 2017). Low-cost hardware is also used to detect deformation and seismic activity (Hou et al., 2018). Other studies

(Hamza et al., 2021; Hohensinn et al., 2022; Tunini et al., 2022; Wielgocka et al., 2021) show that these low-cost receivers can be used in various applications, from geodesy to surveying.

PPP-AR enhances positioning accuracy by resolving the integer ambiguities in carrier-phase measurements. Different research has been done recently regarding using PPP-AR on low-cost hardware. Chen et al. (2024) utilized a low-cost receiver paired with a geodetic antenna, while Ogutcu et al. (2023) focused on deformation monitoring using a low-cost receiver with a survey GNSS multiband antenna, employing dual-frequency measurements on GPS (fixed) and GLONASS (float) only. They demonstrated that post-processed GPS PPP-AR with a low-cost receiver and a low-cost uncalibrated antenna can detect horizontal displacements as small as 2 cm using 3-hour static observations. These findings support the potential of PPP-AR with low-cost devices as a valuable research avenue.

Stochastic modelling plays an essential role in representing GNSS measurement uncertainties, especially for low-cost hardware, which is more susceptible to noise and multipath errors. Weighting schemes based on the carrier-to-noise density ratio have been proposed to address the varying quality of observations from low-cost to geodetic-grade receivers (Hartinger & Brunner, 1999; Luo et al., 2009; Yuan et al., 2022; Y. Li et al., 2023; Brunner et al., 1999) by assigning higher weights to observations with better signal quality. Yuan et al. (2022) conclude that incorporating C/N_0 dependent functions could improve accuracy, as multipath effects, atmospheric delays, and baseline-specific characteristics significantly influence precise positioning in low-cost GNSS devices. Li et al. (2023) proposed an elevation-C/N_0 stochastic model, which improves GNSS measurement accuracy by addressing multipath and NLOS errors, enhancing ambiguity resolution and positioning reliability. Banville et al. (2019) further suggest that applying C/N_0--based weighting and regional ionospheric corrections can improve precision, supporting cm-level accuracy in low-cost measurements. These studies emphasize the C/N_0-based stochastic modelling as the observation weighting is promising to obtain high precision using a low-cost receiver.

Despite notable advancements, cm-level positioning has not yet been fully achieved with low-cost GNSS hardware. However, recent developments in low-cost devices, such as multi-frequency and multi-constellation support, indicate strong potential for reaching this level of precision. With continued advancements in hardware and the appropriate stochastic models, cm-level accuracy may soon become feasible.

Chapter 3 Analysis of GNSS measurement characteristics for geodetic and low-cost hardware

This chapter delves into the analysis of measurement characteristics of geodetic and low-cost GNSS hardware. The chapter is structured into two main sections. The first provides a detailed overview of the GNSS hardware used in this research. The second section offers a comprehensive comparative quality assessment, examining the performance of measurements from geodetic and low-cost hardware across critical metrics, including signal carrier-to-noise density ratio, pseudorange noise and multipath, cycle slips, and data availability.

3.1 GNSS positioning hardware

The GNSS receiver and antenna are the two main hardware components. The available types of antennas and receivers cater to diverse applications, ranging from consumer navigation to high-precision industrial use. Based on the application, the antenna and receiver can be separated (geodetic hardware) or combined into a single device (smartphones). Further, GNSS hardware can be integrated with other application-specific sensors. The specifications and features of GNSS equipment vary according to its intended use. The following subsection discusses the details of the GNSS receiver and antenna used in this research.

3.1.1 GNSS receivers

GNSS hardware encompasses various components and system designs that receive, process, and utilize signals from GNSS satellites for PNT purposes. Modern GNSS receivers sequentially process these signals through several key stages, starting with the antenna, which captures the satellite signals. Due to the nature of these signals upon arrival, preamplifiers, notably the low-noise amplifier (LNA), are employed to boost signal strength without introducing significant noise and maintain a good SNR (Teunissen & Montenbruck, 2017b, p. 372).

The amplified signals then pass through the radio frequency (RF) frontend, which performs initial signal conditioning. Pseudorange measurement quality relies on the bandwidth of the RF signal processing chain (Teunissen & Montenbruck, 2017a, p. 376). Critical components of the RF frontend include the LNA, RF filters, and intermediate frequency (IF) filters. The RF filters select the desired frequency band and reject out-of-band interference. These filters are typically designed as bandpass filters and can be either fixed or adaptive. Fixed filters are preconfigured for specific frequency bands, while adaptive RF filters adjust dynamically based on the frequency band of interest, which is often determined by the GNSS receiver's configuration. This flexibility enables the receiver to handle signals from multiple GNSS constellations or frequency bands.

The next stage involves the mixer, which combines the high-frequency GNSS signal from the antenna with a local oscillator (LO) signal. This process, known as frequency mixing, produces a new signal at the intermediate frequency (IF). The purpose of this operation is to shift the high-frequency GNSS signal to a lower frequency, which is easier to process. Specifically, the mixer outputs three components: the original high-frequency signal, the LO signal, and the desired IF signal (a combination of the two frequencies). The system selects the IF signal while suppressing the other components. This intermediate frequency is now suitable for further processing. After frequency conversion, a bandpass filter is applied to eliminate unwanted frequencies generated during mixing. An automatic gain control (AGC) circuit may be incorporated to dynamically adjust the gain of the frontend, ensuring that the signal levels remain within an optimal range despite variations in the incoming signal strength. AGC prevents the receiver from overloading due to strong signals and ensures sufficient amplification of weak ones.

Following these steps, the signal enters the signal tracking block, which is a critical stage for maintaining synchronization with the satellite signal. This block consists of correlators, tracking loops, and loop filters that work together to extract meaningful information. Correlators match the incoming satellite signal with locally generated pseudorandom noise (PRN) codes, aligning the receiver with the satellite's unique signal. Tracking loops, which include the delay lock loop (DLL), frequency lock loop (FLL), and phase lock loop (PLL), ensure continuous synchronization with the satellite signal despite changes caused by satellite or receiver movement. The DLL tracks the code phase of the signal, ensuring alignment between the incoming and local PRN codes. The FLL monitors and compensates for frequency shifts due to the Doppler effect, while the PLL provides high-precision tracking of the carrier phase, crucial for precise positioning. Loop filters play a vital role in refining the outputs from the tracking loops by removing noise and stabilizing the signal, which is especially important for GNSS receivers dealing with inherently weak and interference-prone signals. These filters ensure that the tracked signal is stable and suitable for further processing. Finally, the refined signals are processed by the receiver's digital circuitry, which computes the position, navigation, and timing (PNT) solutions.

3.1.2 GNSS antenna

The antenna is the initial contact point for GNSS signals. It is designed to receive either a single frequency e.g. L1 or multiple frequencies e.g. L1, L2, L5 from any or all different constellations. The GNSS antenna is designed to receive right-hand circular polarization signals. This research utilizes two types of GNSS antennas: a geodetic antenna and a low-cost patch antenna. Another important characteristic of an antenna is its gain pattern. The gain pattern is a graphical representation that shows the sensitivity of received signals over a range of elevation and azimuth angles. In other words, antenna gain measures the strength of the transmitted signal in the direction of peak radiation compared to an isotropic antenna (an ideal antenna that radiates equally in all directions). Gain pattern also influences the ability to mitigate multipath signals. For instance, an antenna gain pattern of ±3 dBic toward the satellite reflects its sensitivity in those directions, providing optimal reception for overhead satellites and adequate coverage for low-elevation satellites(Teunissen & Montenbruck, 2017, p. 372).

A GNSS antenna should be omnidirectional, meaning it can receive signals from all directions around it. However, while it captures signals horizontally across a wide range, its directional sensitivity is primarily focused on the elevation plane, allowing it to receive better signals from satellites at various elevation angles in the sky. Some antennas, such as patch antennas, require the ground plane to reduce the impact by attenuating reflected signals. In contrast, the most precise geodetic antennas have a chokering design, which eliminates the need for a ground plate. A chokering consists of concentric metal rings surrounding the central antenna element, creating a controlled impedance environment that suppresses signals from low elevation angles, greatly reducing potential multipath.

3.1.3 Overview of GNSS positioning hardware used in the research

Figure 3.1 shows the geodetic and low-cost GNSS hardware used in this research. The NovAtel GNSS-850 [1](top left) is used as a geodetic antenna, while the NovAtel OEM7[2] (bottom left) is

---

[1] https://hexagondownloads.blob.core.windows.net/public/Novatel/assets/Documents/Papers/GNSS-850-Product-Sheet/GNSS-850-Product-Sheet.pdf

[2] https://hexagondownloads.blob.core.windows.net/public/Novatel/assets/Documents/Papers/PwrPak7-E1-Product-Sheet/PwrPak7-E1-Product-Sheet.pdf

used as the geodetic receiver. The Tallysman TW7972 [3](top right) is used as the low-cost patch antenna and is paired with the Septentrio Mosaic-X5 [4]receiver (bottom right). The Mosaic-X5 is a multi-frequency, low-cost receiver module.

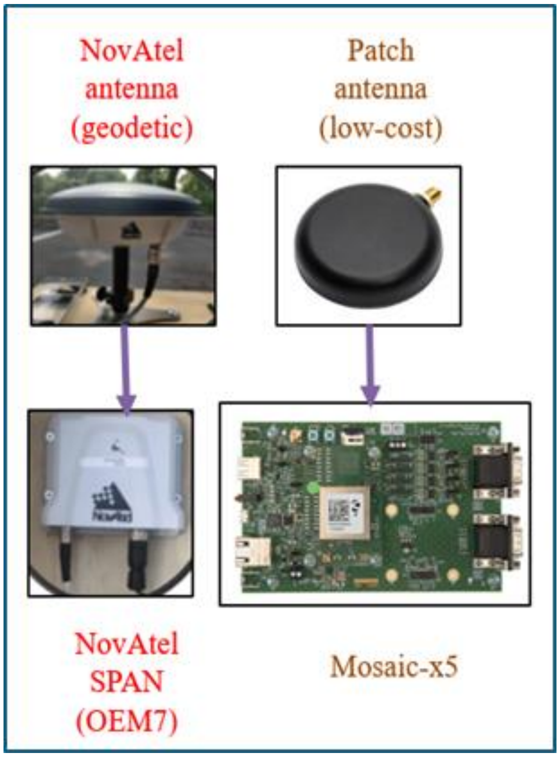

Figure 3.1: GNSS receiver and antenna used for the research and analysis

The choice of antenna and receiver can significantly affect the accuracy of GNSS position solutions (Miletiev et al., 2024). The specifications from the manufacturer are used to compare the features of geodetic and low-cost hardware. Table 3.1 compares the features of the geodetic and low-cost antennas used in this research. The geodetic antenna is built with a multi-point feed design that stabilizes the phase centre and improves its ability to reject multipath interference (Hexagon | NovAtel, 2023). However, the low-cost antenna is more compact and

---

[3] https://sites.calian.com/app/uploads/sites/8/2024/06/Calian%C2%AE-TW7972 Datasheet.pdf?_gl=1*mwhm9v*_gcl_au*MTIzMDU5NzA4MC4xNzMxMTcyMzA2

[4] https://www.septentrio.com/en/products/gnss-receivers/gnss-receiver-modules/mosaic-x5

lightweight, which makes it ideal for use in portable and embedded applications where size and weight are crucial factors, such as autonomous drones, robotics, and IoT applications.

Table 3.2 compares a gain pattern of the same geodetic and a low-cost antenna across various frequencies. The geodetic antenna consistently offers higher gain at the zenith, particularly in the L1/E1, L2/E2, L5/E5a, and G1 bands (Hexagon | NovAtel, 2023). The G1 frequency band is the L band (1589.0625 MHz to 1605.375 MHz) used by GLONASS. Noticeable differences are seen in the gain pattern, especially on the L5/E5a frequency, where the low-cost antenna shows a significant drop in the gain pattern (Calian, 2023). Additionally, the geodetic antenna has a lower LNA noise figure than the low-cost antenna. The noise figure is defined as the ratio of the SNR at an amplifier's input to the SNR at its output. A low noise figure is critical for GNSS receivers as it allows them to effectively process the GNSS signal, resulting in accurate and precise positioning and timing. A noise figure of less than 2 dB is typically optimal for GNSS applications (Calian, 2024). In this case, the geodetic receiver meets this requirement, while the low-cost receiver has a higher noise figure of 2.5 dB, which impacts signal processing quality. However, the low-cost antenna has a better voltage standing wave ratio (VSWR) than the geodetic antenna. VSWR represents the ratio of transmitted power to reflected power, with a lower VSWR indicating better impedance matching between the antenna and cable, resulting in minimal power reflection (Kumar et al., 2010).

Table 3.1 Comparative features of a geodetic antenna and low-cost antennas used in the research

Features	Geodetic antenna (GNSS-850)	Low-cost antenna (TW7972)
Frequency ranges	GPS L1/L2/L5, GLONASS G1, G2, G3, Galileo E1, E5a/b, E6, BeiDou B1, B2, B3 QZSS L1, L2, L5, L6	GPS L1/L2/L5, GLONASS G1, G2, G3, Galileo E1, E5a/b, E6, BeiDou B1, B2b/2a QZSS L6
Multipath rejection	Enhanced multipath rejection	Basic multipath reduction features
Antenna design	Advanced multi-point feed network and radiation pattern optimization design	Compact, lightweight design
Dimensions	176mm (diameter) * 55mm (height)	~25 mm x 25 mm x 4 mm
Weight	507 g	180 g
Cost	~ 10,000 USD[5]	~ 300 USD[6]

Table 3.2: Antenna gain pattern comparison between geodetic antenna and low-cost antennas used in the research

Gain at zenith	Geodetic antenna (GNSS-850)	Low-cost antenna (TW7972)
L1/E1/B1	5.0 dBic min	4.0 dBic min
L2	5.0 dBic min	4.0 dBic min
E5a/L5/B2a	3.0 dBic min	1.5 dBic min
E5b/G3/G2	5.0 dBic min	2.5 dBic min
G1/G2/G3/E5b/B2b	5.0 dBic min	2.5 dBic min
Overall LNA	29 dB typ	32 dB typ
LNA noise figure	2.0 dB typ	2.5dB typ
VSWR	<2.0:1 typ	<1.5:1 typ

---

[5] NovAtel Inc. (n.d.). NovAtel Inc. price list. https://gps-ttff.tripod.com/pricelist.pdf

[6] https://canada.newark.com/tallysman-wireless/33-7972-07/gnss-patch-antenna-1-557-1-606ghz/dp/39AH1228

3.2 Measurement quality metrics

The experiment was conducted on the roof of the Lassonde Research Centre (LRC) building at the Keele Campus of York University, Toronto, Canada. A low-cost patch antenna was connected to the low-cost receiver (Septentrio, Mosaic-X5), as shown in Figure 3.1. Further, a geodetic-grade antenna is connected to a NovAtel geodetic-grade receiver. The measurements from the geodetic-grade receiver are processed to derive reference coordinates. These reference coordinates are used to evaluate the performance of the low-cost hardware. For the reliability of this research, data were collected for approximately 72 hours in a medium multipath open sky environment. Table 3.3 illustrates the data used for the analyses done in Chapter 3. The data were collected from December 2023 to April 2024, and each recording lasted 10 to 17 hours. This extensive dataset provides a reliable basis for assessing the performance difference between geodetic and low-cost GNSS hardware. Metrics chosen for assessing the performance difference are signal carrier-to-noise density ratio, pseudorange noise and multipath, cycle slips, and data availability, as these metrics are essential for evaluating the quality of raw measurements. Further, these metrics offer valuable insights into the performance of the hardware and can also be used for effective quality control.

Table 3.3: Summary of data collection periods for signal quality analysis across various dates and durations

S.N.	Date	GPS Day of Year (DOY)	Duration
1	13th December 2023	347	12 hours
2	21st December 2023	355	10 hours
3	30th December 2023	364	10 hours
4	13th April 2024	104	17 hours
5	16th April 2024	107	10 hours
6	17th April 2024	108	13 hours

3.2.1 Carrier-to-noise power density ratio

C/N_0 is a vital signal quality indicator in GNSS. The signal power and noise power are estimated during the correlation phase, where the incoming GNSS signals in the receiver are aligned with a locally generated replica signal. Simultaneously, the noise primarily originating from the receiver's electronics component is also quantified. This noise is typically referred to as thermal noise. According to Langley (1997), thermal noise is not the physical temperature of the hardware but the movement of electrons within receiver's conductor and the electromagnetic radiation present in antenna's surrounding atmosphere.

Thermal noise is considered uncorrelated noise with a Gaussian distribution (Langley, 1997). In this context, "white" refers to the noise being uncorrelated, meaning that the noise at any given moment is independent of the noise at any other moment. This uncorrelated nature ensures that the noise has a flat spectral density, which affects all frequencies equally within the bandwidth of interest. A Gaussian distribution suggests that most noise values are small, with fewer large deviations, typical of the random process occurring at the microscopic level in electronic components. Signal-to-Noise (SNR) ratio is the ratio of signal power (S) to the noise power (N) over the receiver's bandwidth (B):

$$SNR = 10\log_{10}(\frac{S}{N}) \qquad \text{dB} \qquad (3\text{-}1)$$

For GPS, SNR values are expressed in dB. The ratio of carrier (C) power to the noise power (N_0) in 1 Hz bandwidth is carrier-to-noise density ratio (C/N_0)(Hofmann-Wellenhof et al., 2007, p. 86) :

$$\mathrm{C/N_0} = 10\log_{10}\left(\frac{C}{N_0}\right) \qquad [\text{dB Hz}] \qquad (3\text{-}2)$$

Noise power (N) is proportional to the receiver bandwidth (B) in Hz.

$$N = N_0 \,. B \tag{3-3}$$

Since the noise power increases with larger bandwidths, normalizing it to unit bandwidth provides a bandwidth-independent metric. If we use the full noise power (N) in a specific bandwidth (B), the carrier-to-noise ratio would be complex to compare the quality across receivers with different bandwidths, and hence the noise power density (N_0) is used instead of the total noise power (N). Therefore, C/N_0 is a density ratio that represents the carrier power relative to the noise power per unit bandwidth.

The carrier power reflects the total energy of the GNSS signal received, which is typically very weak (-160 dBW). The noise power density represents the noise per 1 Hz of bandwidth. By comparing the signal power to the noise power density, C/N_0 represents the carrier power normalized to the noise power per 1 Hz bandwidth, ensuring the metric is independent of receiver bandwidth and providing a consistent measure of signal quality. To be considered a strong signal, C/N_0 should be larger than 34 dB Hz, and nominal C/N_0 is 44 dB Hz (Hofmann-Wellenhof et al., 2001). While larger C/N_0 values typically indicate better signal power and quality, true signal quality depends on additional factors, including hardware-induced distortions and environmental interference.

3.2.1.1 Carrier-to-noise density ratio and elevation with different frequencies

The scatter plot in Figure 3.2, Figure 3.3, and Figure 3.4 compares the C/N_0 values as a function of the satellites' elevation angle for geodetic (red) and low-cost (blue) receivers across the first, second, and third frequencies, respectively. Figure 3.6 is a box plot comparing the C/N_0 for geodetic (red) and low-cost (blue) antennas across different frequencies. The y-axis shows the C/N_0 values for various frequencies in dB Hz. The box plots (Figure 3.5) illustrate the interquartile range (IQR), encompassing the middle 50% of the data. The bottom and top edges of the box mark the 25th percentile (Q1) and the 75th percentile (Q3), respectively. A yellow horizontal line within the box indicates the median (or 50th percentile) of the data. The whiskers extend to show the range within 1.5 times the IQR from the quartiles, while any points beyond this span are treated as outliers.

Across all three frequencies, the C/N_0 is well distributed, with higher values at higher elevation angles as the satellites move closer to the zenith. Geodetic hardware consistently shows a higher and more stable C/N_0 across all frequencies, as shown in Figures 3.3,3.4, and 3.5. In low-cost hardware, the C/N_0 representing Q1 at the second frequency extends as low as 20 dB Hz. In contrast, the Q1 for the first and third frequencies extend to approximately 30 dB Hz and 25 dB Hz, respectively. The whiskers at the second frequency of low-cost hardware is extended nearly to 0 dB Hz, indicating significant variability, as shown in Figure 3.5. This variability suggests a broader range of signal fluctuations in the second frequency than the other two frequencies. This degree of variability and signal degradation at the second frequency is unexpected, especially given the similar gain patterns (4 dBic) for L1/E1 and L2 frequencies (Table 3.2). Signals at all three frequencies are expected to demonstrate comparable performance.

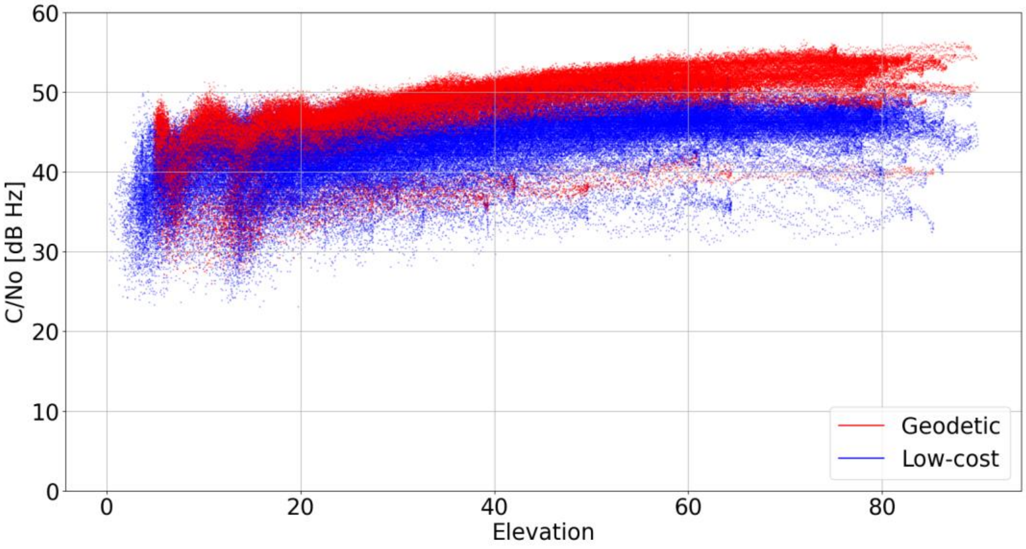

Figure 3.2: C/N$_0$ against elevation angles on first frequency signal

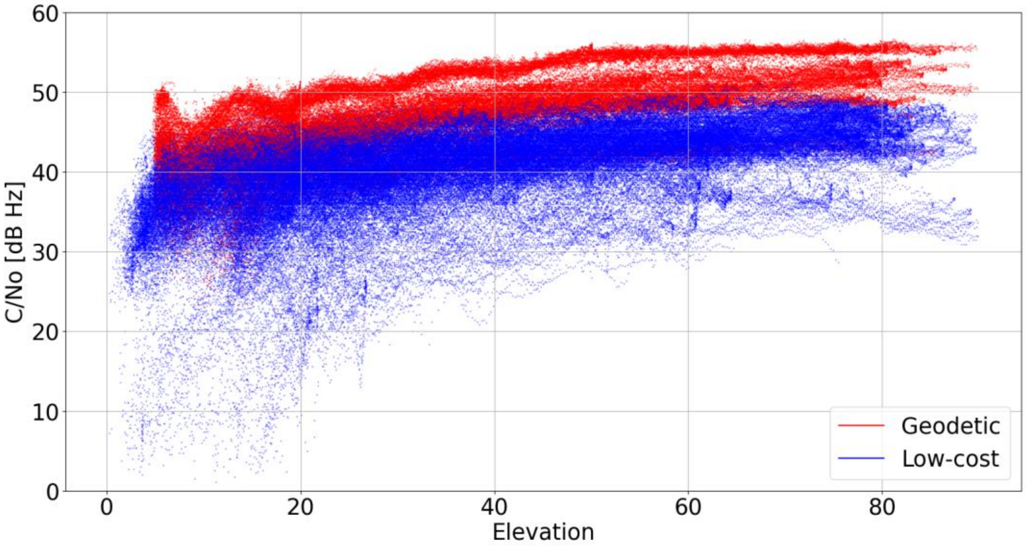

Figure 3.3: C/N$_0$ against elevation angles on second frequency signal

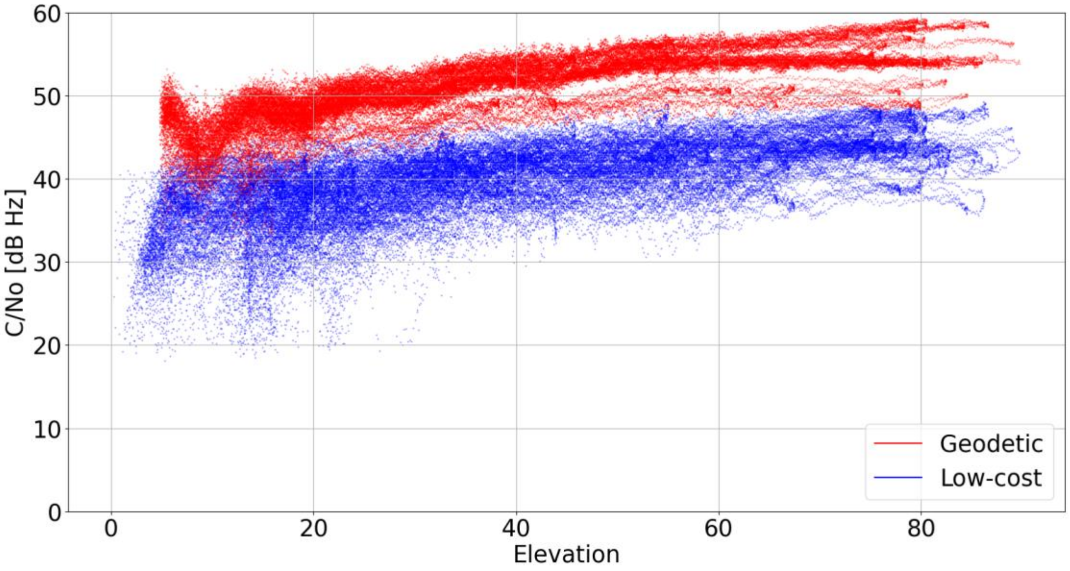

Figure 3.4: C/N₀ against elevation angles on third frequency signal

The comparison of C/N₀ ratios between two hardware across three frequencies reveals a consistent performance gap between geodetic and low-cost hardware. The low-cost receiver shows a mean C/N₀ of approximately 4 dB Hz, 7 dB Hz, and 10 dB Hz lower than the geodetic hardware at the first, second, and third frequencies. At the first frequency, the geodetic receiver achieves stable signal reception with a mean of 47.6 dB Hz compared to 43.2 dB Hz for the low-cost receiver. This gap widens at the second frequency, where the geodetic receiver maintains a mean C/N₀ of 47.5 dB Hz, while the low-cost receiver drops to 40.2 dB Hz, showing significant variability with an interquartile range (IQR) of 6.3 dB Hz (Figure 3.6). The disparity is most pronounced at the third frequency, with the geodetic receiver's mean C/N₀ at 50.9 dB Hz compared to 40.4 dB Hz for the low-cost receiver.

This analysis reveals that, for geodetic receivers, the C/N₀ consistently increases at the third frequency compared to the first and second frequencies. In contrast, low-cost receivers show the highest C/N_0 at the first frequency, with the second and third frequencies performing similarly. Although the L5 signal (third frequency) operates at 1176.45 MHz with a higher chipping rate of 10.23 MHz, resulting in a narrower correlation peak. The L1 and L2 signals have a chipping rate of 1.023 MHz (Teunissen & Montenbruck, 2017a, p. 209). The chipping rate dictates how quickly individual "chips" (bits of the pseudorandom noise, or PRN, code) are transmitted per second. A higher chipping rate like that of the L5 signal yields a narrower correlation peak, allowing the receiver to match the incoming satellite signal with its PRN code more precisely and thus measure the signal's arrival time with greater accuracy (Erker et al., 2009; Leclère et al., 2018). Ideally, L5 signal would enhance signal quality at the third frequency, just like a result observed in geodetic receivers. However, low-cost receivers show lower performance in third frequency. The degradation in performance is linked to the antenna gain pattern of the low-cost receiver, which is 1.5 dBic at the zenith for L5/E5a, compared to 3.0 dBic (Table 3.2) for the geodetic antenna, explaining the degradation in signal strength.

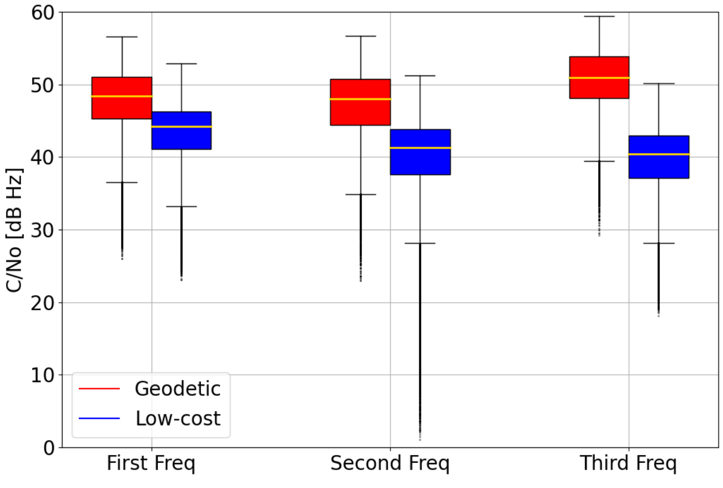

Figure 3.5: Boxplot comparison of C/N_0 across three frequencies for geodetic and low-cost measurements

3.2.2 Measurement noise

Measurement noise is a fundamental concern in GNSS data processing, as it directly affects the accuracy and reliability of positioning solutions. One effective technique for analyzing and quantifying measurement noise is the code-minus-carrier (CMC) linear combination method. The CMC method involves differencing the pseudorange and carrier-phase measurements to isolate and evaluate the non-systematic errors in GNSS observations.

The raw measurements for pseudorange and carrier-phase on the single frequency for the static observations can be expressed as:

$$P = \rho + c\,(dT - dt) + I + T + \varepsilon_P \tag{3-4}$$

$$\phi = \rho + c(dT - dt) - I + T + N.\lambda + M_\phi + \varepsilon_\phi \tag{3-5}$$

where ρ is the geometric range between satellite and receiver, *c* is the speed of light, dT and dt are receive clock and satellite clock error, respectively, *I* is the ionospheric delay, *T* is the tropospheric delay, *N* is the integer ambiguity, λ is the carrier wavelength and ε_P and ε_ϕ are measurement noise and multipath in pseudorange and carrier-phase measurement respectively. The CMC method computes the difference between the pseudorange (p) and carrier-phase (ϕ) measurements for a given satellite signal:

$$\text{CMC} = P - \phi = 2I + N\lambda + \left(M_p + M_\phi\right) + (\varepsilon_p - \varepsilon_\phi) \tag{3-6}$$

The range, satellite and receiver clock offsets, and tropospheric delay are cancelled out as these are common to both pseudorange and the carrier-phase measurement (Teunissen & Montenbruck, 2017a, p. 460). The ionospheric delay appears twice because it oppositely affects pseudorange and carrier measurements by delaying the pseudorange and advancing the carrier (Héroux & Kouba, 2001). While pseudorange measurements are subject to higher noise levels and multipath errors, carrier-phase measurements are more precise. Therefore, carrier-phase noise will have a negligible effect on the system. However, it includes integer ambiguities. The time difference between the consecutive epochs is done so that any terms that are constant over time are cancelled out (Caamano et al., 2020).

$$\Delta CMC_k = \frac{1}{\Delta t}(CMC_k - CMC_{k-1})$$

The remaining terms on the CMC are as follows:

$$\Delta(P - \phi) = 2\Delta I + \Delta M_p + \Delta \varepsilon_p \tag{3-7}$$

The carrier-phase ambiguity term is effectively removed through time differencing because it remains constant over short intervals. What remains are the twice the rates of change of the ionospheric delay, multipath, and noise. These components vary over time, with multipath and noise typically fluctuating more rapidly, making them detectable using this approach. Even though the absolute ionospheric delay is significant, its rate of change over short time intervals is often negligible compared to the rapid fluctuations caused by multipath and noise. In nominal conditions (normal atmospheric conditions), the ionospheric rate-of-change contributes minimally to the TD-CMC residuals, allowing multipath and noise to dominate the equation (Caamano et al., 2020).

Measurement noise can now be quantified by analyzing the residuals from the CMC calculations (3-6). The root mean square (rms) values of the CMC residuals were analyzed for geodetic and low-cost receivers using the datasets (Table 3.3), with the results summarized in Table 3.4. A sample dataset was selected to illustrate these results visually. Figure 3.6 provides a graphical representation of measurement noise analysis using CMC residuals, comparing geodetic-grade hardware (left) and low-cost hardware (right) across three frequency bands: C1-

L1 (top row), C2-L2 (middle row), and C5-L5 (bottom row). Each plot shows residual noise levels in metres over a 10-hour observation period (03:00 to 13:00 HH) from DOY 355 in 2023.

As illustrated in Table 3.4, the geodetic receiver demonstrates significantly lower rms noise levels: 0.6 m for C1-L1, 0.8 m for C2-L2, and 0.5 m for C5-L5. In contrast, the low-cost receiver exhibits much higher noise with rms values: 3.3 m for C1-L1, 2.1 m for C2-L2, and 1.8 m for C5-L5. This results in a substantial noise ratio between low-cost and geodetic hardware, with the low-cost receiver displaying approximately 5.5 times more noise for C1-L1, 2.6 times more for C2-L2, and 3.6 times more for C5-L5. These ratios reflect the higher noise susceptibility of low-cost receivers compared to geodetic hardware. High noise levels impact signal quality and negatively impact positioning accuracy.

Table 3.4: Measurement noise rms analysis for geodetic and low-cost hardware

Device	Measurement noise (rms)		
	C1-L1 (m)	C2-L2 (m)	C5 - L5 (m)
Geodetic	0.6	0.8	0.5
Low-cost	3.3	2.1	1.8
Ratio (Low-cost: Geodetic)	5.5	2.6	**3.6**

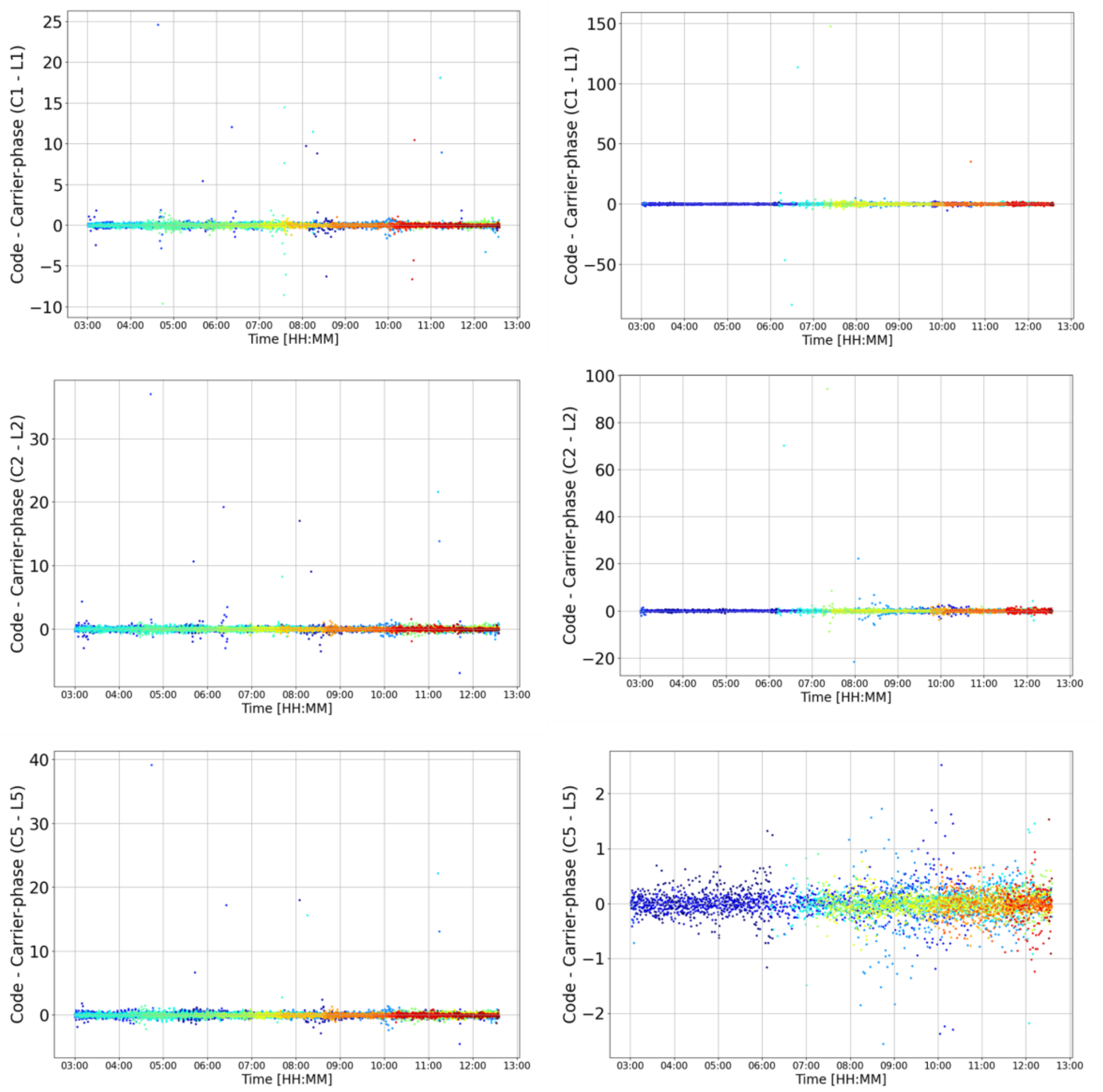

Figure 3.6 Measurement noise analysis using CMC residuals for geodetic hardware (left) and low-cost hardware (right) with C1-L1 (top), C2-L2 (middle), and C5-L5 (bottom) (in m) for DOY 355, 2023

3.2.3 Code multipath

Multipath refers to the phenomenon where GNSS signals travel from the satellites to the receiver via multiple paths, including direct and reflected signals. Multipath occurs because the signal gets reflected off nearby surfaces, such as buildings, water bodies, or the ground, causing the signal to take multiple paths to the receiver. The direct signal follows the shortest path, while reflected signals take longer paths due to bouncing off surfaces. This difference in path lengths causes relative phase offsets between the direct and reflected signals (Brodin & Daly, 1998; Hofmann-Wellenhof et al., 2007). Carrier-phase and pseudorange measurements are impacted differently by multipath. The error introduced by carrier-phase multipath is relatively small, capped at a quarter of the wavelength of the GNSS signals with respect to pseudorange, whereas for the pseudorange, multipath errors can be much larger, often reaching several metres in magnitude (Brown & Mathews, 2005; Amielh et al., 2017; Aggrey et al., 2019).

Unlike measurement noise, multipath cannot be characterized as a random error. The severity and nature of multipath errors depend on the changing geometry between the satellite, the reflecting surface, and the receiver. The multipath error also varies as these relative positions change over time, as with satellite movement or environmental shifts. This results in a pattern where multipath errors are periodic, typically fluctuating on timescales from several seconds to several minutes.

Additionally, unlike random errors that often average to zero over time, multipath errors generally do not have a mean value of zero. Multipaths cannot simply be averaged out and are thus more persistent in affecting GNSS accuracy. Due to their non-zero mean and periodic behaviour, multipath errors require specific mitigation techniques, such as advanced signal processing or antenna design, to minimize their impact on positioning accuracy. Research shows that low-cost antennas exhibit a two- to three-fold decrease in accuracy compared to geodetic antennas (Krzan et al., 2024). Understanding how multipath affects these receivers is critical for improving the accuracy of GNSS-based systems.

A universal model for multipath does not exist because the time and location-dependent scenario is unique and dynamic. However, multipath effects can be estimated by combining multi-frequency pseudorange and carrier-phase measurements. The multipath effects on each frequency are estimated using multipath estimation (Estey and Meertens, 1999; Strode & Groves, 2015).

$$\left.\begin{aligned} MP_1 &= P_1 - \left(1+\frac{2}{\alpha-1}\right)\Phi_1 + \left(\frac{2}{\alpha-1}\right)\phi_2 \\ MP_2 &= P_2 - \left(\frac{2\alpha}{\alpha-1}\right)\phi_1 + \left(\frac{2\alpha}{\alpha-1}-1\right)\phi_2 \\ MP_5 &= P_5 - \left(\frac{2}{\alpha-1}\right)\phi_1 + \left(\frac{2\alpha}{\alpha-1}-1\right)\phi_5 \end{aligned}\right\} \tag{3-8}$$

where, MP_1, MP_2 and MP_3 are the code multipath estimations for the first, second, and third frequencies, respectively. P_n and ϕ_n are pseudorange and carrier-phase measurements of frequency n. α is the ratio of the frequencies of the two GNSS signals being used. $\alpha = \left(\frac{f_1}{f_2}\right)^2$ and $\alpha = \left(\frac{f_1}{f_5}\right)^2$ for MP_1, MP_2 and $MP5$, respectively. The collected measurement described in Table 3.3 are used further to analyze code multipath on geodetic and low-cost hardware. Table 3.5 presents a detailed comparison of code multipath for three different GNSS frequencies.

Table 3.5 reveals the difference in multipath errors between the hardware. The geodetic observables consistently exhibit low multipath errors, with values increasing modestly from 0.3 m on the first frequency to 0.6 m on the third. In contrast, the low-cost device experiences significantly higher multipath errors, ranging from 1.5 m on the first frequency to 1.7 m on the third. Interestingly, the multipath effect on the first frequency is lower than the third for both receivers. The low-cost device, however, shows a significantly higher average multipath error of approximately 1.7 m across all frequencies about 3 to 5 times greater than the geodetic device. These findings suggest that low-cost hardware is considerably more susceptible to code multipath effects.

Table 3.5: Average code multipath rms (m) for geodetic and low-cost hardware in different frequencies

Device	Code multipath in m		
	First frequency	Second frequency	Third frequency
Geodetic	0.3	0.4	0.6
Low-cost	1.5	1.7	1.7

DOY 355, 2023, is used as a representative sample to illustrate multipath on geodetic and low-cost GNSS hardware. Figure 3.7 shows six subplots, with the left column representing the geodetic receiver and the right column representing the low-cost receiver across three frequencies (L1, L2, and L5). For the geodetic receiver, multipath is consistently low and stable across all frequencies, with minimal variation observed, especially in the L1 plot. Although the L5 frequency shows slightly more variability, errors remain within a low range. In contrast, the low-cost receiver displays significantly more dispersed and higher multipath errors across all frequencies. Low-cost observables exhibit wide scattering for all three frequencies, as demonstrated in the plots.

Furthermore, Figure 3.8 represents the multipath analyses on different GNSS constellations on the DOY 355, 2023. Across all GNSS constellations, geodetic hardware exhibits significantly lower rms multipath values than low-cost hardware. On average, multipath on geodetic hardware is less by approximately 70% compared to low-cost hardware in all constellations, which is about 3 times higher than in geodetic hardware across all the constellations. Positional performance can vary significantly in multipath environments due to poor geometry, signal blockage and multipath/NLOS (Chen et al., 2013). Understanding the specific environmental factors, including buildings, reflective surfaces, and nearby obstacles, is critical for effective multipath analysis and mitigation. The following study investigates the influence of site-specific features on GNSS signals.

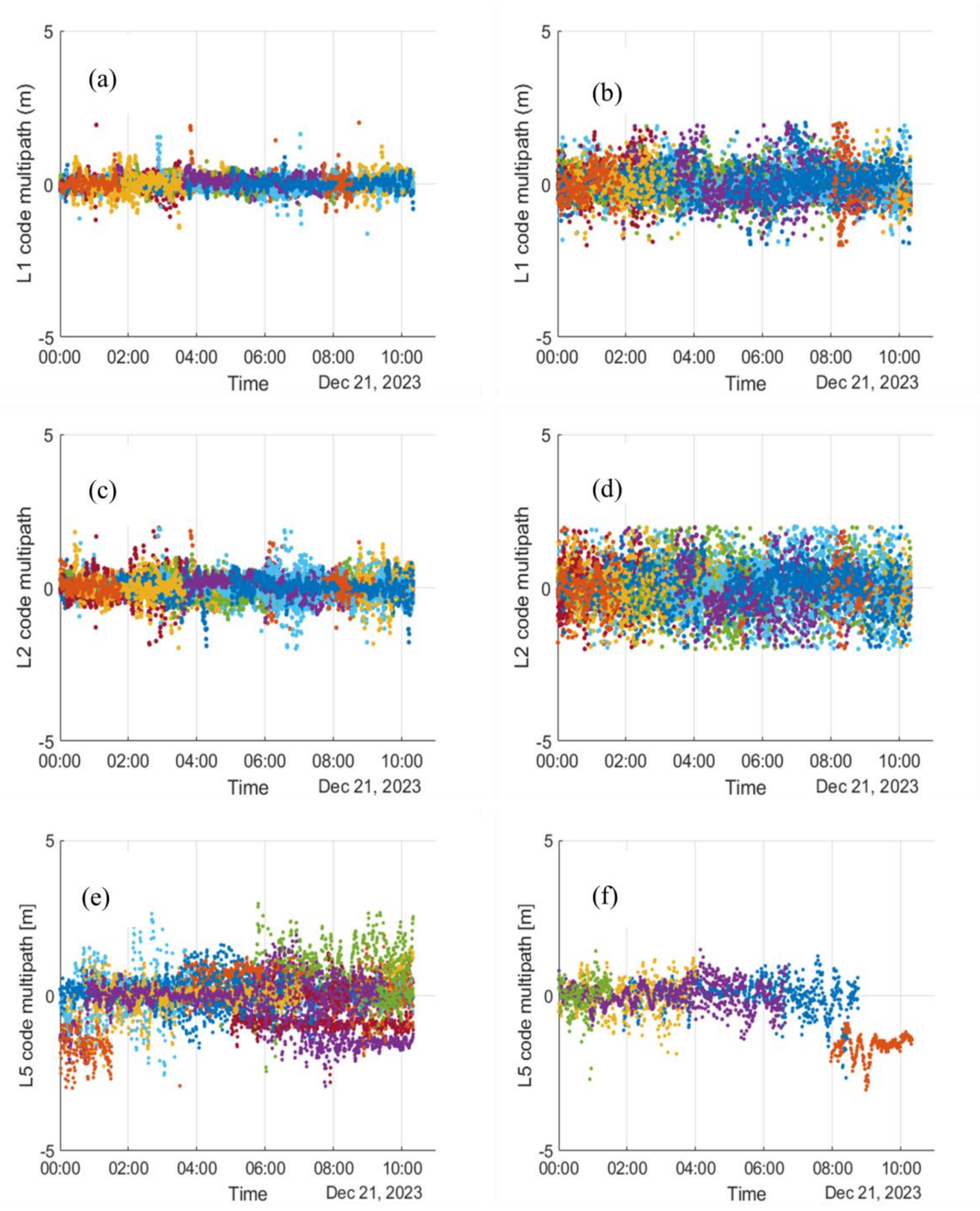

Figure 3.7 Multipath analysis for L1, L2, and L5 frequencies in a static, medium-multipath environment (DOY 355, 2023): geodetic antenna (a, c, e for L1, L2 and L3 frequency respectively) and low-cost antenna (b, d, f for L1, L2 and L3 frequency respectively). Each colours represents separate satellites from different constellations

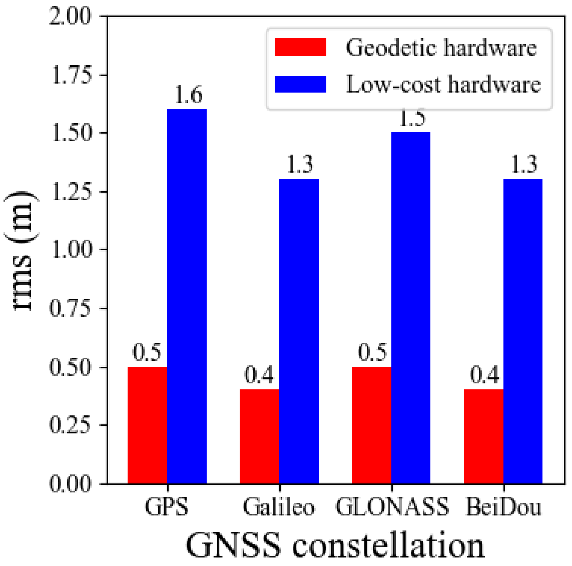

Figure 3.8 Multipath rms error for different GNSS constellations for geodetic hardware and low-cost hardware for DOY 355, 2023

Figure 3.9 illustrates two main components: a Google Earth image showing the data collection site and two polar plots (bottom). The left polar plot represents geodetic, and the right represents low-cost hardware measurements. The polar plot attached displays a multipath to the azimuth and elevation angles. The location of the GNSS antenna is marked on the map using a yellow pinpointer. The polar plots reveal significant differences in geodetic and low-cost hardware code multipath. For the geodetic receiver, most multipath errors remain below 0.6 m. In contrast, the low-cost hardware exhibits substantially higher code multipath, up to 1.8 m. Google Earth image reveals the presence of large reflective surfaces (buildings, trucks, parking lots) near the GNSS hardware. These surfaces likely contribute to the higher multipath errors in the low-cost receiver at low elevation angles. Some satellites, even at higher elevation angles of more than 40^0, seem to suffer from multipath in the low-cost receivers, which is less prominent in geodetic receivers. Both the hardware encounter code multipath at low elevation angles. The scripts to plot the multipath polar plots are taken from free source code available in GitHub[7].

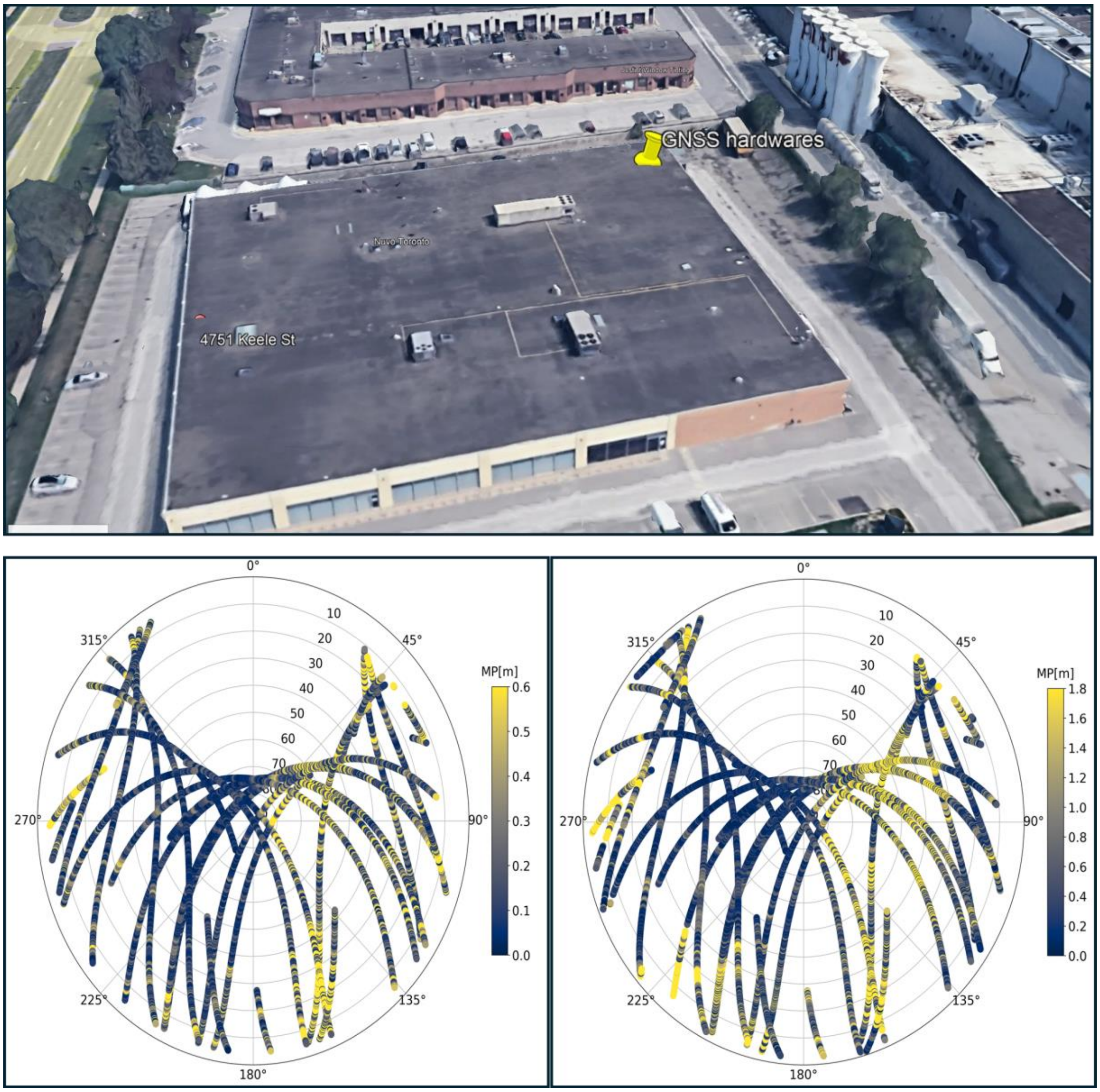

Figure 3.9: Site used for data collection (top); polar plot of multipath, azimuth and satellite elevation for geodetic hardware (bottom left), low-cost (bottom right) (DOY 355, 2023)

---

[7] https://github.com/paarnes/GNSS_Multipath_Analysis_Software

3.2.4 Cycle slips

A cycle slip is an abrupt change in the carrier-phase measurement by an integer number of cycles, which occurs when the phase lock loop (PLL) loses its lock on the signal. When the PLL is locked onto the signal, it can continuously track the integer and fractional parts, allowing the receiver to acquire accurate and consistent carrier-phase measurements. However, when a cycle slip occurs, it disrupts the continuity of phase observations, resulting in an unknown shift by an integer number of cycles (N) in the carrier-phase tracking. If uncorrected, this shift can significantly degrade positioning accuracy (Leick et al., 2015, p. 282). Cycle slips may happen briefly between measurement epochs or persist if the satellite signal cannot reach the antenna due to obstructions or interference such as satellite signal obstructions (e.g., buildings, trees), atmospheric disturbances, or hardware limitations (Hofmann-Wellenhof et al., 2007, p. 194). Thus, accurately detecting and repairing cycle slips is essential for maintaining precise carrier-phase measurements in GNSS positioning, especially in applications that require continuous and reliable data, such as geodetic surveying and autonomous navigation.

Consequently, two prominent methods for detecting cycle slips are used for further analysis: the geometry-free (GF) method and the ionospheric residual combination. GF uses the difference between the carrier-phase measurements of two frequencies (typically L1 and L2) to compute a geometry-free linear combination (Equation 3-9).

$$\phi_{GF} = \phi_1 - \phi_2 \tag{3- 9}$$

where, ϕ_1 is the carrier-phase measurement on the first frequency and ϕ_2 is the carrier-phase measurement on the second frequency. In a typical carrier-phase measurement, the observed phase includes the geometric distance between the satellite and receiver, receiver and satellite clock biases, tropospheric and ionospheric delays, and measurement noise. All terms independent of frequency are cancelled out, leaving only the frequency-dependent ionospheric delay component (Sanz Subirana et al., 2011) using the geometry-free combination. An abrupt change in this ionospheric component, which exceeds a predefined threshold, indicates a cycle slip, thereby flagging the slip for correction.

The ionospheric residual combination method examines the rate of change in ionospheric delay. Since ionospheric delay changes gradually under normal conditions, any sudden, substantial change in ionospheric delay is likely indicative of a cycle slip. By monitoring this rate of change, the ionospheric residual method can identify and localize cycle slips within the GNSS observation data. This combination removes the ionospheric component from the measurement, leaving mainly the geometric distance and other relevant positioning data (Sanz Subirana et al., 2011).

$$\phi_{IF} = \frac{f_1^2\phi_1 - f_2^2\phi_2}{f_1^2 - f_2^2} \tag{3-10}$$

where, ϕ_1 and ϕ_2 are the carrier-phase measurements on the first frequency (f_1) and second frequency (f_2).

Table 3.6 and Figure 3.10 illustrate the total cycle slip counts for geodetic and low-cost GNSS hardware over several dates. The cycle slip events, represented as counts, are plotted against dates on the x-axis, with the y-axis showing the total cycle slip counts. This comparison shows how often each type of hardware experiences cycle slips on specific days. The low-cost GNSS hardware shows relatively higher and more variable cycle slip counts across the dates. Notably, both hardware counts spike significantly on April 13, 2024. The significant rise in cycle slip counts on April 13 highlights that certain environmental or satellite-specific factors may impact GNSS performance, affecting both hardware types. On April 16, 2024, an opposite trend is observed from April 13, where geodetic hardware exhibits approx. 7% more cycle slip counts than low-cost hardware. This provides a clue that though low-cost devices have hardware limitations, it performs comparable to the geodetic hardware in terms of cycle slips under optimal environments. The results from April 16 seem interesting, and hence, further analysis is done through visual representation of cycle slip count vs time.

Table 3.6: Cycle slip events encountered on different days for measurements from geodetic and low-cost hardware

Cycle slips events	2023-12-13	2023-12-21	2023-12-30	2024-04-13	2024-04-16
Geodetic	270	202	228	1258	1088
Low-cost	410	476	250	1255	1016

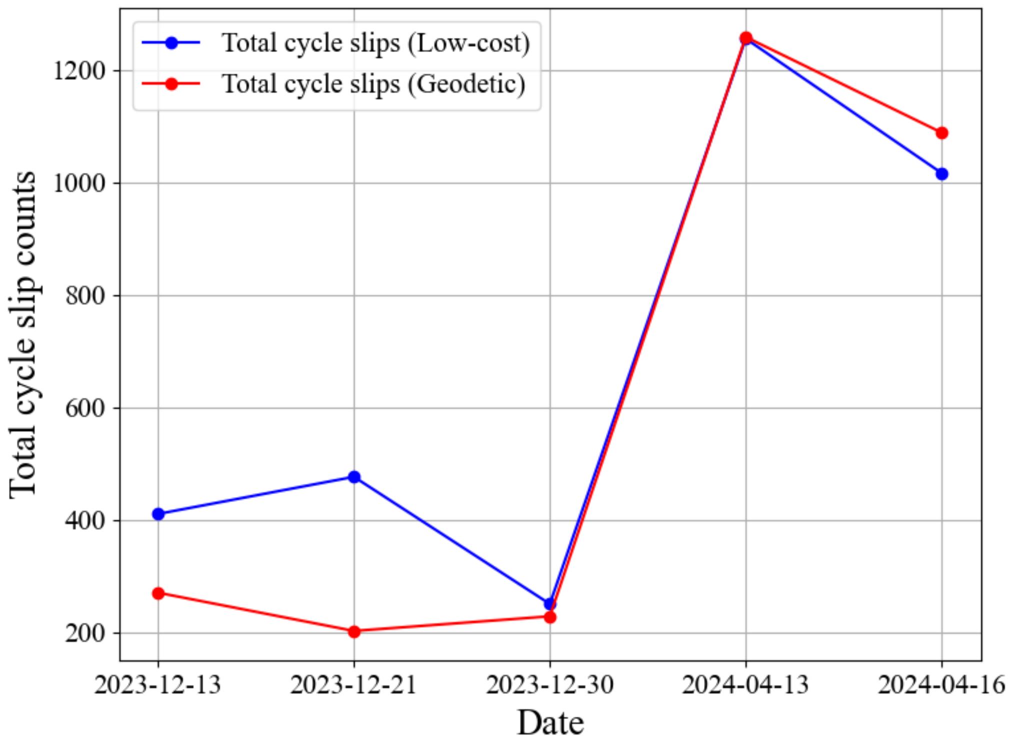

Figure 3.10 Total cycle slips events encountered in sample days for measurements from geodetic hardware (blue) and low-cost hardware (red)

Figure 3.11 provides a comparative view of cycle slip occurrences across geodetic and low-cost GNSS hardware on two specific dates, April 13 and April 16, 2024, where the high count was noticed. This visualization highlights the temporal distribution of cycle slips detected by both hardware types, with each subplot capturing the events for each device over time of the observations. The rationale for examining cycle slips over time is to identify any unusual patterns or trends in their occurrence. The cycle slips appear clustered around similar time epochs for geodetic and low-cost hardware on both dates. This synchronicity in cycle slip occurrences illustrated in Figure 3.11 suggests that the underlying causes could be external, such as atmospheric disturbances, ionospheric irregularities, or multipath effects, rather than hardware-specific issues.

Furthermore, a distinct pattern in cycle slip counts was observed on April 16 as shown in Figure 3.11, where the geodetic hardware experienced more cycle slips than low-cost hardware. A black box highlights the period around 7:00 hrs in both plots, drawing attention to the temporal change in cycle slip events. This focused time frame reveals a spike in cycle slips for the geodetic hardware, which contributes significantly to the overall difference in cycle slip counts between the two hardware types on this date.

In conclusion, while both hardware types experience cycle slips at similar times, the frequency of events varies. Low-cost hardware tends to encounter more cycle slips than geodetic hardware, though there are instances, such as on a particular day, where the low-cost hardware performs comparable or even better. These results suggest the need for further testing to gain a deeper understanding of cycle slip behaviour in low-cost hardware.

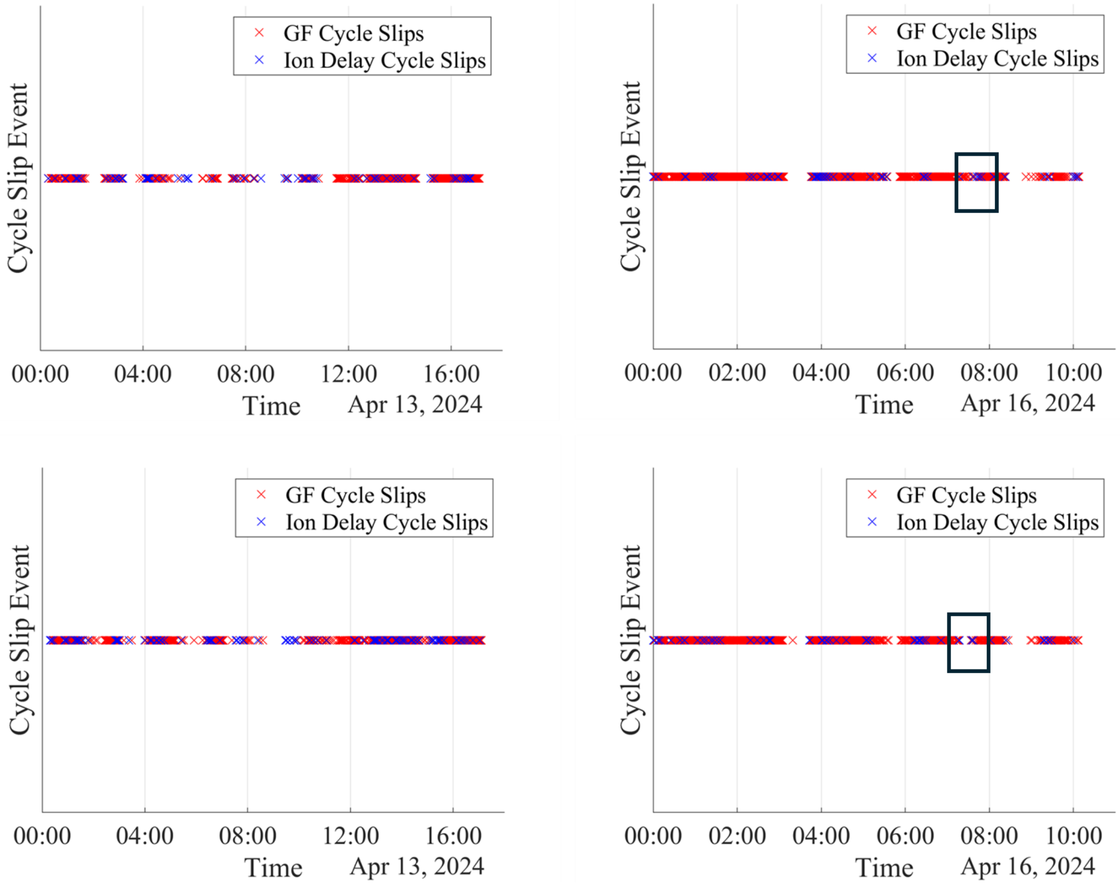

Figure 3.11 Cycle slip events encountered on April 13 and 16, 2024, on measurements of the geodetic hardware (top) and low-cost hardware (bottom)

3.2.5 Data gaps and availability

Data gaps or missing measurements in GNSS observations can stem from various causes. Non-line-of-sight (NLOS) signals, where satellite signals reflect off obstacles rather than reaching the receiver directly, leading to complete loss of phase lock. Similarly, multipath and obstructions from structures like buildings or natural elements such as trees can block satellite signals entirely, resulting in data gaps. Atmospheric disturbances, including ionospheric and tropospheric delays, also contribute, with effects intensifying during periods of high solar activity. Cycle slips contribute to data loss. Additional factors, such as interference from nearby electronics, power interruptions, or inadequate processing power, can disrupt signal lock, creating discontinuities in carrier-phase data (Sennott, 1999). These data gaps are particularly problematic as they disrupt carrier-phase continuity, which is essential for resolving ambiguities and achieving high precision.

The dataset described in Table 3.3 was analyzed to see the data gaps. The geodetic and low-cost hardware were placed in the same multipath environment, and observations were taken simultaneously. Table 3.7 presents the percentage of missing phase measurement observables for geodetic and low-cost hardware across three frequencies. The percentage of missing phase observations is calculated by excluding the satellites that do not transmit any third frequency measurements so that statistics do not get biased.

The results show a contrast in the performance of geodetic versus low-cost receivers regarding data continuity. Across all three frequencies, the geodetic receiver exhibits significantly fewer data gaps than the low-cost receiver. Specifically, for the first frequency, geodetic receivers experience only 0.5% of data gaps, whereas low-cost receivers have 8.3%, which is approximately 16 times higher. Similarly, on the second frequency, the geodetic receiver has a 1.3% gap, while the low-cost receiver shows a much higher rate of 9.8%. This trend continues the third frequency, with geodetic receivers showing only 0.5% missing data, compared to 8.3% for low-cost receivers.

Table 3.7: Percentage of phase measurement gaps in different frequencies in observation from geodetic and low-cost hardware

Receivers	Phase measurement gaps in percentage		
	First frequency	Second frequency	Third frequency
Geodetic	0.5	1.3	0.5
Low-cost	8.3	9.8	8.3

3.3 Measurement analysis summary

Geodetic and low-cost hardware measurements over 72 hrs were analyzed using different quality metrics. Compared to the geodetic hardware, measurement from low-cost hardware consistently shows a gap of 7 dB Hz in average C/N_0 values around the three frequencies. The low-cost hardware shows notable variability at the second frequency, with C/N_0 extending as low as 20 dB Hz. Additionally, the third frequency reveals a significant C/N_0 difference of 10 dB Hz compared to the geodetic hardware.

Pseudorange noise, analyzed through the CMC linear combination, indicated that low-cost hardware exhibits approximately 5.5 times more noise at the first frequency, 2.6 times more at the second, and 3.6 times more at the third, compared to geodetic hardware. Multipath effects were also assessed using a linear combination approach, revealing that low-cost hardware experiences between 3 to 5 times more multipath interference than geodetic hardware. The investigation into cycle slip events across sample days showed that low-cost hardware generally encountered more slips, though there were days, such as April 16, where geodetic hardware experienced a higher slip count. Additionally, an assessment of data continuity in phase measurements highlighted that low-cost GNSS hardware suffers from significantly more data gaps than geodetic hardware, with up to 16 times more missing observations on certain frequencies.

This comprehensive analysis underscores that, while low-cost GNSS hardware can perform adequately under optimal conditions, it is generally more susceptible to noise, multipath effects, and data gaps than geodetic hardware. For applications requiring continuous and high-precision data, geodetic hardware remains the preferable choice.

Chapter 4 Customizing data processing for improved low-cost solutions

Based on the findings from the comparative analysis of measurements from geodetic and low-cost hardware, further customization on data processing was implemented. This discussion forms the central contribution of this study. The first section describes the customizations made to the YorkPPP GNSS processing engine to better process the observations from low-cost hardware. The second section examines the relationship between carrier-to-noise density, carrier-phase standard deviation, and measurement noise. This section also explores the detailed distribution of C/N_0 from geodetic and low-cost hardware. The third section introduces an empirical observation weighting scheme based on the C/N_0. This scheme is then compared with existing methods.

4.1 Customization of the YorkPPP processing engine

The YorkPPP processing software is a GNSS measurement processing tool designed to process the GNSS measurement for PPP solutions. It supports all GNSS constellations. Developed in Visual Studio using C++, the YorkPPP engine was initially designed for measurements from geodetic receivers. As a result, modifications are necessary to adapt it for processing data from low-cost GNSS receivers.

York PPP engine has its origins in the CSRS-PPP online service and was later rebuilt and extended (Seepersad, 2012, pp. 42–50; Aggrey, 2015, pp. 19–37). The first customization integrates BeiDou observation types L7D, L5P, and C7D into the processing code. The low-cost mosaic-X5 receiver tracks these signals. These observables correspond to new signals introduced in the BeiDou-3 constellation, including B2a (associated with L5P) and B2b (associated with L7D and C7D). The B2a signal was released in December 2017,[8] and the B2b signal became available in July 2020. The reader for satellite code and phase biases related to these signals were also incorporated to utilize all available observables from the low-cost hardware.

Following the assignment of observables, elevation angle and carrier-to-noise density ratio rejection thresholds are customized. These thresholds filter out unreliable measurements to pass into the adjustment filter. An elevation angle threshold of 7.5^0 and a C/N_0 threshold of 10 dB Hz are used. All existing pre-processing quality checks, including the cycle slips detection algorithm, are used as they are. Once the measurements pass initial quality control checks, they are processed by a sequential filtering algorithm to estimate the state terms, including the positioning solution. An empirically defined rejection threshold is applied in the post-fit residuals check, similar to the approaches of Shinghal & Bisnath (2021) and Everett et al. (2022) where the residual larger than four times the a posteriori variance will be rejected. For code measurements, the post-fit rejection threshold is set at 10 m for low-cost hardware, while for phase measurements, the threshold is set at 0.04 m. This stricter threshold for phase measurements is appropriate for geodetic-grade applications, as it ensures the identification of even slight deviations that could compromise the integrity of the solution. In contrast, for the measurements from geodetic hardware, the same rejection threshold is used for the phase, and a stricter code rejection threshold of 4.4 m is used.

---

[8] http://en.beidou.gov.cn/SYSTEMS/ICD/201806/P020180608518432765621.pdf

4.2 Relevance of carrier-to-noise density ratio and elevation angle in observation weighting

The functional and stochastic models collectively provide a comprehensive framework for modelling observations and estimating unknown parameters. The functional model defines the deterministic relationships linking the observed data with the variables that need to be estimated (Teunissen & Amiri-Simkooei, 2008). The functional model specifies how the observations are expected to behave in an ideal, error-free scenario. Observations are never perfect due to various noise sources and errors, making a stochastic model essential for accounting for these imperfections. The stochastic model characterizes the random errors associated with the observations. The stochastic model quantifies these errors, often assuming they follow a particular statistical distribution (e.g., Gaussian).

In data processing, the correct specification of functional and stochastic models is paramount for accurate and reliable positioning. The functional model must comprehensively represent the physical and geometrical relationships between the satellite signals and the unknown parameters, accounting for all significant influences on the signal propagation. The stochastic model must accurately characterize the measurement errors guiding the estimation process's weighting of observations. This plays a crucial role in correct parameter estimation and integer ambiguity resolutions, increasing the precision and reliability of GNSS solutions (Li et al., 2008; Teunissen, 2007; Tiberius & Kenselaar, 2000).

In GNSS, equal-weight, elevation-based and C/N_0-based models are used as stochastic models to model measurement uncertainty. In this model, regardless of satellite elevation, signal strength, or environmental conditions, each measurement is assigned an identical weight during data processing. These models lead to the inefficient weighting of observations and reduced positioning accuracy. (Collins & Langley, 1999; Bischoff et al., 2005; P. J. G. Teunissen & Kleusberg, 1998). The elevation-based model allocates weights to GNSS observations according to the elevation angles of the satellites in relation to the receiver. Observations from satellites at higher elevation angles are considered more reliable and are given higher weights. The model typically uses a mathematical function, such as the sine of the elevation angle, to determine the weights (Collins & Langley, 1999). The C/N$_0$-based model utilizes the carrier-to-noise density ratio as a signal quality metric to assign weights to GNSS observations. In this model, observations with higher C/N$_0$ density ratios are assigned higher weights (Collins & Langley, 1999; Hartinger & Brunner, 1999). The details methodology of this model is further discussed in Section 4.3.3.1 and Section 4.3.3.2.

4.2.1 Phase standard deviation and carrier-to-noise density ratio

The measurement noise in the receiver's Delay Lock Loop (DLL) for code tracking and its Phase Lock Loop (PLL) for phase tracking directly depends on the C/N$_0$ of the received signal (Teunissen & Montenbruck, 2017a, p. 579).

The noise of the carrier-tracking loop described by Langley (1997) can be expressed as:

$$\sigma_{PLL} \approx \sqrt{\frac{C_L}{cno}\frac{\lambda}{2\pi}} \tag{4-1}$$

where σ_{PLL} is the standard deviation of the carrier-phase lock loop in m, $cno = 10^{-\left(\frac{C/No}{10}\right)}$ in dB Hz is the carrier-to- noise density ratio, λ is the wavelength corresponding to the carrier frequency used in the signal (L1,L2..) and C_L is the carrier loop tracking bandwidth in Hz, which defines the bandwidth of the PLL used to track the carrier signal phase. The carrier loop tracking bandwidth is an essential parameter in PLL systems. Narrow bandwidths, as highlighted by Braasch & van Dierendonck (1999), are sufficient for ensuring low-phase noise.

Low-phase noise is critical for maintaining minimal phase fluctuations, ensuring stable tracking in high-SNR and minimal multipath environments.

According to Septentrio (2020, p. 94), PLL bandwidth for mosaic-X5 receivers varies from 1 to 100 Hz. For instance, the PLL bandwidth for the geodetic G-III reference receiver from NovAtel is 0.2 Hz for the L2P(Y) signal and 3 Hz for other signals provided in the product spreadsheet (Hexagon | NovAtel, 2020). Further analysis is done using Equation (4-1) to understand the phase noise between the different carrier tracking loop bandwidths. For this analysis, the loop tracking bandwidth is varied of 0.3, 3, 10, 25, and 100 Hz to evaluate different bandwidths of geodetic and low-cost hardware to know the performance of the carrier-phase lock loop. For GPS signals, the wavelength (λ) is determined based on the carrier-frequencies: L1 (190. cm), L2 (24.4 cm), and L3 (25.4 cm). C/N_0 values are assumed at fixed intervals of 0.1 for testing purposes. These simulated C/N_0 values are then substituted into Equation (4-1) and the standard deviation of the carrier-phase lock loop is calculated.

Table 4.2 reveals that the phase noise in carrier-phase measurements varies significantly with PLL bandwidth. The standard deviation of the carrier-phase lock loop noise is calculated with carrier tracking loop bandwidth from 2 to 100 Hz using Equation (4-1) with C/N_0 30 dB Hz. At narrow bandwidths, such as 0.2 Hz, typically used by geodetic receivers, phase noise remains minimal (below 0.5 mm) with negligible differences between L1, L2, and L5 frequencies. In contrast, at higher bandwidths (25 to 100 Hz) commonly adopted by low-cost receivers, phase noise increases substantially, reaching 4.7 to 9.5 mm, equivalent to 2.5-5% of each frequency's respective wavelength. Additionally, phase noise values diverge more noticeably between L1 and L5 at these wider bandwidths. Two major findings can be summarized from this analysis:

1. For GPS L1 with a wavelength of 19.01 cm, phase noise at a PLL bandwidth of 0.2 Hz represents only 0.2% of the total wavelength. The PLL bandwidth determines the frequency range over which the receiver tracks phase variations of the incoming signal. Narrow bandwidths, such as 0.2 Hz, effectively filter noise, resulting in lower phase noise. However, as PLL bandwidth increases to 100 Hz, the loop's ability to track rapid phase variations improves but allows more noise to influence the signal. This increase in PLL bandwidth causes the fraction of the phase noise relative to the wavelength to rise to 5%, demonstrating that phase noise occupies a more significant portion of the wavelength at higher bandwidths, thereby impacting measurement precision.
2. Although phase noise differences across frequencies (L1, L2, L5) are negligible at narrow bandwidths, they become more pronounced at higher PLL bandwidths. This relationship suggests that phase noise is reflective through C/N$_0$ and differs according to frequency, particularly under conditions of wider PLL bandwidth.

Table 4.1: Final phase standard deviation at the C/N$_0$ of 30 dB Hz on GPS L1, L2, and L5 frequencies

C_L (Hz)	L1 (mm)	L2 (mm)	L5 (mm)
0.2	0.4	0.5	0.5
3	1.6	2.1	2.2
10	3.0	3.8	4.0
25	4.7	6.1	6.4
100	9.5	12.2	12.8

4.2.2 Noise assessment with carrier-to-noise density ratio and elevation angle

In this thesis, noise assessment is done using the CMC linear combination (Equation 3-7). Details on CMC can be found in Section 3.2.2. The code noise is assessed following the process outlined by De Bakker et al. (2009), which includes first finding the code-minus-carrier observables fitting a low-order polynomial to CMC residuals and later subtracting the fitted polynomial from the CMC observables, resulting in residual noise. Measurements from low-cost hardware are only taken for the noise analysis. Figure 4.1 provides a summary of this process.

Low-order polynomial fitting and subtracting from CMC observables minimized the slowly varying components, including carrier-phase ambiguity, low-frequency multipath, and low-frequency ionospheric delay. The term residual noise refers to the remaining noise components in the CMC observables after the slowly varying components have been removed through polynomial fitting. After removing the slowly varying components, the residual noise of CMC consists of twice the high-frequency ionospheric delay, high-frequency code multipath, and code noise. This polynomial fitting process essentially functions as a filter, isolating the rapidly varying noise components. The residual noise left after filtering is then analyzed to explore its relationships with C/N_0 and elevation angle. The Pearson correlation coefficient is used to quantify these relationships. The Pearson correlation coefficient (r) determines the degree of linearity between the variables from -1 to +1. Here, $r = 1$ indicates a perfect positive linear correlation, $r = -1$ indicates a perfect negative linear correlation, and $r = 0$ suggests no linear relationship. The study used the calculation strategy for the coefficient provided in the SciPy documentation (The SciPy Community, 2014).

Figure 4.1: Process of code noise estimation use for single receiver

The assessment is divided into two sets: the first examines the correlation of noise with low-elevation angles and C/N_0, and the second analyzes the correlation of noise with high-elevation angles and C/N_0. Similar results were observed across all datasets detailed in Table 3.3; therefore, DOY 107 is taken as a representative sample for the analysis. Figure 4.2 comprises four distinct subplots illustrating the analysis of PRN 12 over time. The first plot displays the CMC combination in blue and a low-order polynomial fit in red. The second plot presents the residual noise, which is obtained by subtracting the fitted values from the CMC. The third plot illustrates the C/N_0 over time, and the fourth plot shows elevation over time.

The polynomial effectively fits the CMC observable in the first plot, as shown in Figure 4.2. The residual noise, shown in the second plot, remains relatively small and stable over time with minor spikes. A clear correlation between residual noise and C/N_0 is observed: around 04:15 and the end of the observation period, highlighted by a red oval in Figure 4.2, as C/N_0 decreases, the residual noise gradually increases. Since slow-varying ionospheric delay has minimal effect on the fitted residuals, the spikes on the CMC (first plot) and noise (second plot) are for a short duration, indicating the high-frequency pseudorange multipath that affects the signal.

As illustrated in Table 3.2, the low antenna gain pattern of patch antenna effects is seen on the measurement when satellite is setting to horizon. As a result, C/N_0 values are gradually decreasing while the satellite is setting (third plot), which is reflected on the residual noise in the second plot. When C/N_0 stabilizes, the residual noise stabilizes near zero, indicating a direct relationship between signal quality and measurement noise. However, no direct relationship between residual noise and elevation is apparent. Nevertheless, it can be said that as elevation increases, C/N_0 increases, which in turn leads to a reduction in measurement noise. This analysis provides insights that especial consideration should be taken in quality control so that satellite with low elevation has minimal effects on the positional solutions.

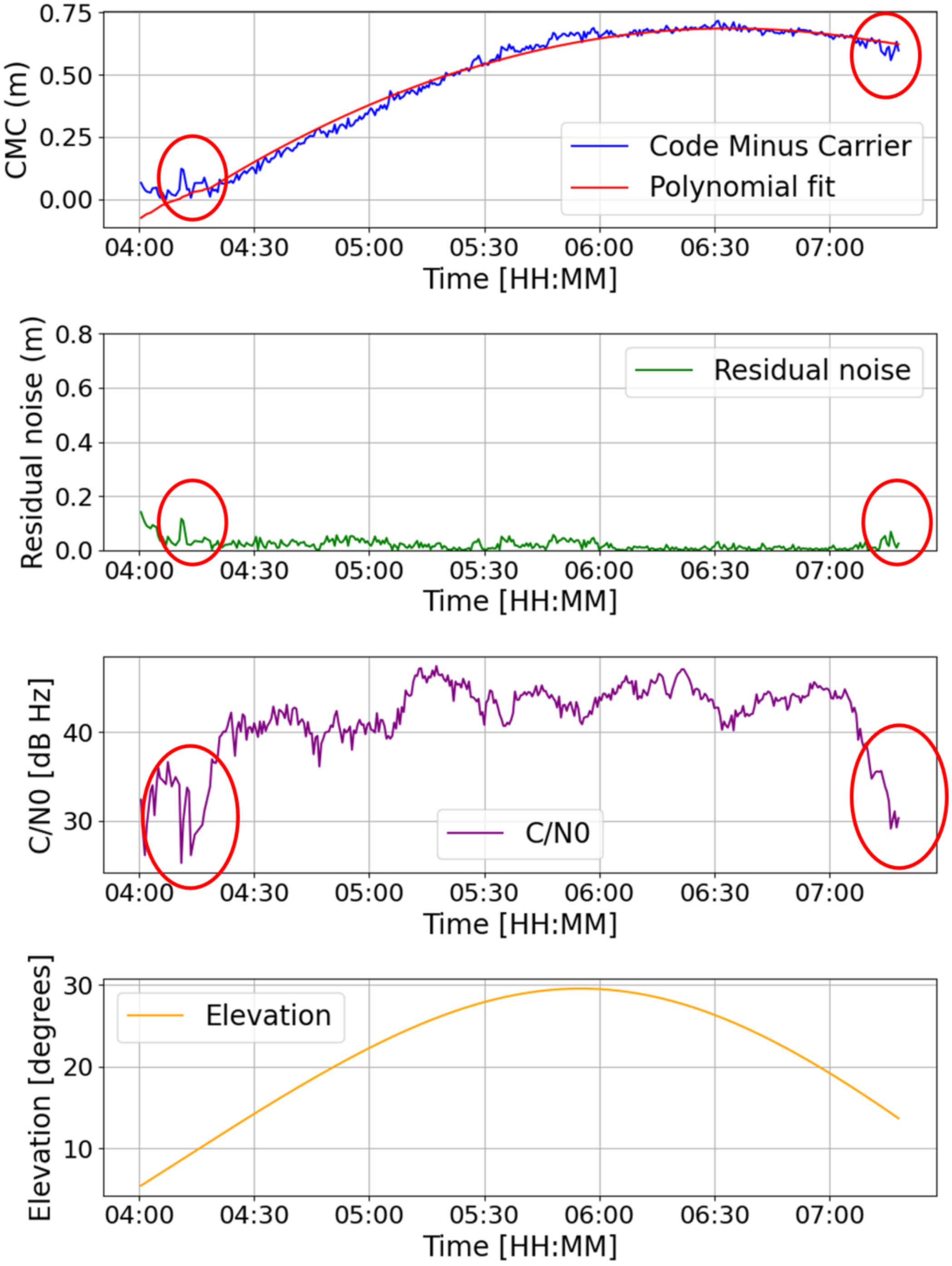

Figure 4.2: CMC residuals and fitting polynomial (first), high-frequency noise component and time (second), first frequency C/No and time (third), and elevation angle and time (fourth) of GPS PRN 12, low-cost data, DOY 107, 2024

4.2.2.1 Correlation analysis of low elevation angle satellites, carrier-to-noise density ratio and residual noise

The residual high-frequency noise component from the CMC combination is used in correlation analysis with C/N_0 and satellite elevation angle. The relationships between residual noise and C/N_0 and low elevation angle below 40^0 are analyzed for six satellites (GPS PRNs 11, 12, 20, 30, GLONASS PRN 03, and Galileo PRN 03) in Figure 4.3. The first frequency carrier-to-noise density ratio is analyzed for this subsection as it is a primary frequency in GNSS. The reason for choosing these specific satellite PRN is that satellites were observed in low-angle below 40^0 all over the observation period, each for a longer duration. Each subplot displays the correlation coefficient (r) between these variables for the low-cost receivers.

In all cases, as illustrated in Figure 4.3, residual noise shows a negative correlation with C/N_0 and satellite elevation angle. For instance, both GPS PRN 11 and 12 exhibit a moderate negative correlation with C/No (r = -0.49), while the noise-elevation correlation is notably weaker (both at r = -0.24). Conversely, GPS PRN 30 and Galileo PRN 3 have a moderate correlation with C/N_0 (r = -0.52 and r = -0.43) but little correlation with elevation (r = 0.08 and r = - 0.12). PRN 20 exhibits the highest correlation with C/N_0 (r = -0.85) and moderate noise-elevation correlation (r = -0.67).

In summary, the correlation analysis demonstrates that the signal quality decreases as satellites approach the horizon, increasing residual noise due to high atmospheric interference and multipath. This effect is related to an inverse relationship between tropospheric slant delay and elevation angle (Teunissen & Montenbruck, 2017b, p. 569). At low elevation angles, GNSS signals experience high tropospheric slant delay. Slant delay is calculated using a mapping function that adjusts the delay measure at the zenith to match the actual path taken by the signal to the receiver. The result demonstrates that in low elevation angles, the C/N$_0$ negatively correlates to the noise compared to elevation angles. These findings are useful in refining weighting schemes for GNSS observations, improving correction models for tropospheric delay, and designing algorithms that mitigate low-elevation signal degradation.

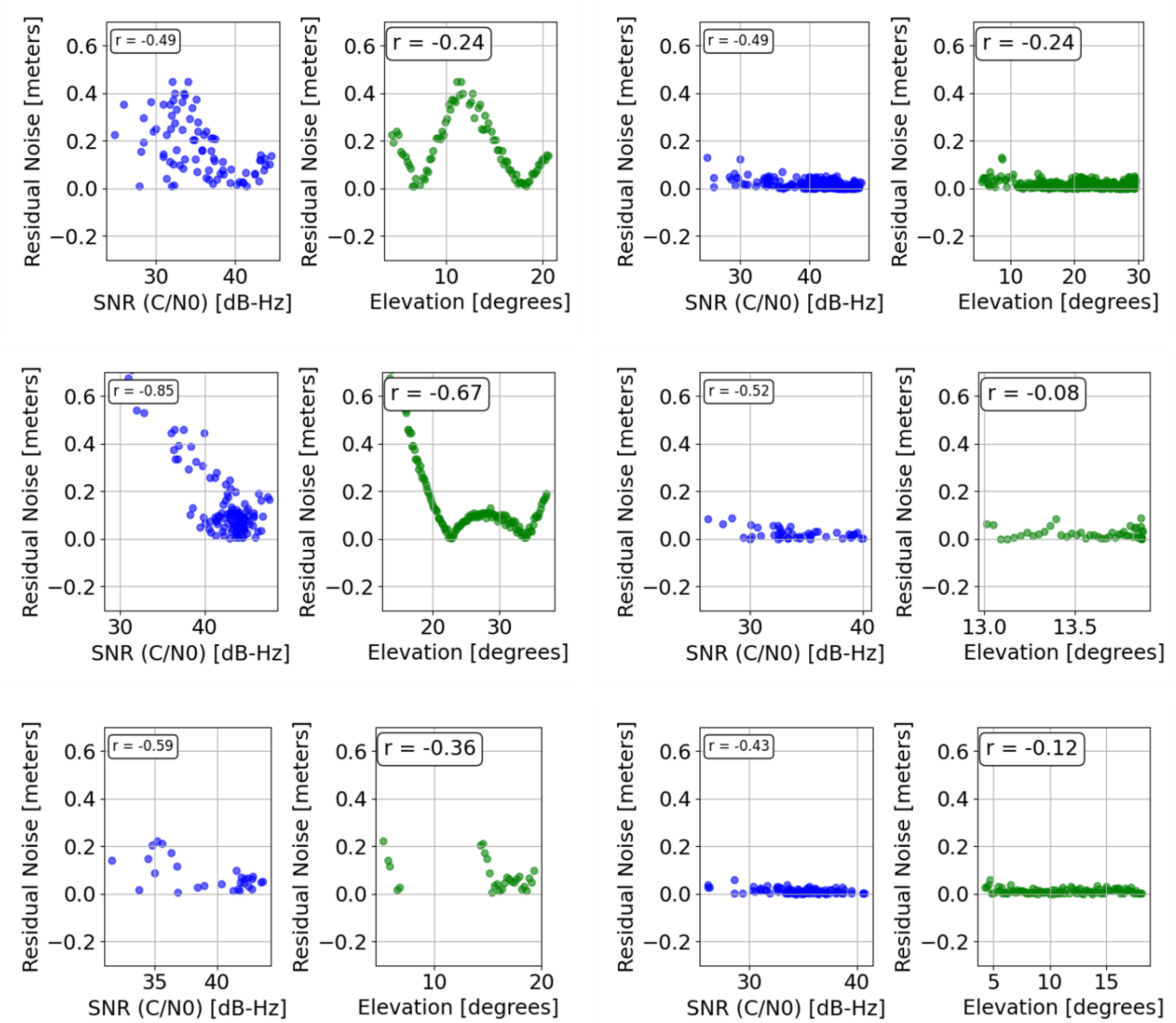

Figure 4.3: Correlation analysis of residual noise with C/N$_0$ (blue) and residual noise with low-elevation angle (green) for the DOY 107 across satellites with GPS PRNs 11, 12, 20, 30; GLONASS PRN 03; and Galileo PRN 03 (arranged top-left to bottom-right. r is the Pearson correlation coefficient)

4.2.2.2 Correlation analysis of high elevation angle satellites, carrier-to-noise density ratio and residual noise

Figure 4.4 compares noise correlation with C/N_0 and elevation across six satellites: GPS PRNs 17, 18, GLONASS 1, 2, 12, and Galileo PRN 05, using a high elevation angle of 35^0-75^0 to understand the relationship of noise with signal indicators. This analysis provides insights into how elevation and C/N_0 affect the residual noise from the CMC combination.

The analysis using Pearson correlation, as shown in Figure 4.4, reveals that the correlation coefficients between noise and elevation range from r = -0.2 to r = -0.4, while the correlation coefficients between noise and C/N_0 range from r = -0.2 to r = -0.6 across GPS, GLONASS and Galileo satellites. The strongest negative correlation for noise and elevation is r = -0.4, and the strongest negative correlation for noise and C/N_0 is r = -0.6. These results indicate that both satellite elevation angle and C/N_0 exhibit a medium negative correlation with noise.

In conclusion, the following key insights can be revealed. A moderate negative correlation exists between noise and C/N_0 at high satellite elevation ranges, while noise shows almost no correlation with elevation at lower elevation angles. At lower satellite elevation angle, the correlation between noise and elevation is weak. However, as elevation angle increase, the negative correlation between noise and C/N_0 and elevation becomes similar. Therefore, optimizing satellite signal quality at high elevation angles may require considering both C/N_0 and elevation jointly to achieve noise interference. For satellites at low-elevation angles, C/N_0 is the primary factor indicating noise level for low-cost hardware, as elevation alone shows minimal correlation with noise (Figure 4.4). This discussion highlights the carrier-to-noise density ratio for pre-processing and outlier detection.

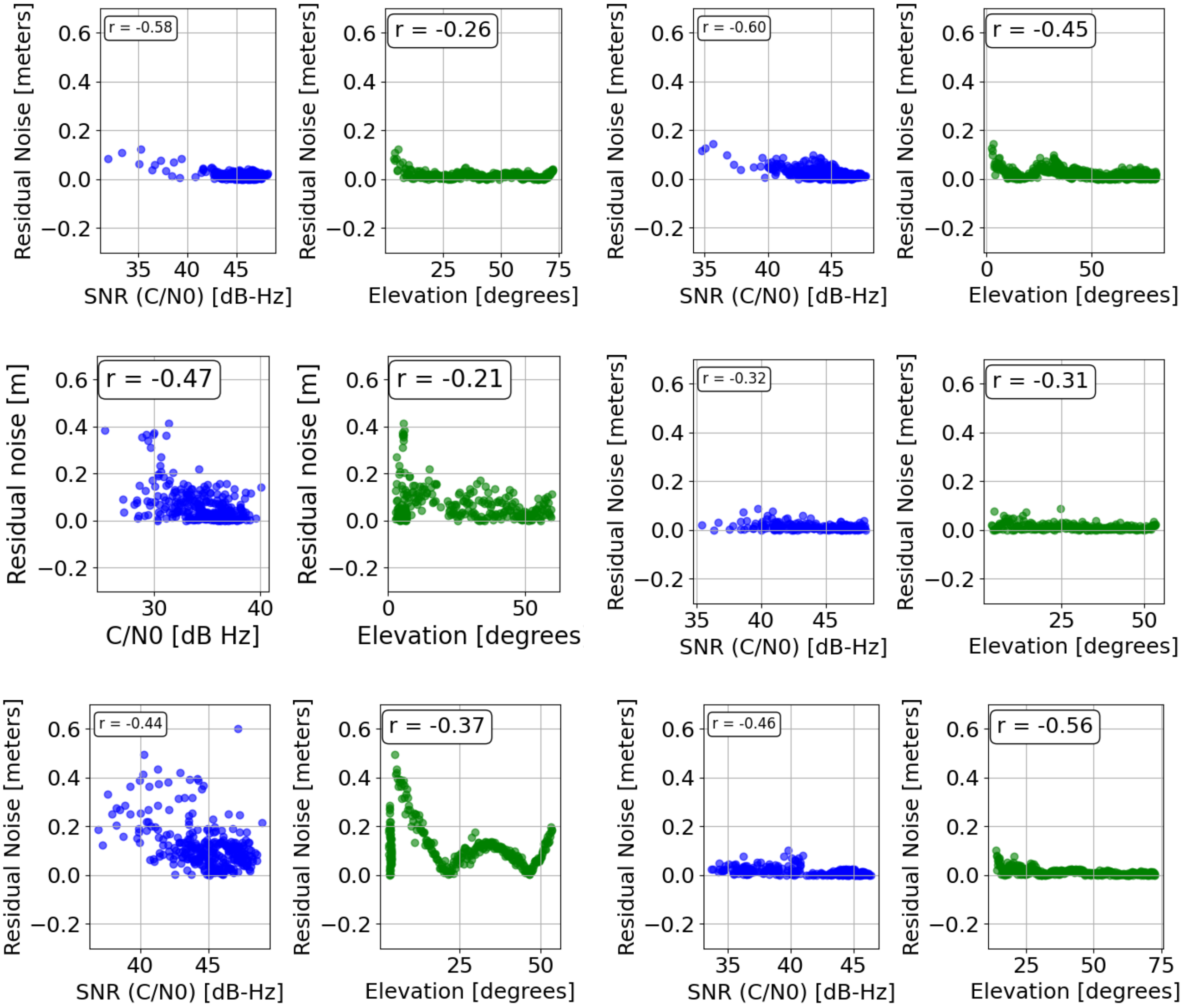

Figure 4.4 Correlation analysis of residual noise with C/N$_0$ ratio (blue) and residual noise with high-elevation angle (green) for the DOY 107 across satellites with GPS PRNs 17, 18; GLONASS PRNs 1, 2,12; and Galileo PRN 05 (arranged top-left to bottom-right). r is the Pearson correlation coefficient.

4.2.3 Carrier-to-noise density ratio in geodetic and low-cost measurements

GNSS signals are transmitted on multiple frequencies (e.g., L1, L2, L5), and the C/N$_0$ distribution varies depending on the frequency. Geodetic receivers have advanced signal processing capabilities, and high-quality antennas can maintain higher C/N_0 across elevations and frequencies. In contrast, low-cost receivers with lower-quality antennas and less sophisticated signal processing are more susceptible to signal degradation, especially at low elevations. Therefore, before applying the same stochastic models used for geodetic hardware, it is essential to evaluate whether both types of hardware exhibit similar behaviour across various frequencies and elevation angles. C/N_0 from geodetic and low-cost receivers are grouped into 10^0 elevation intervals from 0 to 90^0 to evaluate the C/N_0 distribution of GNSS hardware across different elevation ranges. This distribution is then visualized using violin plots to facilitate comparative analysis.

Figure 4.5 shows the C/N_0 distribution for geodetic (top) and low-cost (bottom) hardware across 10^0 elevation intervals for three frequencies. A red line at 44 dB Hz marks the minimum threshold for reliable GNSS signals (Brunner et al., 1999; Hofmann-Wellenhof et al., 2007). Geodetic hardware consistently achieves higher C/N_0 values across all elevation ranges for each frequency, with maximum values ranging from 55-60 dB Hz, while low-cost hardware peaks at 45-50 dB Hz, a notable 10 dB Hz lower than geodetic hardware. Due to the logarithmic C/N_0 scale, this 10 dB Hz gap significantly increases noise power, amplifying the impact of multipath and atmospheric interference.

Geodetic hardware consistently crosses the 44 dB Hz threshold starting from 20^0-30^0 of elevation for each frequency, whereas low-cost hardware only reaches this signal strength level at 50^0-60^0. At lower elevations (0-30^0), low-cost hardware often fails to meet the 44 dB Hz threshold. This instability is further pronounced on second and third frequencies for low-cost receivers, where nearly half of the signals fall below the 44 dB Hz threshold, even at higher elevations. These findings demonstrate that geodetic and low-cost hardware performance is not similar, with geodetic hardware offering more reliable signal quality across elevation ranges.

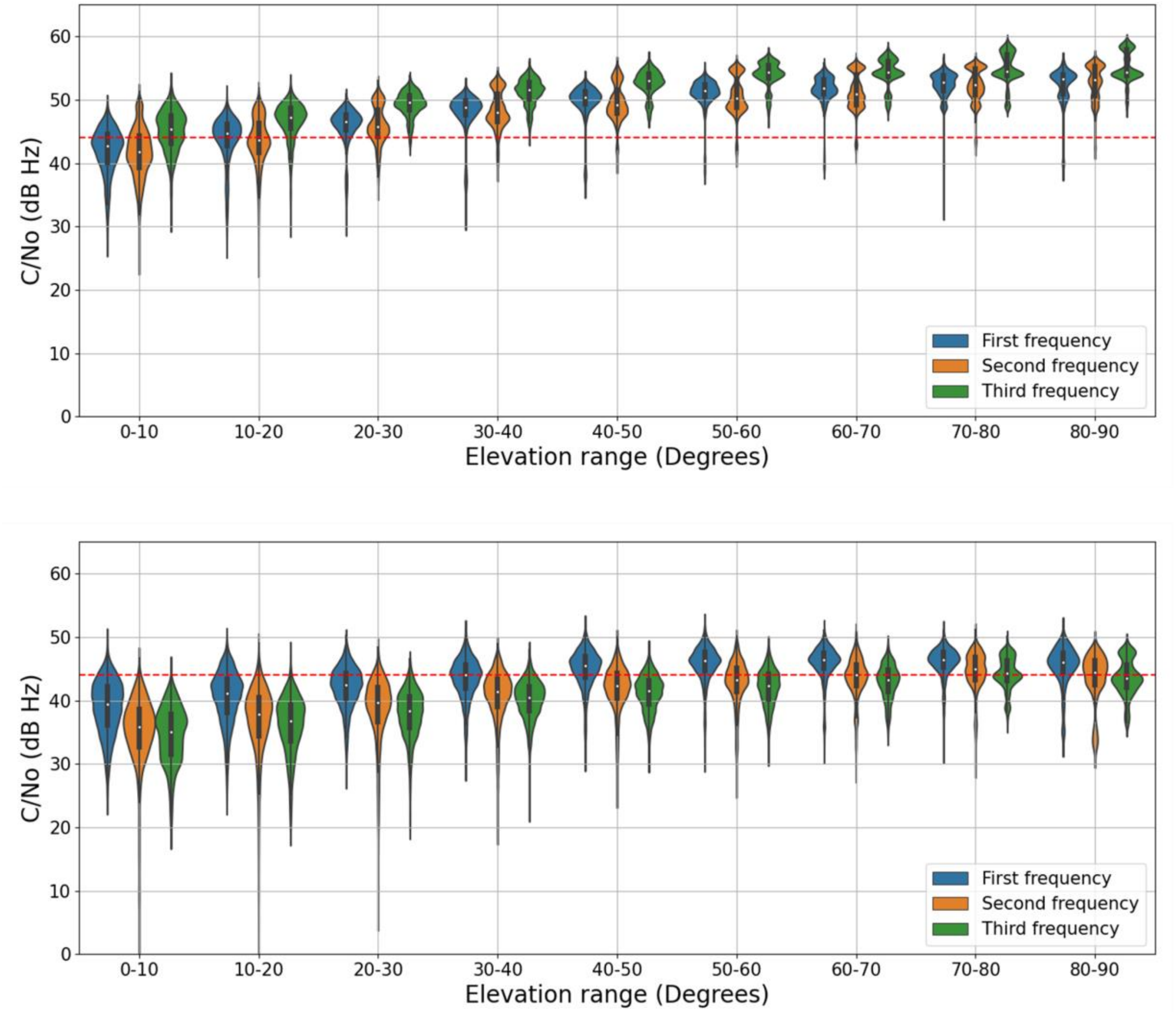

Figure 4.5 C/No distribution of geodetic datasets (top) and low-cost datasets (bottom) at 10 dB Hz interval. Red line is a threshold of 44 dB Hz

Exploring the relevance of C/N$_0$ and elevation angle in observation weighting, the analysis investigates how C/N$_0$ and elevation angle contribute to phase noise and measurement noise, comparing measurements from geodetic and low-cost hardware. Findings demonstrate that these factors impact signal strength, indicating that a nuanced approach to weighting is essential.

Carrier loop tracking bandwidth is directly proportional to phase noise, with higher bandwidths resulting in higher phase noise levels (Table 4.1). Geodetic receivers typically use smaller carrier loop tracking bandwidth, making them less affected by this phenomenon. In contrast, low-cost receivers, such as the Mosaic-X5 (Septentrio, 2020) have bandwidths ranging from 1 to 100 Hz, leading to more significant phase noise. For instance, at a 25 Hz carrier loop bandwidth, phase noise increases by approximately 29% from L1 to L2 and 36% from L1 to L5. The elevation-based weighting scheme fails to capture these variations in noise across frequencies.

As summarized in Section 4.2.2, there is a negative correlation between noise and C/N_0 observed in low-cost measurements at a low elevation angle. In contrast, no significant correlation exists between noise and elevation angles. This finding supports the argument that, for low-elevation angles, C/N_0 is a more reliable noise indicator in observations from low-cost receivers.

For low-cost hardware, achieving a nominal C/N_0 signal threshold at the first frequency typically requires 50^0-60^0 elevation angles. However, for the second and third frequencies, more than half of the signals fail to meet the threshold even at higher elevation angles. This indicates that observations need adjusted weighting strategies in measurements from low-cost hardware to optimize the performance using these measurements.

4.3 Observation weighting using carrier-to-noise density ratio for low-cost hardware

The analysis in Section 4.2 suggests that, for low-cost receivers, C/N_0 is a crucial signal quality indicator, particularly for satellites at low elevation angles. Appropriate observation weighting where a higher weight to a precise observation and lower weight to less reliable observation (those with low C/N_0), can enhance positional solution. This section explores the realization of a new C/N_0-based observation weighting scheme.

4.3.1 Model realization

Building on Langley's (1999) work on the relationship between carrier loop noise and C/N_0, Hartinger & Brunner (1998b, 1998c) conclude that carrier-to-noise density ratios are an actual quality indicator of phase noise, and using C/N_0-based phase variance allows for appropriate weighting of satellites at lower elevation angles. Further studies by Brunner et al. (1999) and Wieser and Brunner (2014) demonstrated the effectiveness of using C/N_0 in observation weighting, accounting for site-specific signal diffraction and multipath for geodetic measurements. Furthermore, C/N_0 is used in the observation weighting for measurement from low-cost receivers. However, cm-level accuracy remains a challenge, primarily due to the low-cost hardware being susceptible to noise and multipath (Luo et al., 2009; Yuan et al., 2022; Y. Li et al., 2023).

Analyzing results from Sub-section 3.2.1.1, a notable average discrepancy of 7 dB Hz C/N_0 gaps in measurement from low-cost hardware is seen compared to geodetic ones. This finding is further substantiated in Section 4.2.3, which states that the performance of low-cost hardware is not similar to geodetic hardware, where geodetic hardware offers more reliable signal quality even in low-satellite elevation angles. In light of these findings, further analysis was done using the same datasets in Chapter 3 (see Table 3.3). Five days of data from low-cost and geodetic hardware was compiled and analyzed. The C/N_0 were grouped into 10 dB Hz intervals, and histogram of the percentage of observations falling within the interval was plotted. This analysis aimed to evaluate the frequency of occurrence of C/N_0 above 44 dB Hz across the observation period in both hardware types.

The threshold of 44 dB Hz is particularly important, as it represents the nominal signals enough to be reliably distinguished from the background noise. GNSS signals are transmitted from satellites at varying power levels depending on the code and frequency used. However, their power gradually attenuates as these signals travel through the atmosphere and encounter various propagation effects, such as absorption, scattering, and diffraction. When they reach the GNSS receiver on Earth, the signal amplitudes are often close to below the noise floor, making them more challenging to detect and track accurately. Amplitude is particularly significant in this context because it directly influences the signal's power, with power being proportional to the square of the amplitude ($P \propto A^2$). The absolute minimum power level at which a GNSS signal can still be distinguished from background noise is approximately −204 dBW/Hz. Under typical conditions, however, the C/A-code signal is expected to reach the receiver with a minimum power of approximately -160 dBW (Arinc Research Corporation, 1993, p. 12; Hartinger & Brunner, 1999, p. 12; Hofmann-Wellenhof et al., 2007, p. 86). When the signal power is at this level, the corresponding C/N_0 is about 44 dB Hz.

Figures 4.6 and 4.7 illustrate the C/N_0 percentages, where blue represents geodetic hardware results and green represents low-cost hardware. Since the study focuses on low-cost hardware, the detailed distribution of low-cost hardware is discussed. Fewer than 1% of observations from low-cost hardware exceed the 50-60 dB Hz C/N₀ range. In contrast, geodetic receivers have approximately 35% of observations within the 50-60 dB Hz range for the first and second frequencies and around 57% for the third frequency. For low-cost hardware, the majority of observations fall within the 40-50 dB Hz range across all frequency bands: 80.3% for the first frequency, 60.9% for the second, and 53.5% for the third, with fewer than 1% of observations exceeding 50 dB Hz.

Given that the majority of observations from low-cost receivers fall within the 40-50 dB Hz C/N_0 range, with fewer than 1% exceeding 50 dB Hz, a new C/N_0-based weighting scheme has been developed to address the unique signal behaviour of low-cost receivers. The proposed C/N_0-based weighting scheme is called the C/N_0-based empirical weighting scheme hereafter. The scheme is as follows:

$$W = \frac{C/N_{0_{max}} - C/N_{0_{min}}}{1+e^{-k(C/N_0 - C/N_{0_{mid}})}} + C/N_{0_{min}} \tag{4-2}$$

where, W is the weight applied to each observation in filtering process. The parameters $C/N_{0_{max}}$ and $C/N_{0_{min}}$ represents the maximum and minimum carrier-to-noise density in the observation data, respectively. For the analysis in Chapter 6, $C/N_{0_{max}}$ was set to 70 dB Hz and $C/N_{0_{min}}$ was taken 0.8 dB Hz regardless of the observation days and period. The reason for choosing the minimum and maximum C/N_0 comes from the analysis done in Subsection 4.2.3, where the minimum C/N_0 density ratios were low, nearly 0 for the second frequency (Figure 4.5). Though the maximum values of C/N_0 range to 50-60 dB Hz (Figure 4.6), 70 was taken to account for extreme cases. C/N_0 is the carrier-to-noise density ratio values from the individual satellites in different frequencies. The parameter k is derived by fitting a function to the residuals obtained after adjustment, controlling the steepness of the transition. While $C/N_{0_{mid}}$

is set to 44 dB Hz, marking the midpoint of the function. Equation (4-2) enables a smooth progression between low and high weights assigned to the C/N$_0$ density ratio, with k ensuring that the weights increase gradually as C/N$_0$ values rise above the midpoint.

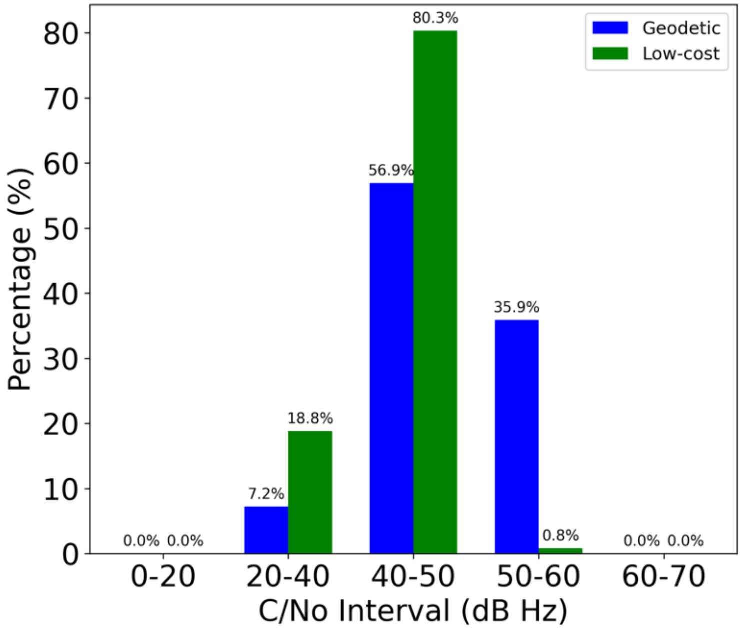

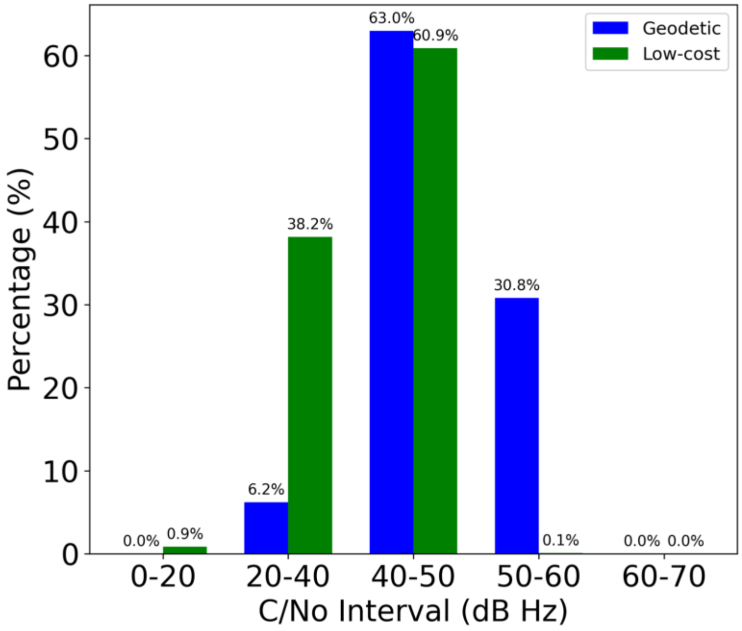

Figure 4.6: Percentages of C/N_0 over different intervals for 5-day datasets for first frequency (top) and second frequency (bottom). Blue colour represents geodetic datasets, and green colour represents low-cost datasets.

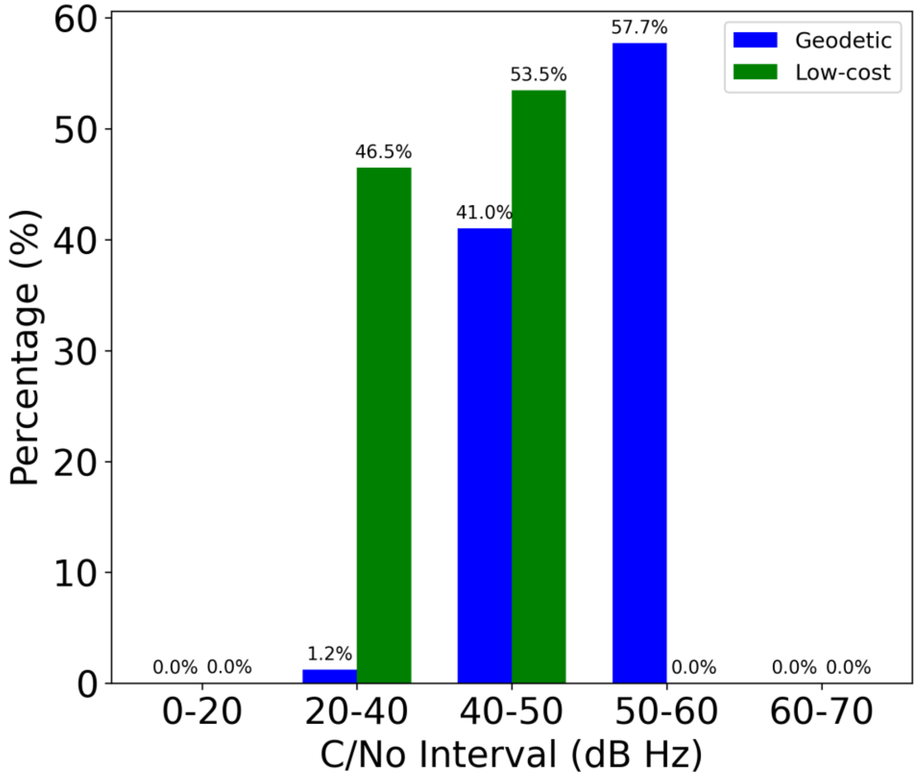

Figure 4.7: Percentages of carrier-to-noise density ratio over different intervals for the 5-day datasets for a third frequency

4.3.1.1 Key component of the C/N_0-based empirical observation weighting function

The function has two parameters: $\mathrm{C/N_{0_{max}}}$ and $\mathrm{C/N_{0_{min}}}$ define the maximum and minimum bounds of the output values for weight (W). The output of the function will vary between these two values, with $\mathrm{C/N_{0_{min}}}$ as the minimum and $\mathrm{C/N_{0_{max}}}$ as the maximum possible out. Basically, the range of the function is $\left[\mathrm{C/N_{0_{min}}}\ ,\ \mathrm{C/N_{0_{max}}}\right]$. The main part of the function is a sigmoid function, as provided below:

$$S = \frac{1}{1 + e^{-k(C/N_0 - C/N_{0_{mid}})}}$$

The exponential function e creates a smooth, S-shaped transition. The function centred around $C/N_{0_{mid}}$, which defines the midpoint of the transition where the output of the sigmoid approaches 0.5. The exponential function allows for non-linear sensitivity to changes in C/N_0 values. Near the midpoint, the weight shifts more dramatically due to the steep slope created by the exponential function. This non-linearity creates a selective response to different C/N_0 prioritizing signals within the 40-50 dB Hz range scaled at 44 dB Hz threshold over others. As a result, the proposed model enhances its ability to discriminate between high-quality and low-quality signals.

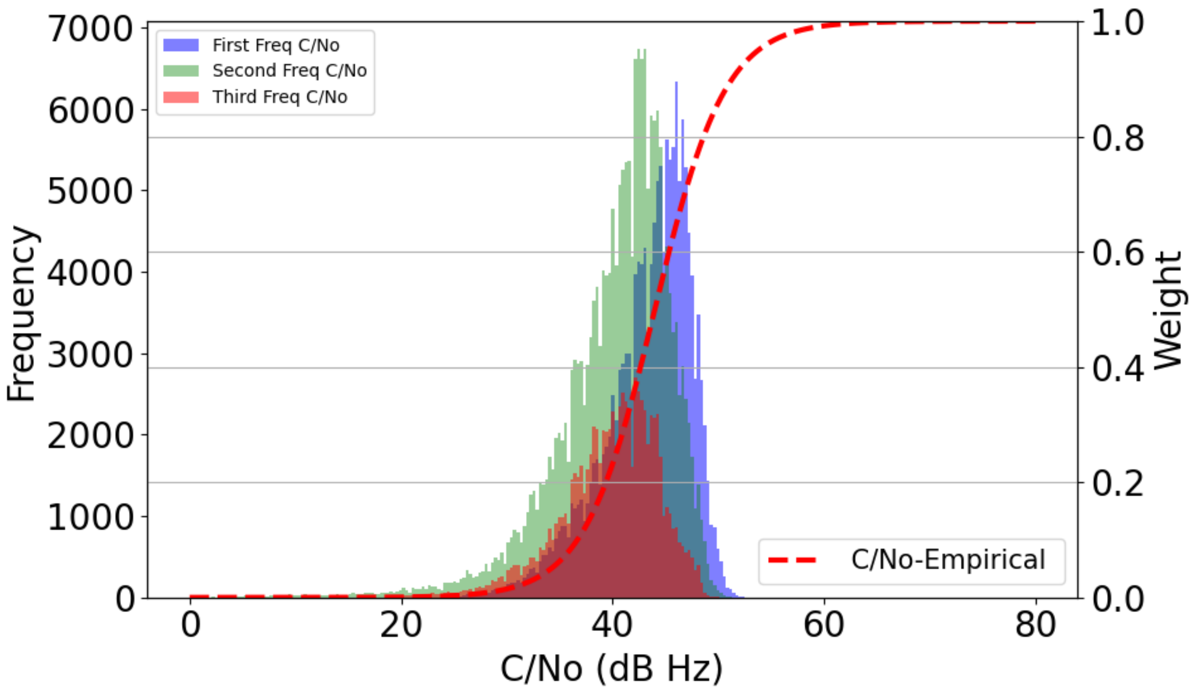

Figure 4.8: Proposed empirical weighting model with first, second and third frequency histogram

The parameter k controls the steepness of the curve. A larger k value makes the transition between low and high weights steeper, while a smaller k value makes it smoother and more gradual. The function is smooth, continuous, and differentiable, which makes the model mathematically stable and predictable. Figure 4.8 provides the visual representation of the proposed model with simulated C/N_0 values ranging from 0 to 80 with 0.05 intervals.

4.3.1.2 Sensitivity of parameters k

Selecting appropriate values for k is critical to the proposed weighting scheme's effectiveness. The parameter k in the weighting function controls the steepness of the transition around the midpoint C/No_{mid}. A higher k value results in a steeper transition, making the weighting function more sensitive to changes in C/N_0 around the midpoint. Conversely, a lower k value results in a more gradual transition, allowing smoother weight variation across a broader range of C/N_0 values. Balancing these trade-offs is essential for achieving optimal performance. Figure 4.9 demonstrates the impact of different values of the parameter k on the normalized weighting function which adjust the observation weighting based on the C/N_0 in dB Hz. The three curves in the plot correspond to different values of the parameter k with 0.1, 0.2, and 0.3.

For k = 0.1, the curve shows a gradual transition, where weights increase slowly with rising C/N_0, meaning even lower C/N_0 signals receive moderate weights. This approach is more inclusive of the lower C/N_0 density ratio. At k = 0.2, the transition is moderately steep, assigning low weights to weak signals and quickly increasing weights as C/N_0 approaches the midpoint (around 44 dB Hz). Lastly, k = 0.3 represents the steepest curve, with low C/N_0 values receiving minimal weight and only signals above 44 dB Hz contributing significantly.

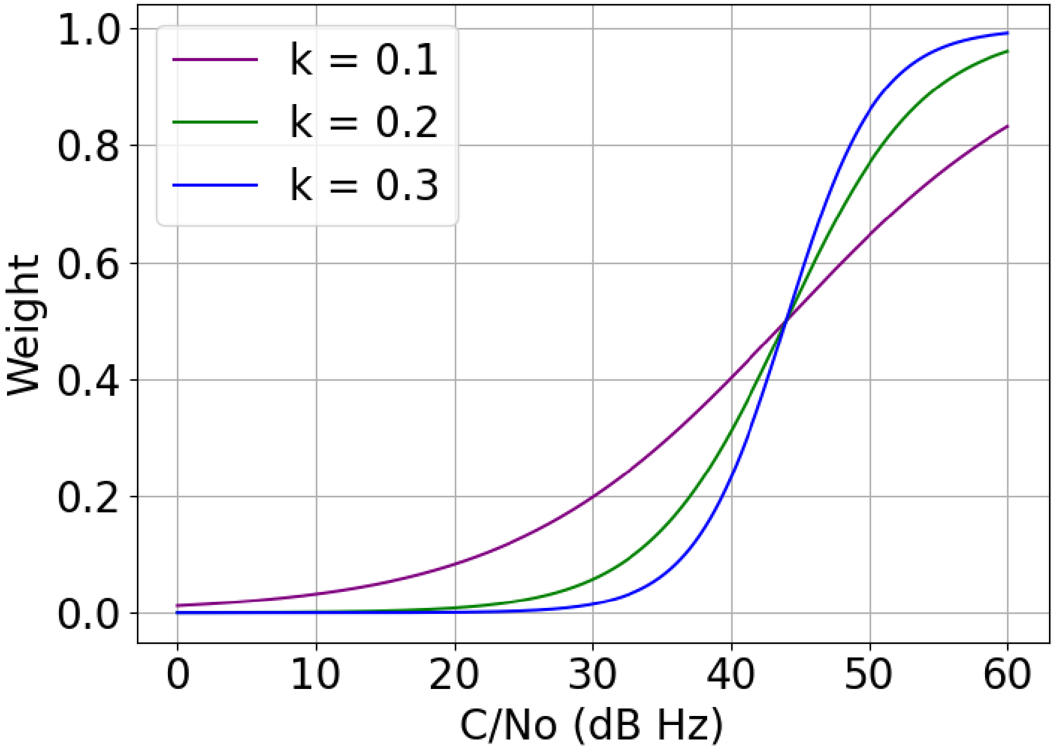

Figure 4.9: Sensitivity evaluation for parameter k on the weighting function

4.3.2 Fitted weighting function

The empirical C/N$_0$-based function is fitted using pseudorange and carrier-phase post-fit least squares residuals for each frequency. This fitting approach, based on Hu et al. (2024), has been adapted and extended in this study to develop the proposed model. The process involves binning the residuals by C/N$_0$, computing the median and two standard deviations (2σ) within each bin to create error bars as shown in Figure 4.9. The (2σ) residuals represent the variability of the binned residuals and are used to define the range of error bars $(median \pm 2\sigma)$. The residuals are then used to fit the proposed weighting function by minimizing the discrepancy between the residuals and the model. The blue error bars represent the binned residual $(median \pm 2\sigma)$

against the C/N$_0$ density ratio. Fitting the proposed function to the least squares post-fit residuals quantify how well the measurements fit the underlying model, leading to a better understanding of how the proposed model captures the noise behaviour from the measurements.

Figure 4.10 suggests that as C/N$_0$ values increase, the median converges towards zero and has a lower residual variability. The empirical C/N$_0$ model (red line) follows a declining trend, matching the decrease in residuals as the signal strength increases. For the carrier-phase residual fit, the function used for fitting appears to capture the trend quite accurately. Since the residuals of carrier-phase measurements do not show a strong trend of increasing or decreasing with C/N$_0$, the fitted red line remains almost flat. Although the model captures the overall trend of pseudorange residuals, it exhibits more consistency at higher C/N$_0$ values. The fitting coefficients for each case are provided in Table 4.2, where "P" denotes pseudorange residuals, and "L" denotes carrier-phase residuals, with subscripts 1, 2, and 3 representing respective frequencies. The fitting coefficients are used later in the model.

Table 4.2: Fitting coefficient used for fitting the empirical C/N$_0$-based model with the residuals

Residual	$\mathrm{C/No_{mid}}$	k
P1	36.7	0.3
P2	39.4	0.2
P3	23.0	0.1
L1	41.0	2.9
L2	46.9	2.2
L3	42.0	2.9

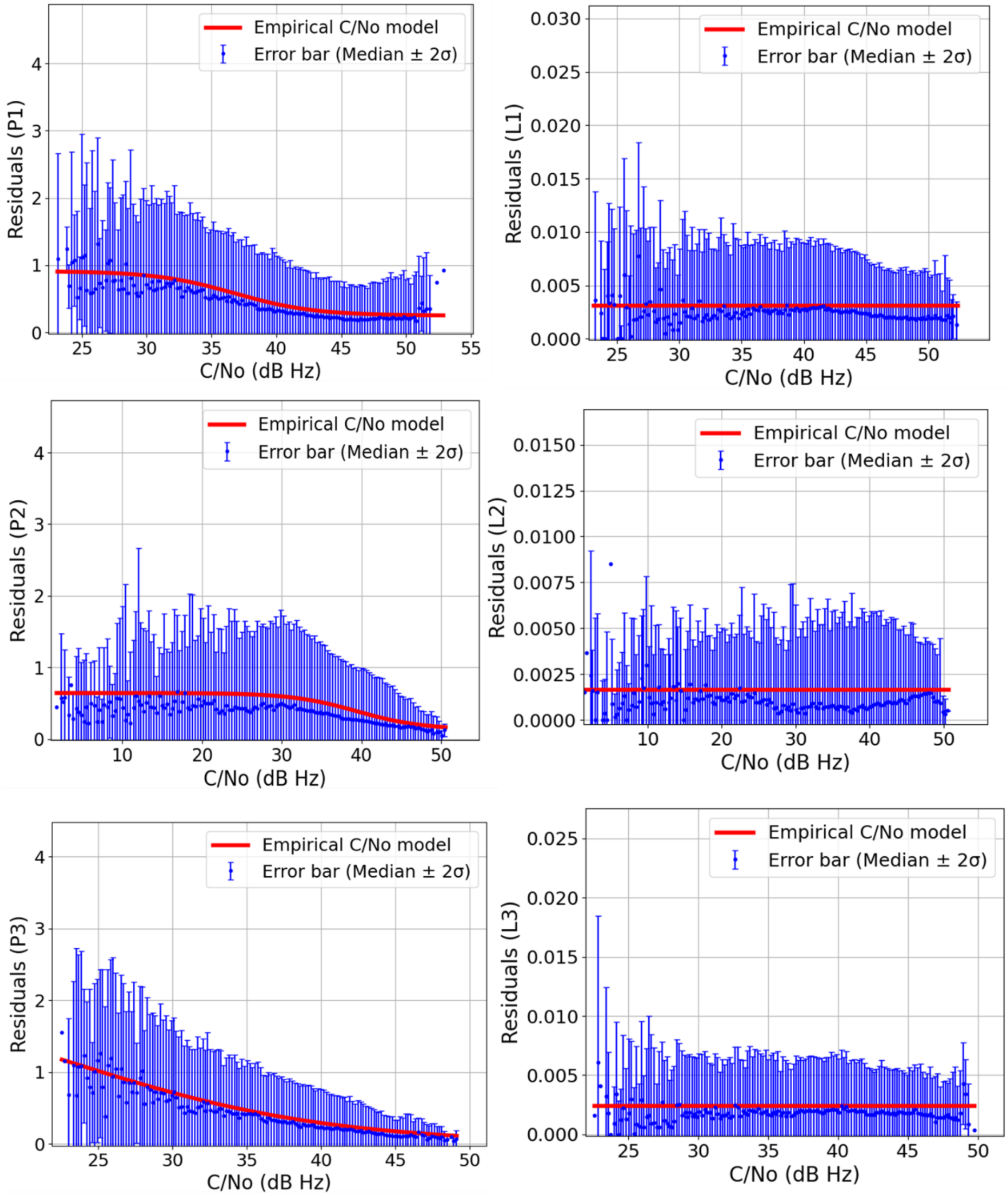

Figure 4.10: Fitting function and residual error bars for the pseudorange (left), carrier-phase (right) with first frequency (top), second frequency (middle) and third frequency (bottom)

4.3.3 Observation weighting scheme comparison

This section compares the proposed model with an existing elevation-based model (Collins & Langley, 1999; Naciri & Bisnath, 2023) and the C/N$_0$-based analytical model (Brunner et al., 1999; Hartinger & Brunner, 1999).

4.3.3.1 Elevation-based scheme and C/N$_0$-based empirical scheme

The elevation-based stochastic model leverages the cosecant function, akin to the tropospheric mapping function (TMF), to describe the relationship between atmospheric delay and the satellite elevation angle. This model assigns higher weights to signals from satellites at higher elevations. The standard deviation of the observations is modelled as:

$$\sigma_{ele} = \frac{\sigma_{90}}{a + b \sin el} \tag{4-3}$$

where:

- σ_{90} is the standard deviation at the zenith (90^0 elevation), set to 0.1 m for pseudorange measurements and 0.001 m for carrier-phase measurements (Naciri & Bisnath, 2023).
- a and b are empirically determined constants, set to 0.15 and 0.85, respectively.
- $sin(el)$ is the sine of the satellite elevation angle.

Figure 4.11 illustrates the variance model associated with the elevation-based weighting scheme, showing how the variance decreases inversely with satellite elevation angle, resulting in higher weights for signals from satellites at higher elevation. As the elevation angle increases, the variance decreases, leading to smaller cofactors and higher weights for observations at higher elevations. This model is particularly effective in open-sky conditions where elevation can be a reliable predictor of signal quality. Analyzing Figure 4.5 shows that the low-cost hardware's C/N$_0$ values stabilize to a 44 dB Hz threshold as the elevation angle increases beyond

40^0. This observation justifies using a 40^0 threshold to determine the reliability of GNSS observations in low-cost receivers. However, the elevation-based model has limitations, as it fails to account for cases where C/N$_0$ remains low even at high elevation angles. Thus, relying solely on elevation for weighting may not fully capture the variations in such environments.

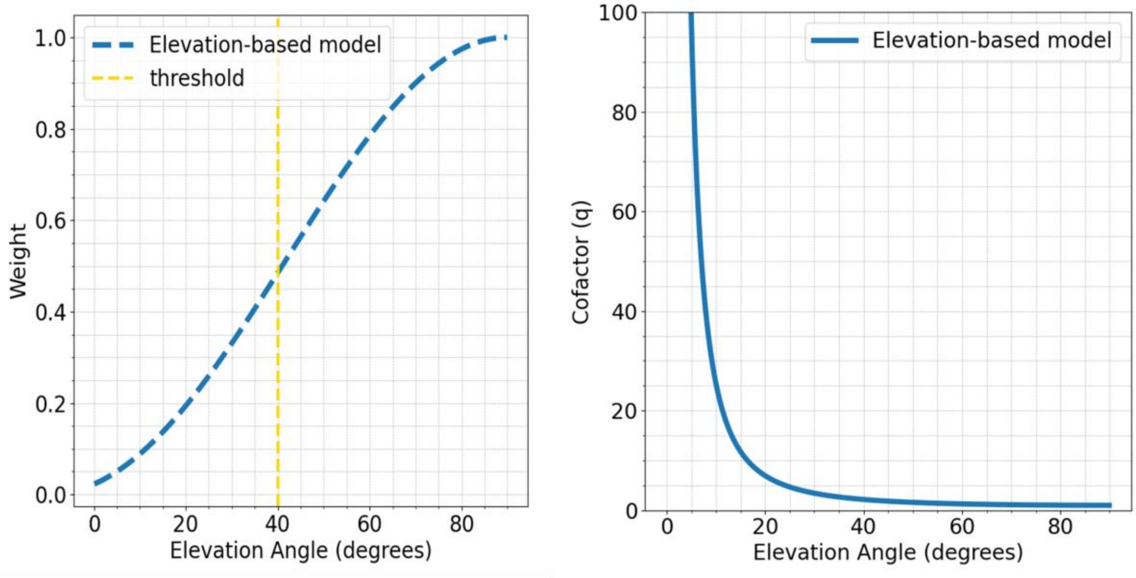

Figure 4.11: Weight and cofactor values calculated using an elevation-based model

4.3.3.2 C/N$_0$-based analytical scheme and C/N$_0$-based empirical scheme

The C/N$_0$-based analytical stochastic model assigns weights based on the C/N$_0$ values from the receiver in RINEX format. A higher C/N$_0$ indicates a stronger signal with less noise, thus deserving a higher weight in the estimation process. The standard deviation is defined by:

$$\sigma_{C/No} = a + b * 10^{-0.5\left(\frac{C/No}{10}\right)} \tag{4-4}$$

where:

- a and b are constants determined empirically through the fitting process to match the observed residuals from least squares post-fit analysis.
- C/N_0 is the carrier-to-noise density ratio in dB Hz

This equation models the standard deviation inversely with the C/N_0 value; as the signal quality improves (higher C/N_0), the variance decreases, increasing the observation's weight.

Figure 4.12 illustrates a comparative analysis of two models: an empirical C/N_0-based model (proposed), an analytical C/N_0-based model, and a histogram representing the C/N_0 distribution for three GNSS frequencies. In the empirical model (shown by the red dashed line), weights increase rapidly as C/N_0 values approach the 30-50 dB Hz range, emphasizing measurements within this range. This approach aligns well with the C/N_0 distribution in low-cost hardware, where approximately 80% of the data falls between 40-50 dB Hz. In contrast, the analytical model (blue dashed line) applies a more gradual increase in weights across the C/N_0 spectrum, resulting in a smoother transition as C/N_0 rises from 30 to 80 dB Hz. This conservative approach assigns relatively high weights only for C/N_0 values above 50 dB Hz, which are rare in low-cost hardware. The empirical C/N_0-based model, with its sharper transition in the mid-range (30-50 dB Hz), provides weights more suited to the actual C/N_0 distribution observed in low-cost hardware. This model's responsiveness to moderate changes in signal quality is advantageous in environments with variable interference or multipath effects, as it better accommodates fluctuations in signal strength.

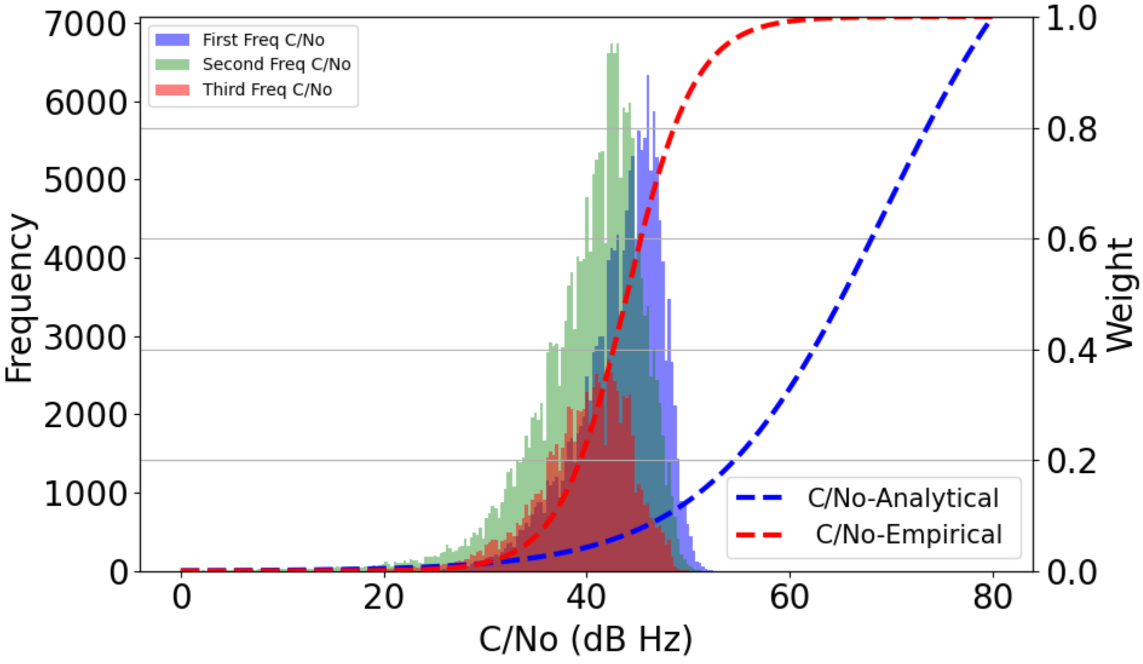

Figure 4.12: C/N_0-based empirical and analytical model comparison with first, second and third frequency histograms

4.4 Summary

This section highlights the necessary adjustments to GNSS data processing for improving positioning accuracy with low-cost hardware. Key modifications were made to the YorkPPP GNSS processing engine. These customizations included integrating additional observation types, setting specific thresholds for filtering unreliable measurements, and implementing an empirical C/N_0-based weighting scheme. This scheme addresses the limitations of traditional elevation-based and equal-weight models, providing a more accurate approach to managing measurement quality variations linked to C/N_0 and elevation angles. Analysis revealed that phase noise increases with wider carrier loop tracking bandwidths, a common feature in low-cost hardware, making C/N_0 a more effective noise indicator than elevation alone, especially at lower elevation angles. Furthermore, the comparison between geodetic and low-cost hardware showed that low-cost devices often fail to meet reliable C/N_0 thresholds at low elevations, underscoring the need for adaptive weighting strategies to enhance their performance. To address these limitations, the new C/N_0-based empirical model was developed, emphasizing signal quality in the 40-50 dB Hz range, which corresponds to most observations from low-cost receivers. The model smoothly adjusts weights using a sigmoid function based on C/N0 values, providing a higher weight increase for signals within this range, aligning better with the actual performance of low-cost hardware. The performance of proposed weighting scheme is further analyzed in Chapter 5.

Chapter 5 Processing improvements of static measurements from low-cost hardware

This chapter explores and compares the three stochastic models discussed in Chapter 4, with two primary focus areas: assessing the performance of the newly proposed C/N_0-based empirical observation weighting model against two established models, an elevation-based model and a C/N_0-based analytical model using data from low-cost GNSS hardware. The second motive is to conduct a detailed evaluation of the C/N_0-based empirical model.

5.1 Data campaign

The experiment for this chapter was conducted on the roof of the LRC building at York University, Toronto, Canada, with the same setup as shown in Figure 5.1. The hardware and the approaches adopted are the same as in Section 3.2, Chapter 3. The hardware and methodologies are consistent with Section 3.2 of Chapter 3. The specific days of data collection are listed in Table 5.1, with data recorded at 30-second intervals. The data were collected in a medium multipath environment.

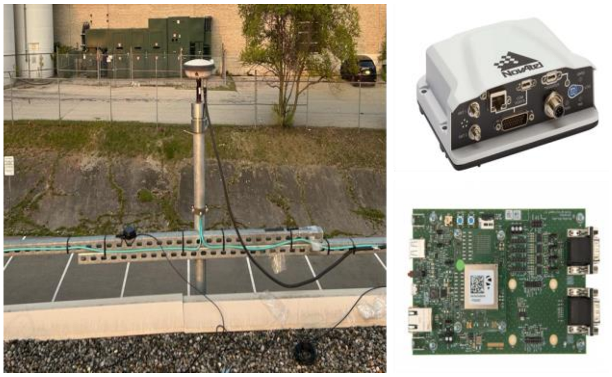

Figure 5.1: Measurement setup with a geodetic and low-cost receiver

Table 5.1: Summary of observation data used for analysis in Sections 5.3 and 5.4

Date	(DOY)	Duration
11th December 2023	344	3 hours
12th December 2023	345	11 hours
13th December 2023	346	12 hours
18th December 2023	352	3 hours
19th December 2023	353	9 hours
20th December 2023	354	5 hours
21st December 2023	355	10 hours
26th December 2023	360	3 hours
30th December 2023	364	11 hours
13th April 2024	104	17 hours
15th April 2024	106	8 hours
16th April 2024	107	5 hours
29th July 2024	211	2 hours
30th July 2024	212	7 hours
Total		106 hours

5.2 PPP processing engine and strategy

The standard PPP processing mathematical model described in Section 2.3.1, already implemented in the in-house YorkPPP engine, was used with the parameters and strategies outlined in Table 5.2. Fourteen days of observation data, detailed in Table 5.1, were used for analysis and assessment. Pre-processing was conducted on the measurements from each satellite. Cycle slips were detected using the geometry-free (GF) combination (Blewitt, 1990) and Melbourne-Wübbena (MW) combination. The ambiguity variance associated with the measurement was reset upon detection of a cycle slip. Satellites with C/N_0 less than 10 dB Hz were excluded to avoid incorporating weak and noisy signals that could reduce positioning accuracy. Satellites with elevation angles below 7.5^0 were removed to minimize atmospheric interference and multipath errors. The choice of satellite elevation rejection mask depends on factors such as application, measurement availability, and hardware used and varies from 5^0 to 25^0 (GNSS, 2016; Wu et al., 2021; Ministry of Natural Resources, Canada, 2024). The selection of a 7.5^0 elevation mask aims to thoroughly evaluate the effectiveness of the proposed C/N_0-based empirical model in processing low-elevation satellite signals.

Ambiguities were resolved with the modified Least-squares AMBiguity Decorrelation Adjustment (MLAMBDA) technique (Chang et al., 2005). The LAMBDA method is a well-established technique in GNSS data processing, recognized for its efficiency in resolving integer ambiguities. Uncombined float ambiguities and their covariances were used as inputs for this method. The ambiguity parameters undergo a transformation process that reduces their correlations, resulting in a simpler and more independent structure for each ambiguity parameter. After transformation, the ambiguities are resolved to their nearest integer values using an advanced search algorithm within the modified LAMBDA framework. All GNSS constellations are processed in this analysis. Satellite clock and orbit products are obtained from GFZ (Deng et al., 2017), while satellite code and phase bias products are from CNES ((Laurichesse & Blot, 2016). For satellite antenna corrections, the IGS20 ANTEX model (Schmid et al., 2016) is applied. The weighting strategy follows the approach outlined in Table

5.2, with an adjustment for BeiDou measurements. These measurements are assigned half the weight of other constellations, as justified by Naciri (2022).

Table 5.2: Processing strategy for the estimated parameters used for observation weighting scheme comparison and assessment

Item	Strategy
Software	YorkPPP engine
Receiver clock	White noise
Orbit and clock	GFZ rapid products
Code and phase bias	CNES products
Satellite antenna correction	IGS20.atx
Adjustment model	Sequential least squares
Processed constellation	GPS/GLONASS/Galileo/BeiDou
Processed frequency	Dual frequency
Epoch interval	30 sec
Elevation cutoff angle	7.5^0
C/N$_0$ cutoff	10 dB Hz
Tropospheric delay	Dry: GMF model and mapping function (Kouba, 2009b)
	Wet: estimated
Ionospheric delays	Estimated as a white noise process
Phase wind-up, relativistic effect	IERS conventions
Ambiguities	Estimated as constants on each continuous arc
Weighting strategies	a) Elevation-based: $\sigma = \frac{\sigma_{90}}{a+b\ sine\ el}$ with σ_{90} is 0.1m and 0.001m for pseudorange and carrier-phase, respectively b) C/N$_0$-analytical: $\sigma_{C/No} = a + b * 10^{-0.5\left(\frac{C/No}{10}\right)}$ with a = 0.1 m and 0.001 m for the pseudorange and carrier-phase measurement. b = 293 c) C/N$_0$-empirical: $W(C/No) = \frac{C/No_{max} - C/No_{min}}{1+e^{-k(C/No - C/No_{mid})}} + C/No_{min}$ where $C/No_{mid} = 44$; $k = 0.3$; $C/N_{0_{max}} = 70$; $C/N_{0_{min}} = 0.8$

5.3 Comparative analysis of GNSS PPP stochastic model with low-cost measurements

This section compares the proposed C/N_0-based empirical model described in Equation (4-2) against the two major weighting schemes: the elevation-based model described in Equation (4-3) and the analytical C/N_0-based model described in Equation (4-4). The comparison metrics used are convergence time and the horizontal and vertical root mean square error (rms) at the 100th, 95th, and 67th percentiles. Solution convergence time and rms are selected as key indicators for the comparative analysis because they offer comprehensive insights into the speed and accuracy of the positioning. A shorter convergence time means the system can provide reliable position estimates more quickly after initialization or signal interruptions. RMSE quantifies the average magnitude of the positioning errors, providing a clear metric for comparing the overall performance of different weighting models. The 2.5 and 5 cm accuracy thresholds are taken for the convergence threshold to align with this research's goal. Achieving a horizontal accuracy of 2.5 cm indicates high-precision positioning, suitable for geodetic surveying applications where minimal positional error is paramount. A 5 cm accuracy threshold is often considered acceptable for precision agriculture, construction, autonomous vehicles, robotics, and other industries where slight positional deviations are tolerable but still require high accuracy.

Observation data for the day mentioned in Table 5.1 was processed individually using the in-house YorkPPP engine, following the processing strategy outlined in Table 5.2 with a sample interval of 30 seconds. Horizontal error and convergence time were calculated by comparing each positioning result to the known reference coordinates. After processing each dataset independently, the average convergence time was computed across all runs to represent the overall PPP convergence time to the mentioned horizontal error.

5.3.1 Convergence time to 5 cm horizontal error

Figure 5.2 presents three subplots comparing the average convergence times (in minutes) at the 100th, 95th, and 67th percentiles. Each subplot illustrates the results with the blue float solution and the orange fixed solution. A float solution is a state of the PPP solution that treats carrier-phase ambiguities as real numbers instead of resolving them in an integer cycle. The fixed solution represents the solution where carrier-phase ambiguities are fixed explicitly in each epoch. The float-to-fixed ratio is calculated as shown in Table 5.2 to quantify the difference in convergence times between the float and fixed solutions. The ratio is obtained by dividing the float solution's convergence time by the fixed solution's convergence time.

Comparing float to fixed solution convergence time, the C/N_0-based empirical model performs best, reducing convergence time by 71% when moving from float (60 minutes) to fixed (17 minutes) in the 100th percentile. In comparison, the elevation-based model achieves a 51% reduction (from 60 float to 29 minutes fixed), and the C/N_0-based analytical model only reduces convergence time by 32% (from 58 float to 39 minutes fixed). At the 95th percentile, the empirical model again leads with an 84% reduction (39 float to 6 fixed). This is significantly better than the elevation-based model’s 56% improvement (from 39 float to 17 minutes fixed) and the analytical model’s 29% improvement (from 36 float to 25 minutes fixed). At the 67th percentile, the empirical and analytical C/N_0-based models achieved instant convergence in the fixed solution (0 minutes), and the elevation-based model took 1 minute. The highest float-to-fixed ratio is 6.3:1 from the C/N_0-empirical model at the 95th percentile. In contrast, the lowest float-to-fixed ratio is 1.4:1, observed in the C/N_0-analytical model at the 95th percentile.

In achieving a fixed solution to 5 cm horizontal accuracy, the proposed C/N$_0$-empirical model demonstrates significantly faster convergence times than others. Compared to the elevation-based model, it achieves an improvement of 42% at the 100th percentile and 62% at the 95th percentile. When compared to the analytical model, the C/N$_0$-empirical model shows an improvement of 56% at the 100th percentile and 75% at the 95th percentile. At the 67th percentile, the proposed model achieves instantaneous convergence. These results indicate that the proposed C/N$_0$-empirical model is effective in achieving precise positioning quickly, compared to existing models. This rapid convergence in 67th percentile solutions reflects the model's robustness and reliability, which is especially valuable for applications requiring swift, high-accuracy positioning. Meanwhile, the float solution exhibits minimal variation in convergence times across all three models, highlighting that the primary advantage of the C/N$_0$-empirical model lies in enhancing fixed solution accuracy rather than float solutions.

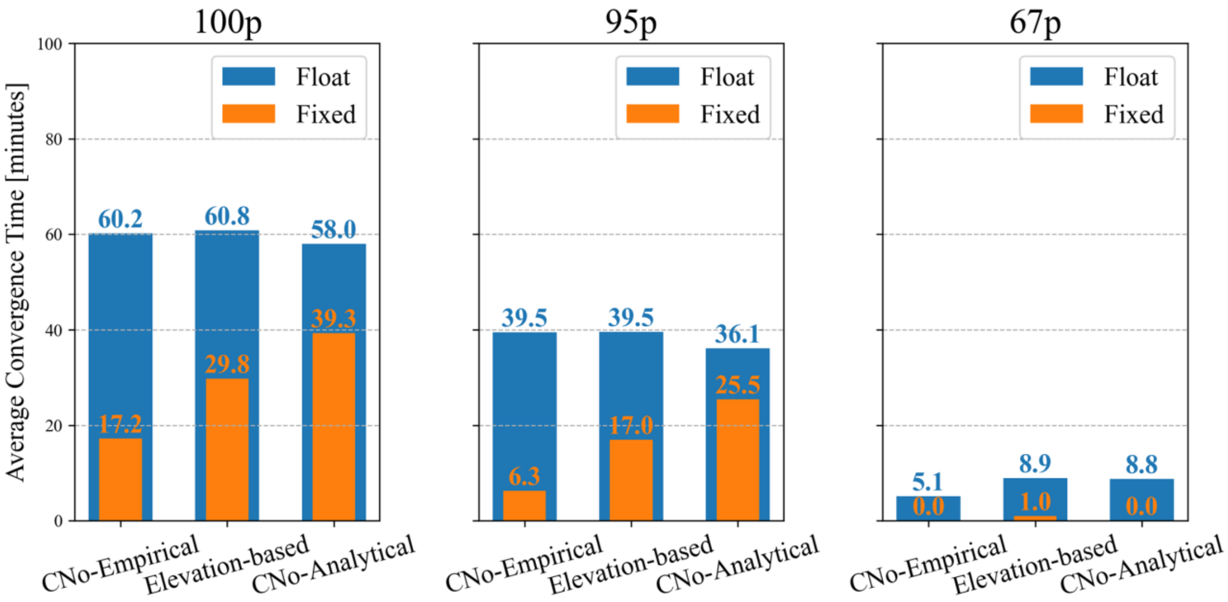

Figure 5.2: Average convergence time to 5 cm horizontal error at 100th, 95th, and 67th percentiles with and without AR

Table 5.3: Average convergence time (minutes) to achieve 5 cm horizontal accuracy

Stochastic model	Percentile	Float [min]	Fixed [min]	Ratio [float: fixed]	Improvement [%]
C/N_0-empirical	100	60.2	**17.2**	**3.5:1**	**71**
Elevation-based	100	60.8	29.8	2.0:1	51
C/N_0-analytical	100	58.0	39.3	1.5:1	32
C/N_0-empirical	95	39.5	**6.3**	**6.3:1**	**84**
Elevation-based	95	39.5	17.01	2.3:1	57
C/N_0-analytical	95	36.1	25.5	1.4:1	29
C/N_0-empirical	67	5.1	0.0	N/A	100
Elevation-based	67	8.9	1.0	8.9:1	88
C/N_0-analytical	67	8.8	0.0	N/A	100

5.3.2 Convergence time to 2.5 cm horizontal error

Out of the 14 days of data listed in Table 5.1, only seven days (50%) reached a 2.5 cm horizontal error threshold. Due to variability in the results, averages were not calculated; instead, data for each day is presented individually in bar plots and tables. Figure 5.3 (DOY 107, 2024), Figure 5.4 (DOY 354, 355, 360, 2023), Figure 5.5 (DOY 364, 2023, DOY 104 and 106, 2024) shows the convergence times in minutes for both float and fixed ambiguity resolution at the 95th and 67th percentiles while Table 5.4 includes results for the 100th, 95th, and 67th percentile. The reasons behind these convergence patterns were further investigated and discussed in Section 5.4. Figures 5.3, 5.4, 5.5 and Table 5.4 show how ambiguity resolution consistently accelerates convergence compared to float solutions across all models and percentiles. This effect is particularly evident in the 67th percentile, where many instances show zero convergence time with PPP-AR. For example, on DOY 360, 2023, at the 67th percentile, the C/N$_0$-based empirical model achieves instantaneous convergence with PPP-AR, whereas convergence was not achievable with float solutions alone. Similarly, on DOY 354, 2023, the C/N$_0$-based empirical model required 41 minutes to converge under PPP; however, fixing ambiguities reduced this time to 0 minutes at the same percentile.

On multiple days, such as DOY 354, 355, and 360 of 2023, the C/N$_0$-based empirical model was the only one to achieve successful convergence in both float and fixed solutions, while the elevation-based and analytical models frequently failed to converge. The C/N$_0$-based empirical model converged with a 41% improvement over the analytical model at the 95th percentile on DOY 360, 2023. Moreover, at the 67th percentile, all the models instantaneously converge to 2.5 cm on DOY 104, 106, 107, 2024 and DOY 364, 2023.

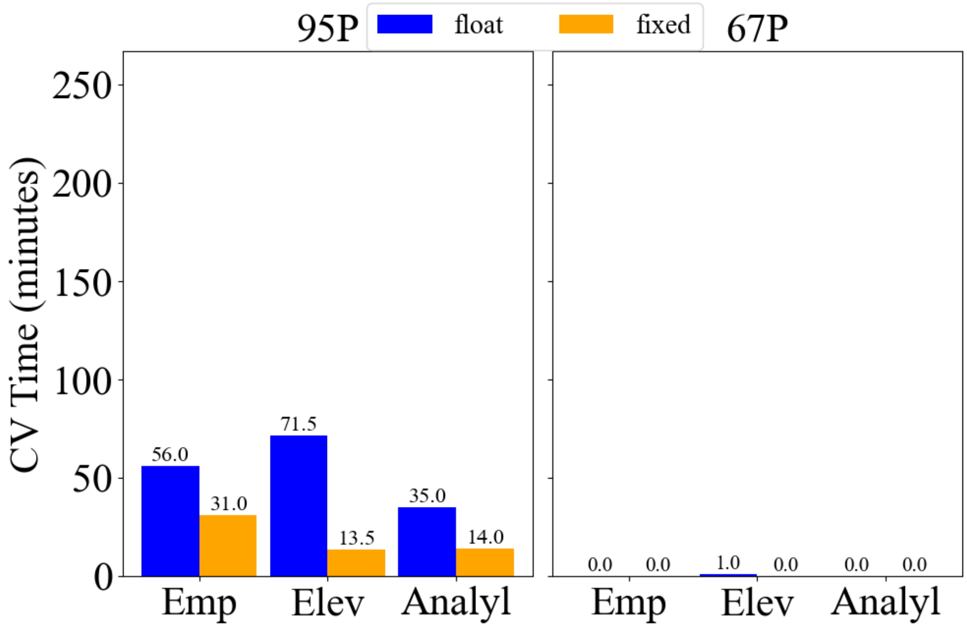

Figure 5.3: Convergence time to achieve 2.5 cm horizontal error at 95th and 67th percentiles, with and without ambiguity resolution (AR) (DOY 354 107, 2023)

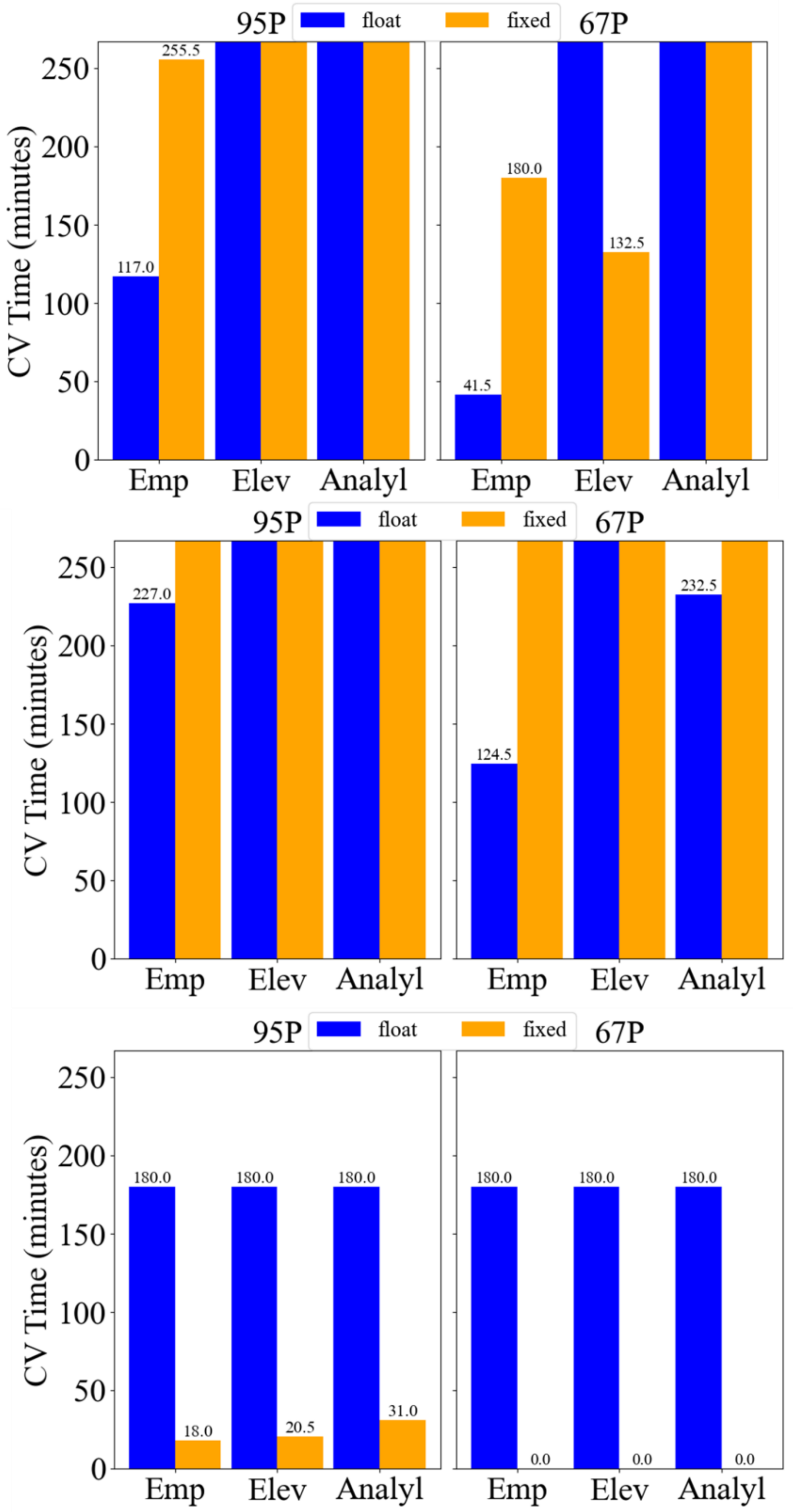

Figure 5.4: Convergence time to achieve 2.5 cm horizontal error at 95th and 67th percentiles, with and without ambiguity resolution (AR). Data are shown for 2023 DOY 354 (top), 355 (middle), 360 (bottom)

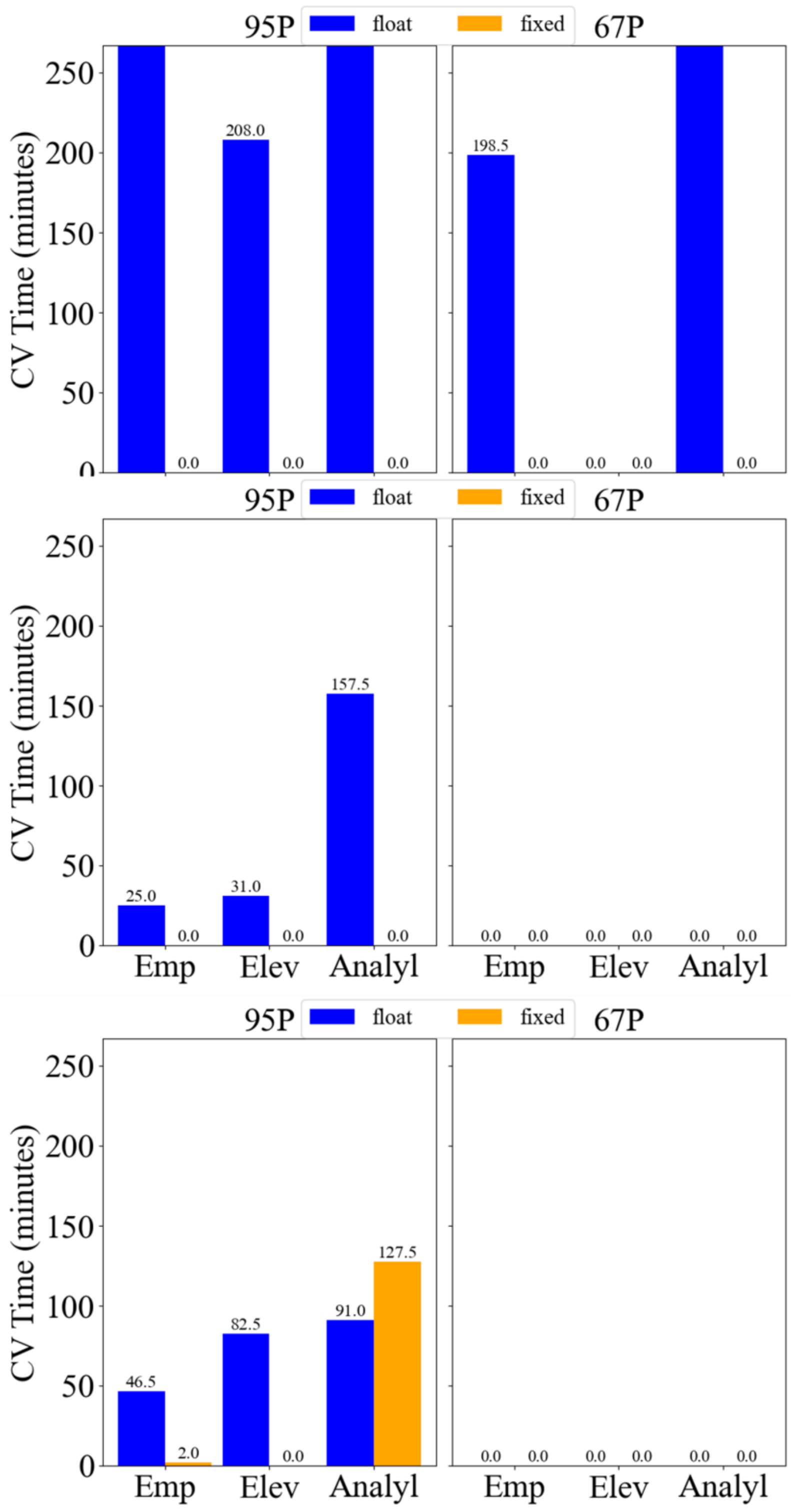

Figure 5.5: Convergence time to achieve 2.5 cm horizontal error at 95th and 67th percentiles, with and without ambiguity resolution (AR). Data are shown for 2023 DOY 364 (top), 2024 DOY 104 (middle), 106 (bottom)

Table 5.4: Average convergence time (minutes) to achieve 2.5 cm horizontal accuracy.

DOY, Year	Float			Fixed		
Percentile	C/N_0-empirical	Elevation-based	C/N_0-analytical	C/N_0-empirical	Elevation-based	C/N_0-analytical
354, 2023						
100	**131**	-	-	**269.5**	-	-
95	**117**	-	-	**255.5**	-	-
67	**41**	-	-	**180**	-	132.5
355, 2023						
100	**245**	-	353.5	-	-	-
95	**227**	-	335	-	-	-
67	**124.5**	-	232.5	-	-	-
360, 2023						
100	-	-	-	**27**	29.5	40
95	-	-	-	**18**	20.5	31
67	-	-	-	0	0	0
364, 2023						
100	418	**241.5**	508.5	141	**12**	14.5
95	384.5	**208**	475	0	0	0
67	198.5	**0**	289	0	0	0
104, 2024						
100	**75**	81.5	208	**9.5**	**9.5**	18.5
95	**25**	31	157	0	0	0
67	0	0	0	0	0	0
106,2024						
100	**69.5**	105.5	114	25	**20**	150.5
95	**46.5**	82.5	91	2	**0**	127.5
67	0	0	0	0	0	0
107,2024						
100	**69**	84.5	48	44	**26.5**	27
95	**56**	71.5	35	31	**13.5**	14
67	0	1	0	0	0	0

5.3.3 Horizontal and vertical root mean squares (rms) error

Horizontal and vertical root mean squares are chosen to provide quantitative insights into the processed data from low-cost hardware observations. The rms plot shows the average magnitude of the errors over time. For instance, lower rms values indicate better precision and higher reliability in the positioning solution. Figure 5.6 demonstrates the comparative analysis of the horizontal and vertical rms errors across three models under the float and fixed solutions.

In the horizontal rms fixed solution, the C/N_0-empirical model consistently shows superior accuracy across all percentiles. At the 100th percentile, there is a 50% (11.5 cm) improvement over the C/N_0-analytical model's rms of 23 cm. The elevation-based model performs comparably, with only a slight difference from the empirical model at this percentile. At the 95th percentile, the empirical model achieves a 2.6 cm rms, improving over the elevation-based model by 13% and outperforming the analytical model by 26%. At the 67th percentile, both the empirical and elevation-based models achieve identical rms values of 2.3 cm, while the analytical model lags slightly with an rms of 2.9 cm, marking a 21% larger error than the empirical model.

For the vertical rms fixed solution, At the 95th percentile, the empirical model's rms improves to 4.6 cm, slightly better than the elevation-based model at 5.1 cm, representing a 9% improvement, while the analytical model trails by 16% at 5.5 cm. At the 67th percentile, the empirical and elevation-based models achieve similar rms values around 2.4 cm, whereas the analytical model remains higher at 2.9 cm, a 21% large error compared to the empirical model.

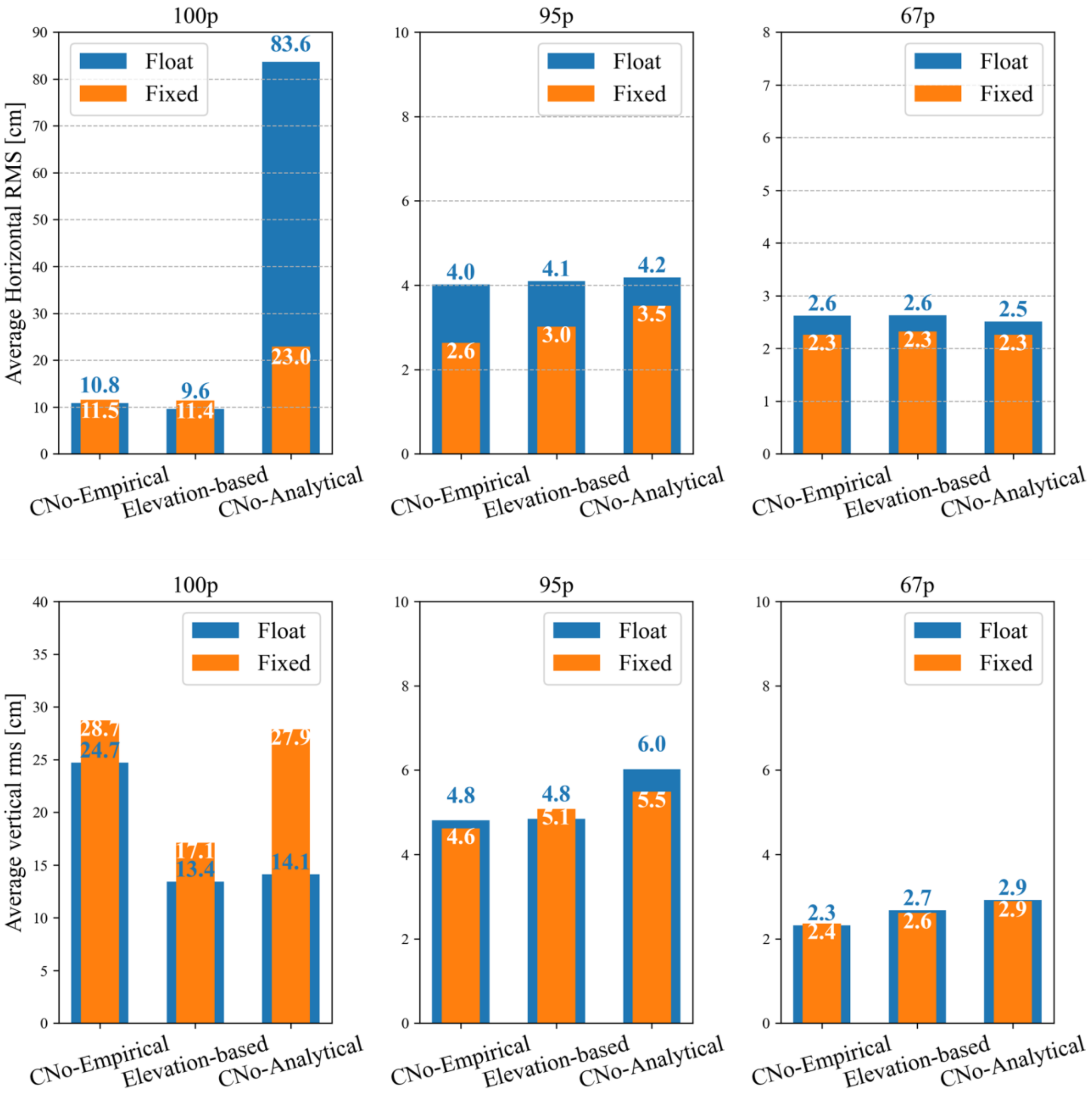

Figure 5.6: Horizontal rms (top) and vertical rms (bottom) with and without AR

5.3.4 Position Dilution of Precision (PDOP)

The geometry between the user and the satellites varies over time due to their relative movement. This geometry is quantified by the dilution of precision (DOP) factor, which reflects satellite positioning quality. DOP is a scalar value that represents the geometrical strength of the satellite configuration observed by a GNSS receiver at a given time. An optimal geometry is indicated by a low DOP value, which is inversely related to the volume of the geometric shape formed by the satellite configuration. The DOP value can be derived from the inverse of the normal equation matrix, specifically:

$$Q = \ (B^T B)^{-1} \tag{5-1}$$

where Q is the cofactor matrix for parameters in an Earth-Centred Earth-Fixed (ECEF) coordinate system (Hofmann-Wellenhof et al., 2007, p. 263). If a weight matrix W is used then,

$$Q = \ (B^T W B)^{-1} \tag{5-2}$$

This cofactor matrix, Q is a 4×4 matrix in which three elements correspond to the site coordinates (U, V, W) and one to the receiver clock bias. The elements of Q can be represented as:

$$Q = \begin{bmatrix} qUU & qUV & qUW & qUt \\ QUV & qVV & qVW & qVt \\ qUW & qVW & qWW & qWt \\ qUt & qVt & qWt & qtt \end{bmatrix} \tag{5-3}$$

This matrix structure Equation (5-3) captures the contributions of both position and clock bias, allowing for the computation of DOP values that reflect the satellite constellation geometry and its influence on positioning accuracy. The diagonal elements of the cofactor matrix Q are used to define various types of DOP values, each representing a different aspect of positioning accuracy:

- Geometric DOP (GDOP): $\sqrt{qUU + qVV + qWW + qtt}$ reflects the effect on both position and time accuracy, providing an overall indication of the geometry's impact on the accuracy of all four parameters (position in three dimensions and time).

- Position DOP (PDOP): $\sqrt{qUU + qVV + qWW}$ pertains to the three-dimensional position accuracy, excluding the time component and represents the effect of geometry on the positional accuracy alone.
- Horizontal DOP (HDOP): $\sqrt{qUU + qVV}$ Relates to the horizontal position accuracy (latitude and longitude).
- Vertical DOP (VDOP): $\sqrt{qVV}$ is concerned with vertical position accuracy (altitude).
- Time DOP (TDOP): $\sqrt{qtt}$ affects the accuracy of time determination.

PDOP ≤ 2 indicates good satellite geometry. Poor satellite geometry, indicated by high DOP values, can significantly affect PPP solutions' accuracy and convergence time. When satellites are clustered in a particular region of the sky, the geometric diversity decreases, leading to amplified positional errors. High PDOP values can lead to larger uncertainties in the estimated positions, making the PPP solution less reliable.

This section compares the PDOP across the three models: C/N_0 empirical, elevation-based, and C/N_0 analytical. Figures 5.7 and 5.8 consist of four panels, each showing the number of processed satellites and the PDOP over different periods for the DOY 354 and 355 of 2023 and DOY 106 and 212 of 2024, respectively. Each panel has two subplots, with the top subplot showing the number of satellites observed and the bottom subplot showing the calculated PDOP. The blue line represents the C/N_0-based empirical model, the orange line represents the elevation-based model, and the green line indicates the C/N_0-based-analytical model.

The C/N_0-based empirical model (blue line) and elevation-based model (orange line) consistently track the highest number of satellites, maintaining around 30-32 satellites throughout the observation periods. In contrast, the C/N_0-based analytical model (green line) tracks the fewest satellites, with values ranging from 15 to 20 satellites. Comparing the PDOP, there are many instances, such as DOY 365 21:30-22:40, DOY 106 10:15 to 11:30 and DOY

212 3:45-5:00, in which the C/N$_0$-based empirical model outperforms both the elevation-based and C/N$_0$-analytical models. These comparative improvements in PDOP using a C/N$_0$-based empirical model are also reflected through the convergence time and positional improvement discussed before.

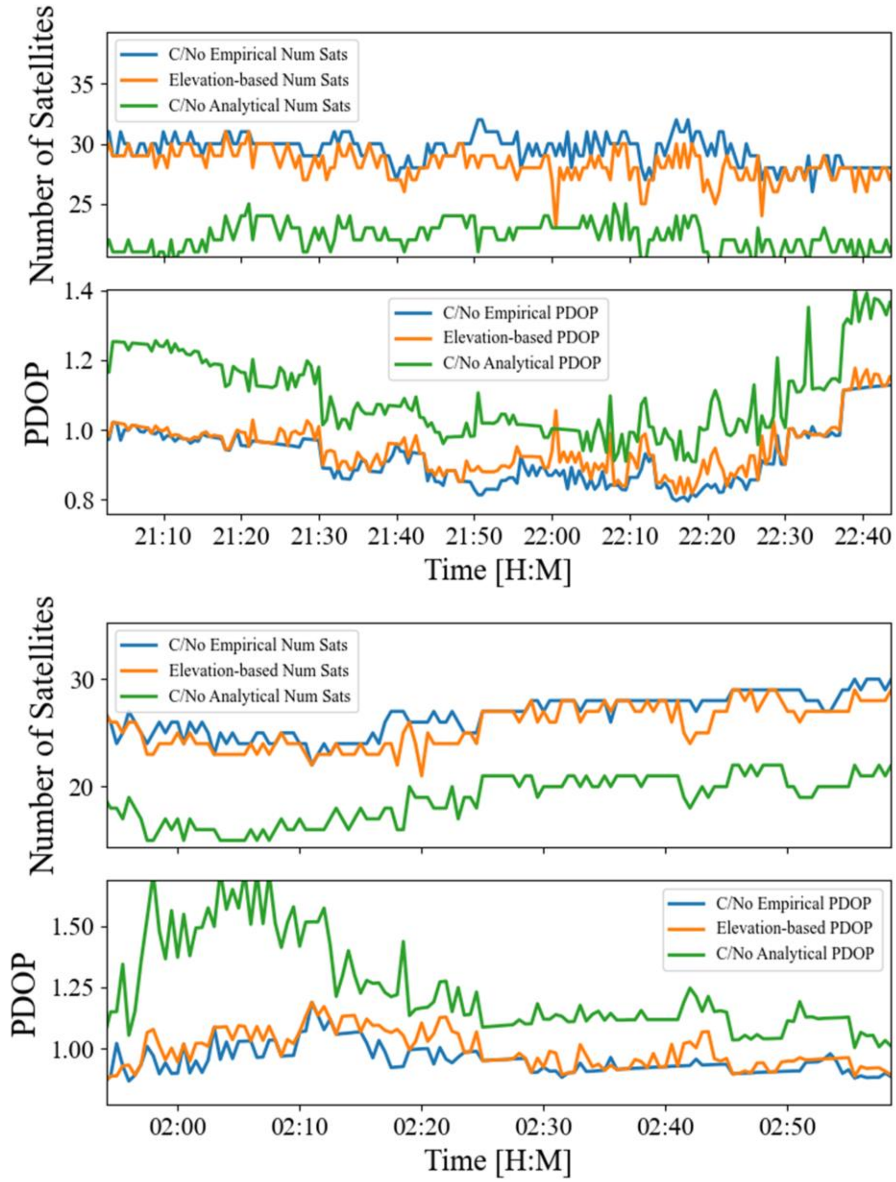

Figure 5.7: Number of satellites and Position Dilution of Precision (PDOP) for DOY 354,2023 (top) and 355, 2023 (bottom)

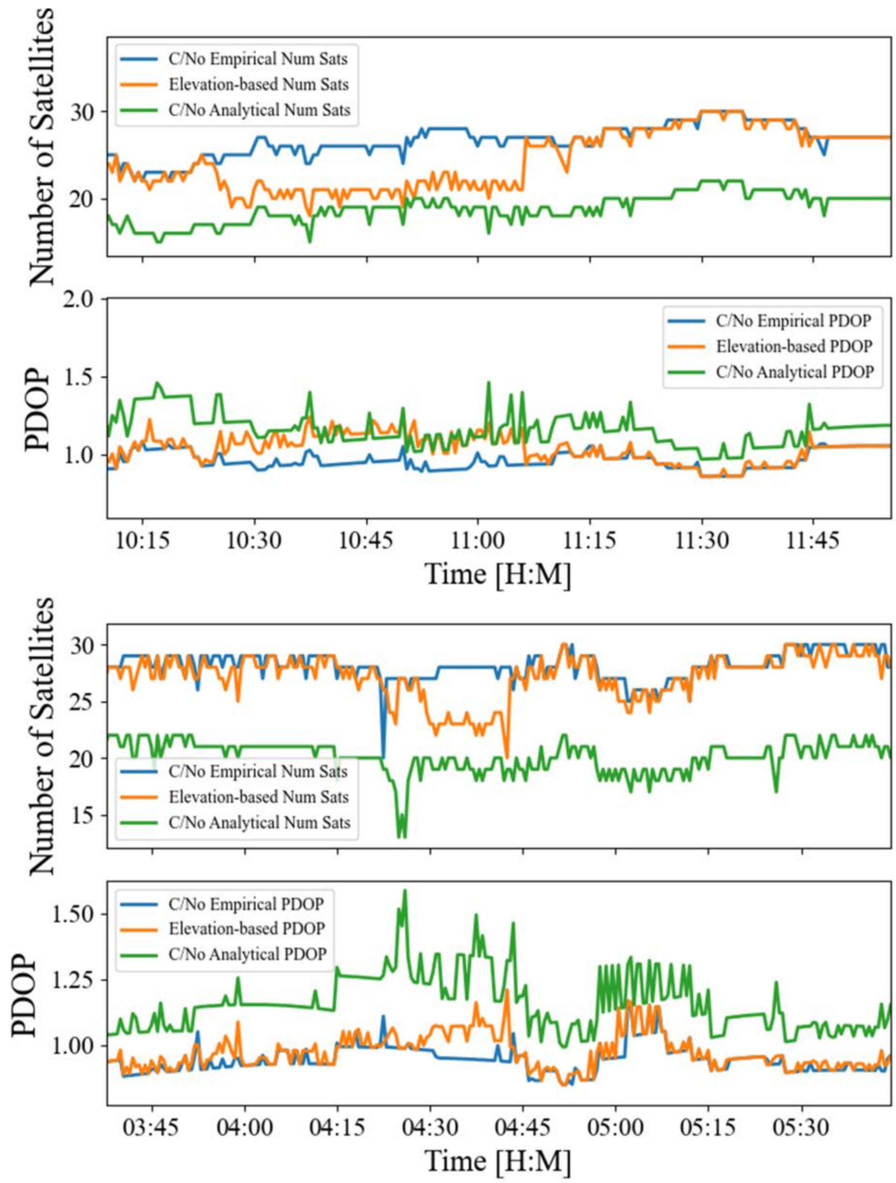

Figure 5.8: Number of satellites and Position Dilution of Precision (PDOP) for DOY 106, 2024 (top) and 212, 2024 (bottom)

5.3.5 A posteriori residual rejection

The a posteriori residual rejection technique is employed to identify and exclude measurements with residuals exceeding predefined thresholds, treating these as outliers to ensure the reliability of the final solution. Once outliers are identified and removed, the sequential least squares filter is iteratively re-applied until all residuals fall within the acceptable range. For the dataset outlined in Table 5.1, three observation weighting schemes are applied independently. Three observation weighting schemes are C/N_0-based empirical, elevation-based, and C/N_0-analytical. The total number of satellites processed is determined by counting the satellites used in each epoch and summing these across all epochs. During pre-processing, satellites that fail quality control checks are excluded. Additionally, satellites identified as outliers due to exceeding the post-fit residual thresholds are separately counted. The percentage of satellites rejected with posterior residual rejection was further analyzed.

The data in Table 5.5 reveals the percentage of satellites rejected due to a posteriori residual rejection for three observation weighting schemes. The results highlight significant differences in satellite rejection rates, indicating the impact of the weighting model on outlier detection and data reliability. The C/N_0-based empirical weighting exhibits the lowest rejection rate (1.8%), and C/N0-based analytical weighting shows the highest rejection rate (7.7%). Given the same residual rejection threshold, pre-processing quality checks, and sequential filter across all three schemes, the differences in rejection rates can be attributed to how each weighting model prioritizes and evaluates measurements during processing. As demonstrated in Section 5.3.1, the C/N_0-based empirical weighting has improved over the other methods in enhancing the overall solution and effectively addressing outliers through appropriate identification and handling.

Table 5.5: Average percentage of satellites rejected due to a posteriori residual rejection

Weighting model	C/N_0-based empirical (%)	Elevation-based (%)	C/N_0-based analytical (%)
Satellite rejection percentage	1.8	3.0	7.7

5.3.6 A posteriori variance of unit weight

The variance of unit weight s a statistical measure used to evaluate the fit of a mathematical model to observed data in least-squares estimation, particularly in GNSS data processing. It quantifies how well the residuals (the differences between observed and modeled values) align with the expected noise levels. Variance of unit weight is defined as:

$$\hat{\sigma}^2 = \frac{\boldsymbol{V^T P v}}{n - u}$$

where v is the vector of residuals, P is the observation weighting, n is the number of observations and u is the number of unknown parameters. $n - u$ is the degree of freedom available for error analysis. If $\hat{\sigma}^2 \approx 1$ then the model fits the data well and the residuals are consistent with the expected noise levels. If $\hat{\sigma}^2 > 1$ then the model does not fully explain the observations, possibly due to overestimated weights (low weighting of observations), poor satellite geometry or unexpected measurement errors, and model errors (e.g., unmodeled tropospheric delays or multipath effects). If $\hat{\sigma}^2 < 1$ then the residuals are smaller than expected, potentially indicating underestimated weights or an overly restrictive model or unrealistic assumptions.

Dataset described in Section 5.1, Table 5.1 is processed with three observation weighting models and further analyzed for the residual. The analysis provides insights into the performance of the weighting models based on the posteriori variance of unit weight. A sample of DOY 344, 2023 is provided in the analysis section as all other observation days has the similar results.

Figure 5.9 provide the comparison of the posteriori variance of unit weight calculated using the residuals obtained using weighting models—C/N$_0$-empirical, elevation-based, and C/N$_0$-

analytical—reveals distinct trends in their performance. The elevation-based model demonstrates the most stable behavior, with variance values consistently clustered between 0.1 and 0.2 and minimal spikes. In contrast, the C/N$_0$-empirical model exhibits the highest sensitivity, with frequent and pronounced spikes reaching up to 0.6. The C/N$_0$-analytical model provides a middle ground, showing slightly higher variance than the elevation-based model in some epochs but fewer spikes compared to the C/N$_0$-empirical model. The C/N$_0$-empirical model, while effective in most epochs, requires refinement to address its sensitivity to dynamic errors and reduce pronounced variance spikes.

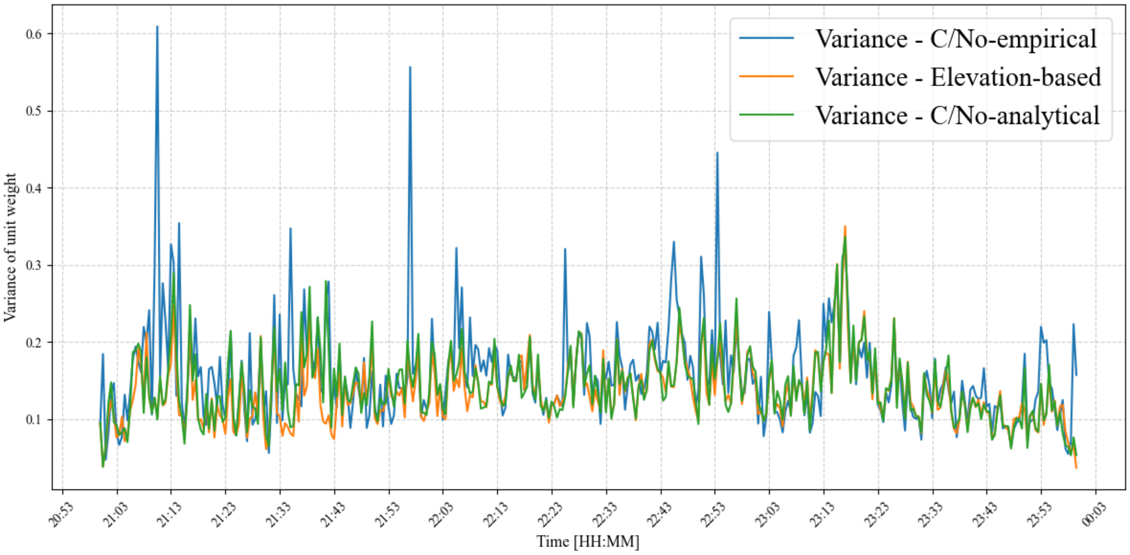

Figure 5.9: Posteriori variance of unit weight over time for three observation weighting models on DOY 344, 2023

5.4 Assessment of the C/N$_0$-based empirical model

The dataset outlined in Table 5.1 was processed using a major stochastic model in conjunction with the newly proposed C/N$_0$-based empirical model. However, the results revealed that seven datasets did not achieve convergence to a horizontal accuracy of 2.5 cm, while the remaining datasets successfully converged. It is important to note that identical pre- and post-processing quality control measures were applied consistently across all datasets, ensuring that the variations in performance were not due to differences in the processing approach. This section delves into an in-depth analysis to explore potential factors that may have influenced the lack of convergence in certain datasets. Specifically, the investigation focuses on the possible correlations between non-converging datasets and residual errors, ambiguity resolution challenges, and number of satellites including PDOP.

The datasets were divided into two groups: those that successfully converged to a horizontal accuracy of 2.5 cm and those that did not to facilitate a more detailed comparison. From each group, the dataset exhibiting the highest horizontal rms was selected for further scrutiny. The two datasets chosen for this comparative analysis are from DOY 344, 2023 (December 11, 2023) and DOY 107, 2024 (April 15, 2024). By isolating these sample datasets, the analysis aims to identify the underlying causes of the differences in convergence behaviour, emphasizing post-fit least squares residuals, ambiguity resolution, and the impact of number of satellites being processed. This comparative approach will shed light on the relationship between the stochastic and empirical models employed, providing insights into potential areas for further refinement of the convergence process.

5.4.1 Positional performance

Positional performance metrics include the overall performance of float and fixed solutions and provide visual representations of convergence time and performance. The dataset from 15th April 2024 serves as a benchmark against which the performance of the 11th Dec 2023 dataset is evaluated, offering insights into convergence behaviour and accuracy improvements achieved through C/N$_0$-based empirical observation weighting model.

The radar plot Figure 5.10 highlights the performance differences between the two datasets across eight key positional metrics. Each axis on the radar plot corresponds to a specific metric, such as float and fixed horizontal and vertical rms, both before and after convergence. The data points for these variables are connected, forming polygons that visually depict the performance. The overlapping polygons enable a direct visual comparison of accuracy and convergence between these dates. The closer a polygon is to the center, the better the performance of lower RMS errors and improved positioning accuracy. The data reveals that the April 15, 2024, dataset consistently achieved better accuracy, as the orange polygon shows tighter bounds across most metrics, especially after convergence. Overall, this radar plot offers quick, visual positioning performance differences between the two datasets.

Figure 5.11 provides the horizontal and vertical rms before and after convergence for the DOY 364, 2023 and DOY 107, 2024. The April 2024 (DOY 107) dataset shows notable improvements in post-convergence accuracy across most metrics. The float horizontal rms is also presented in Table 5.6. The decrease is significant, from 17.8 cm in December (DOY 364) to 13.9 cm in the April datasets, an improvement of approximately 21%. However, the fixed horizontal rms increased from 16.1 cm to 20.1 cm, suggesting that fixed solutions in the April dataset might have experienced more variability before convergence. In terms of vertical accuracy, both float and fixed vertical rms remain similar between the two datasets pre-convergence, with float vertical rms increasing slightly in April (from 17 cm to 20 cm) and fixed vertical rms decreasing marginally (from 22 cm to 21 cm). The post-convergence performance, however, showed substantial improvement in April, where float vertical rms dropped from 6.4

cm to 1 cm, and fixed vertical rms improved from 2.9 cm to 0.9 cm. The statistics are presented in Table 5.6 for further detail.

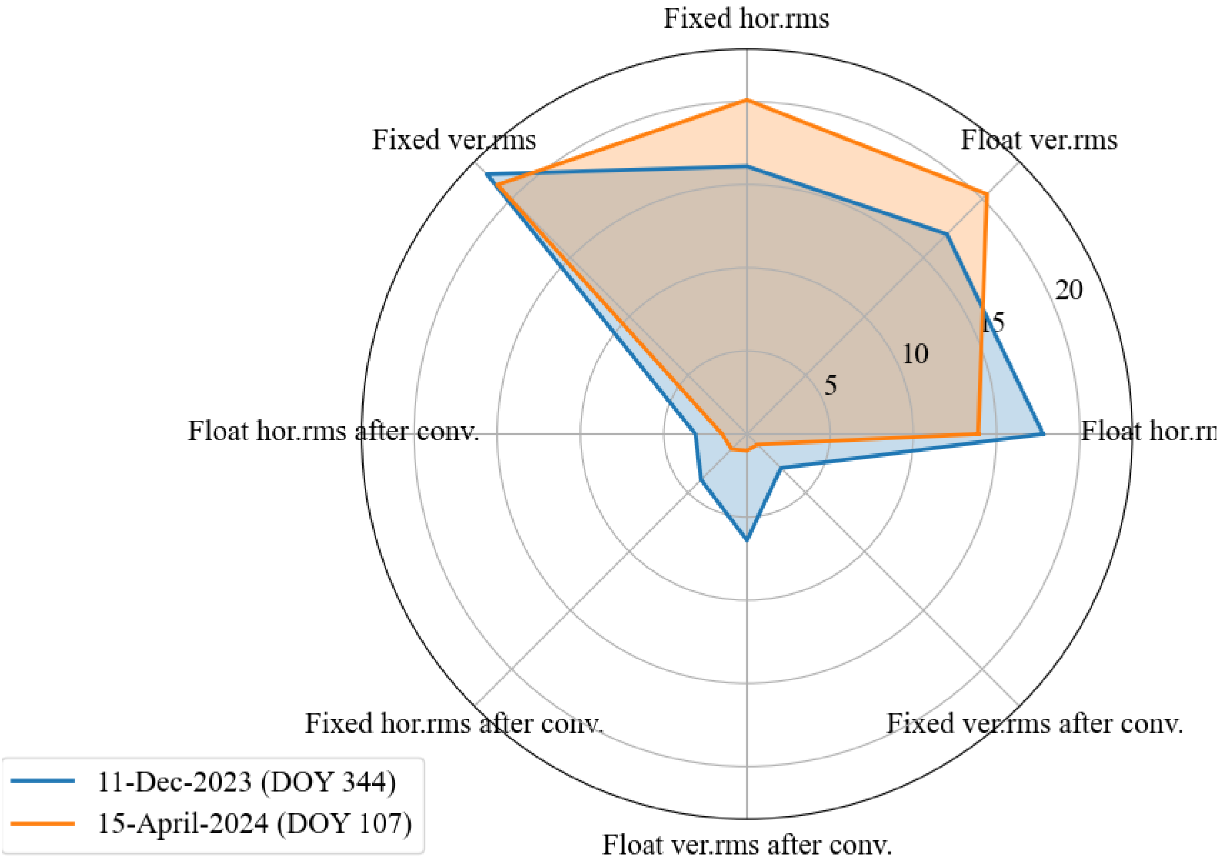

Figure 5.10: Radar plot comparing horizontal and vertical rms for float and fixed solutions, both before and after convergence, on DOY 344, 2023 (December 11, 2023), and DOY 107, 2024 (April 15, 2024) using C/N_0-based empirical weighting observation model

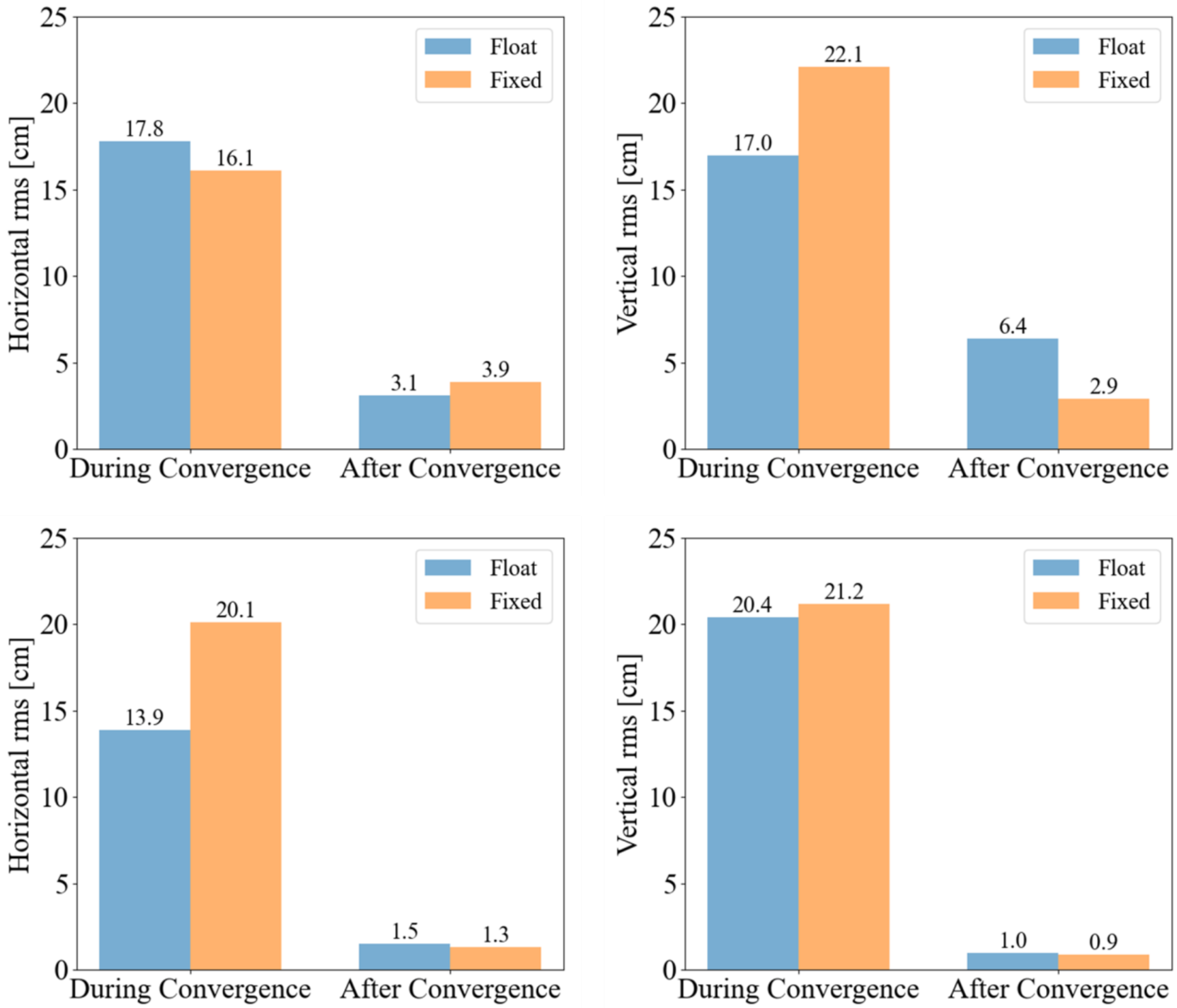

Figure 5.11: Horizontal and vertical rms before and after convergence for DOY 364, 2023 (top), and DOY 107, 2024 (bottom) arranged from left to right, respectively

The horizontal and vertical error plots presented in Figure 5.12 provide a time vs horizontal and vertical error analysis of the float and fixed solutions for DOY 344, 2023 (December 11, 2023) and DOY 107, 2024 (April 15, 2024). These plots illustrate the convergence of horizontal and vertical errors over time, with explicit reference lines marking the 2.5 cm and 5 cm thresholds. Each subplot compares the performance of float and fixed solutions in terms of convergence towards these thresholds. The horizontal error plots for DOY

344, 2023, and DOY 107, 2024 demonstrate significant improvement in the precision of both float and fixed solutions over time, particularly to convergence to the 2.5 cm threshold. In the initial phase, the float and fixed solutions exhibit high horizontal errors, with float solutions showing a slightly higher error than fixed solutions. However, the errors sharply decrease after approximately 22:00 (DOY 344, 2023) and 18:00 (DOY 107, 2024), reflecting convergence. Specifically, during DOY 107, the fixed horizontal solution converged to 2.5 cm within 25 minutes, significantly outperforming the float solution, which required 69 minutes for similar convergence.

There is an interesting instance on DOY 344, 2023, where the horizontal error, between 22:00 and 22:30, converges toward the 2.5 cm threshold but then diverges before reconverging later. This divergence reflects some instability in the solution, which may be attributed to environmental factors, multipath effects, or temporary signal degradation. In contrast, the fixed solution on DOY 107, 2024, consistently converged without divergence, demonstrating a more stable and reliable performance. The fixed solution not only converged faster but also maintained lower post-convergence errors, showing superior reliability and consistency in comparison to the float solution.

For vertical errors, both float and fixed solutions exhibit a similar convergence pattern, but the fixed solutions consistently display better performance. On DOY 107, 2024, for example, the fixed solution converged to 2.5 cm in 73 minutes, while the float solution required 166 minutes, demonstrating the fixed solution's advantage in achieving quicker convergence in vertical positioning. In summary, while both float and fixed solutions show notable improvements in precision and convergence over time, the fixed solution consistently demonstrates faster convergence and better post-convergence accuracy.

Table 5.6: Comparative analysis of horizontal and vertical rms for float and fixed solutions, both before and after convergence, for DOY 344, 2023 (December 11, 2023), and DOY 107, 2024 (April 15, 2024).

Parameters	DOY 344, 2023 (cm)/(min)	DOY 107, 2024 (cm)/(min)
Float horizontal rms	17.8	13.9
Fixed horizontal rms	16.1	20.1
Float vertical rms	17	20.4
Fixed vertical rms	22.1	21.2
Float horizontal rms after convergence	3.1	1.5
Fixed horizontal rms after convergence	3.9	1.3
Float vertical rms after convergence	6.4	1
Fixed vertical rms after convergence	2.9	0.9
Float horizontal error (2.5 cm) convergence	-	69.5
Fixed horizontal error (2.5 cm) convergence	-	25
Float vertical error (2.5 cm) convergence	-	166
Fixed vertical error (2.5 cm) convergence	-	73

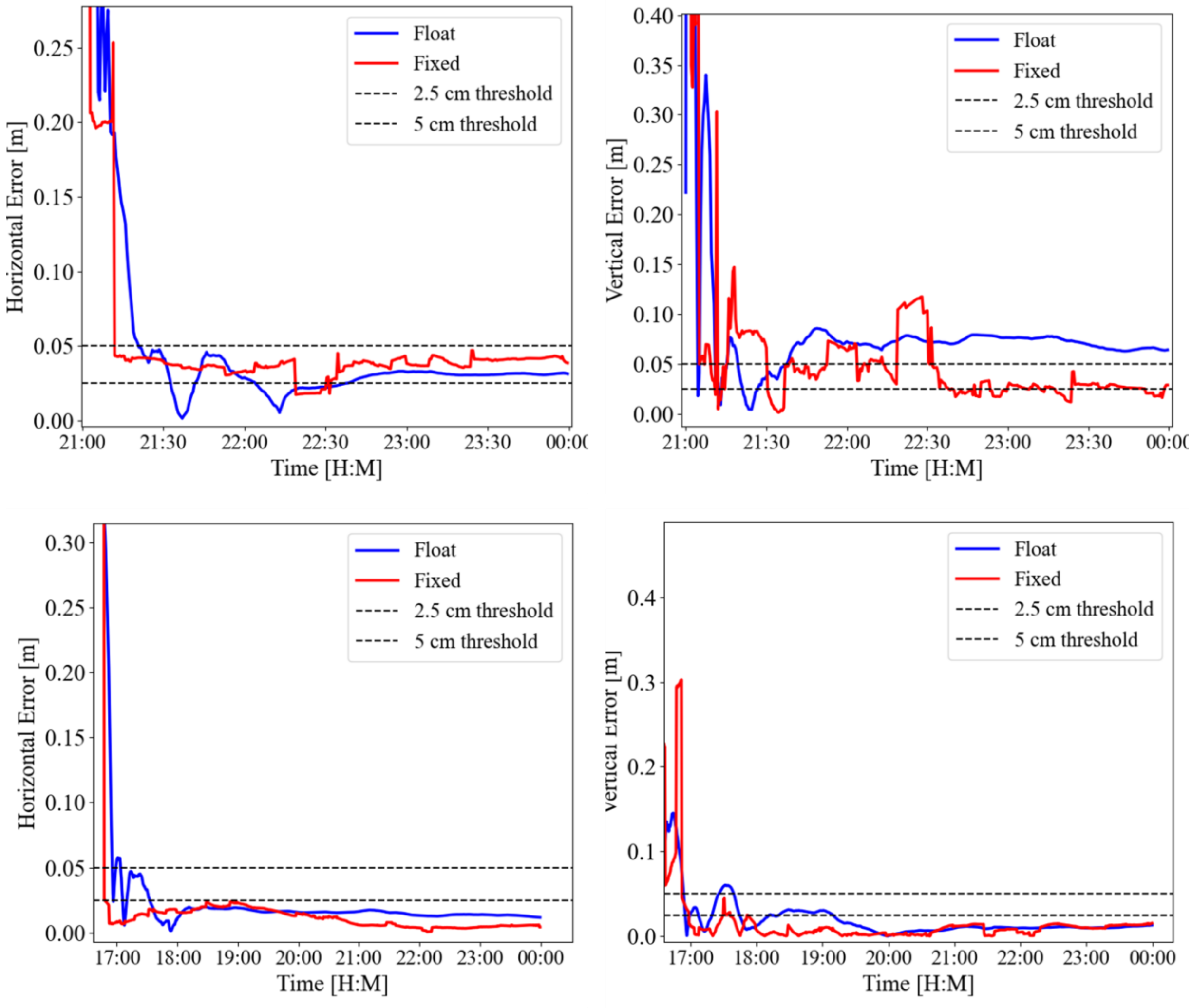

Figure 5.12: Horizontal and vertical error plot with convergence to 5 cm and 2.5 cm for DOY 344, 2023 (top), and DOY 107, 2024 (bottom), arranged from left to right, respectively

5.4.2 Least squares post-fit residuals distribution

Residuals represent the errors or deviations in the model's fit to the data, calculated after the model's parameters have been optimized to minimize the sum of the squared residuals. Ideally, these residuals should be small and exhibit normal distribution without systematic patterns, indicating that the model effectively captures the underlying data structure. Analysis of post-fit residuals provides critical insights into the model's performance. Examining their distribution can detect potential model misspecification, outliers, or unmodeled influences in the data. For instance, if residuals display non-random patterns, such as trends or clustering, this suggests that the model may be inadequate or that key variables are missing. Hence, a rigorous analysis of residual behaviour is necessary. This section analyses the residuals between the two datasets from DOY 344, 2023 (December 11, 2023) and DOY 107, 2024 (April 15, 2024).

Residual analysis is performed by plotting residuals with respect to time to identify temporal patterns, trends, or anomalies in the GNSS measurement data. Residuals over time can help to understand systematic biases, measurement inconsistencies, or variations that may occur during the observation period. By visually inspecting the residuals against time, any deviations from the expected zero-centred distribution can highlight signal unmodeled effects or weaknesses in the processing model. Figure 5.13 compares the post-fit residuals as a function of time for two datasets: DOY 344, 2023 (top row) and DOY 107, 2024 (bottom row). The residuals are shown for pseudorange (postfitP1, postfitP2, postfitP3; blue) and carrier-phase measurements (postfitL1, postfitL2, postfitL3; green) across frequencies 1, 2, and 3. Each panel displays the time series of residuals, with time on the x-axis and residual magnitude on the y-axis.

For pseudorange residuals, both datasets exhibit a consistent spread of ±2.5 m across all frequencies, reflecting stable performance. However, the DOY 107, 2024 dataset shows slightly denser and more uniform clustering of residuals over time compared to DOY 344, 2023. For carrier-phase residuals, the distributions in both datasets remain tightly centered around zero, with a spread limited to ±0.02 m. However, the DOY 107, 2024 dataset shows marginally reduced noise and fewer extreme values compared to DOY 344, 2023. Temporal analysis across both datasets shows no observable trends, biases, or systematic deviations. To further validate and refine the findings, the standardized residual histogram is analyzed, offering a complementary perspective by focusing on the overall distribution of residuals across all measurements.

DOY 344, 2023

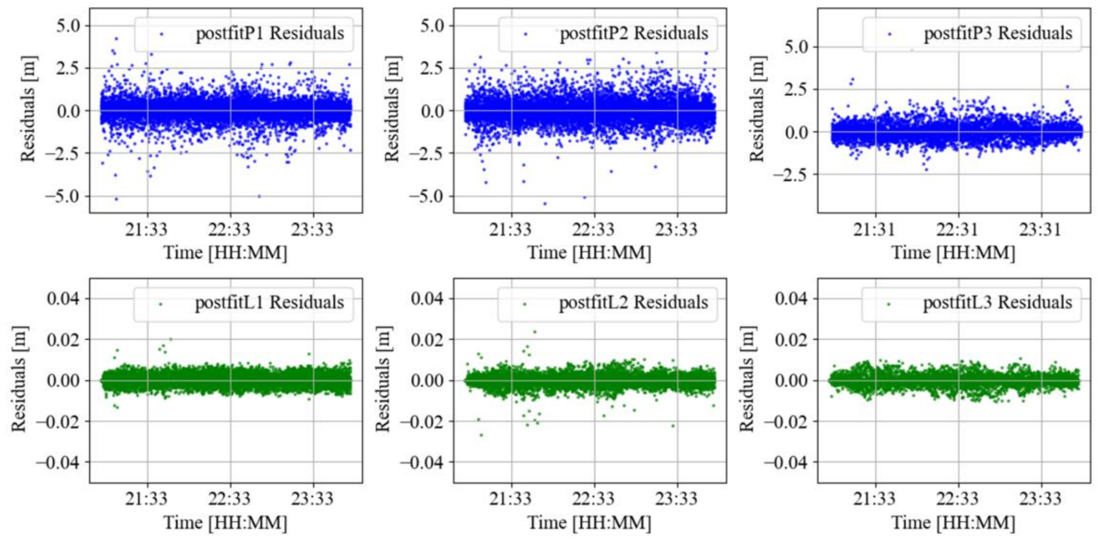

DOY 107, 2024

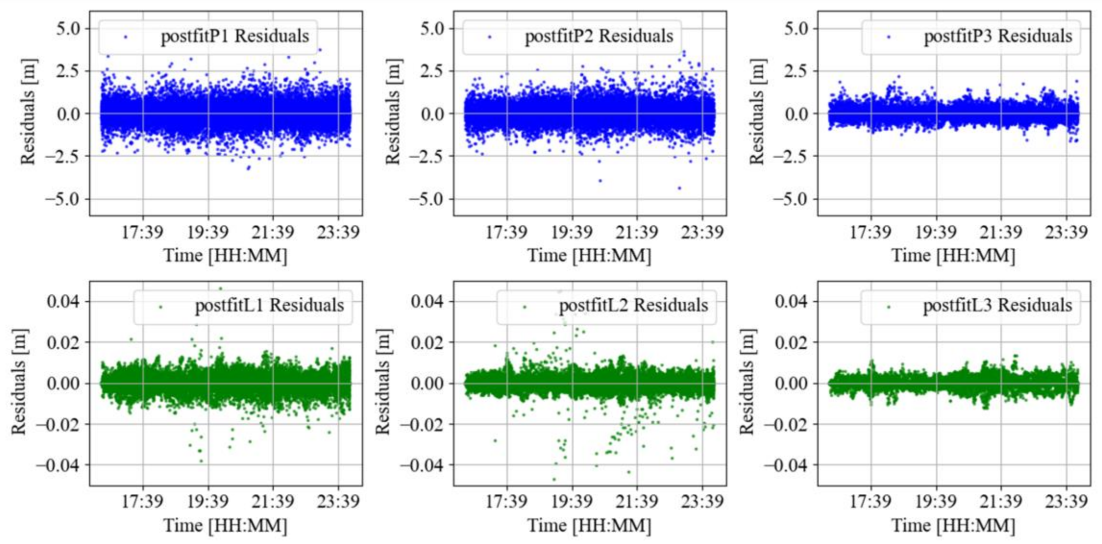

Figure 5.13: Time vs post-fit residuals for DOY 344, 2023 (top row) and DOY 107, 2024 (bottom row), showing pseudorange residuals (postfitP1, postfitP2, postfitP3; blue) and carrier-phase residuals (postfitL1, postfitL2, postfitL3; green) across frequencies 1, 2, and 3, arranged from left to right

Figure 5.14 illustrates histogram distributions of standardized post-fit residuals for both pseudorange and carrier-phase measurements across different frequencies (1, 2, and 3), comparing two datasets: DOY 344, 2023 (top) and DOY 107, 2024 (bottom). The histograms display residuals for pseudoranges (postfitP1, postfitP2, postfitP3) and carrier-phase measurements (postfitL1, postfitL2, postfitL3). All distributions are centred around zero, with the vertical dashed lines indicating the mean (red) and ±1 standard deviation (orange) indicating no systematic biases. Both datasets exhibit symmetric distributions centred at zero.

A comparison between the two datasets shows that the pseudorange residuals in DOY 107, 2024 (converged) exhibit slightly narrower distributions for all frequencies compared to DOY 344, 2023, reflecting a reduction in standard deviations. This is evidence that DOY 107, 2023, converged to a 2.5 cm horizontal error. For carrier-phase measurements, the residuals remain consistently precise across both datasets, with minimal differences in the standard deviation and distribution shape. However, a notable difference is observed in the carrier-phase residuals (bottom row), where the y-axis for the DOY 107, 2024 dataset extends up to 20, particularly at the tails of the distribution. The variability of residuals in the extremes (tails of the histogram) suggests a higher frequency of extreme standardized values in the DOY 107, 2024 data, while the overall high precision of carrier-phase measurements is maintained. To further examine the characteristics of these residual distributions, a Q-Q plot analysis was conducted, providing deeper insights into the behaviour of the data across the two datasets.

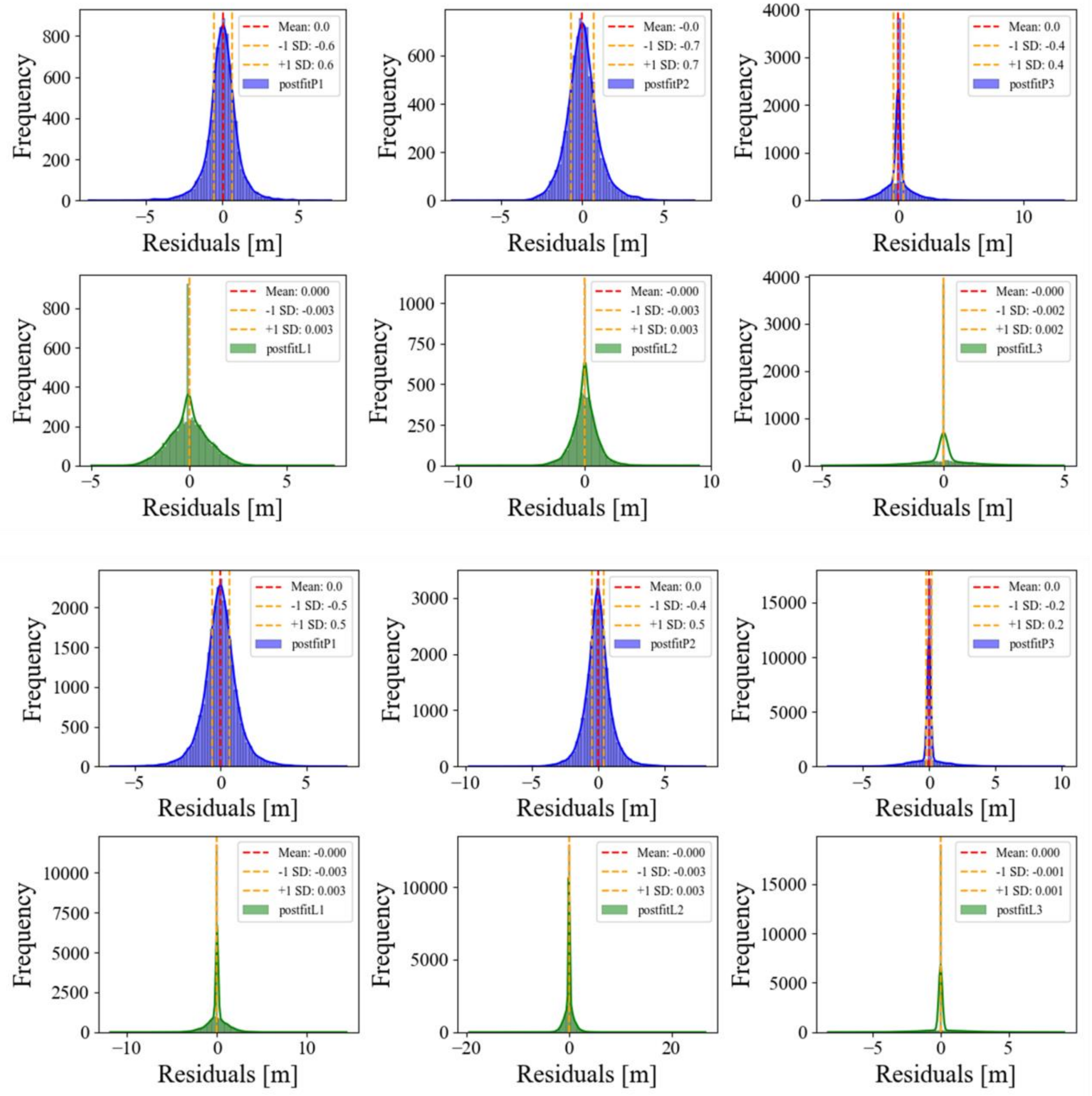

Figure 5.14: Histogram distribution of standardized post-fit residuals for DOY 344, 2023 (top) and DOY 107, 2024 (bottom), showing pseudorange measurements for frequencies 1, 2, and 3, as well as carrier-phase measurements for frequencies 1, 2, and 3, ordered from left to right

A quantile-quantile (Q-Q) plot helps visualize the distribution of a data set to a normal distribution. This plot helps determine if the dataset follows the specified distribution by plotting the data's quantiles against those of the reference distribution. To create a Q-Q plot, the quantiles of the dataset are calculated and then plotted against the expected quantiles from the theoretical distribution. First, the data points are sorted from lowest to highest for the Q-Q plots. The corresponding quantiles from the theoretical distribution are calculated, and each data point is plotted against its corresponding theoretical quantile. If the data follow the theoretical distribution, the points should lie approximately straight. Deviations from the straight line suggest departures from the assumed distribution, such as skewness or kurtosis.

Figure 5.15 provides an analysis of the standardized residuals from six post-fit variables (P1, L1, P2, L2, P3, and L3) over two different days: DOY 107 (blue) and DOY 344 (orange). These variables represent different types of pseudorange residuals (P) and carrier-phase residuals (L) across three different frequencies (1, 2, and 3). The points should fall along the dashed reference line in a perfect normal distribution. Both DOY 107 and DOY 344 exhibit clear deviations from the reference line. The central portion of the plots shows points that align more closely with the reference line, suggesting that the residuals in the middle of the distribution may follow normality more closely than the extremes. The curves in several Q-Q plots (e.g., postfitP1, postfitL2, postfitP3, postfitL3) suggest some skewness, particularly in the DOY 107 (blue) dataset. The blue line deviates more sharply at the extremes, indicating some asymmetry or skew in the residuals. DOY 344 (orange) seems to follow a more moderate pattern but also shows deviations at the extremes, suggesting that both datasets are not perfectly normal but have varying degrees of skewness and kurtosis.

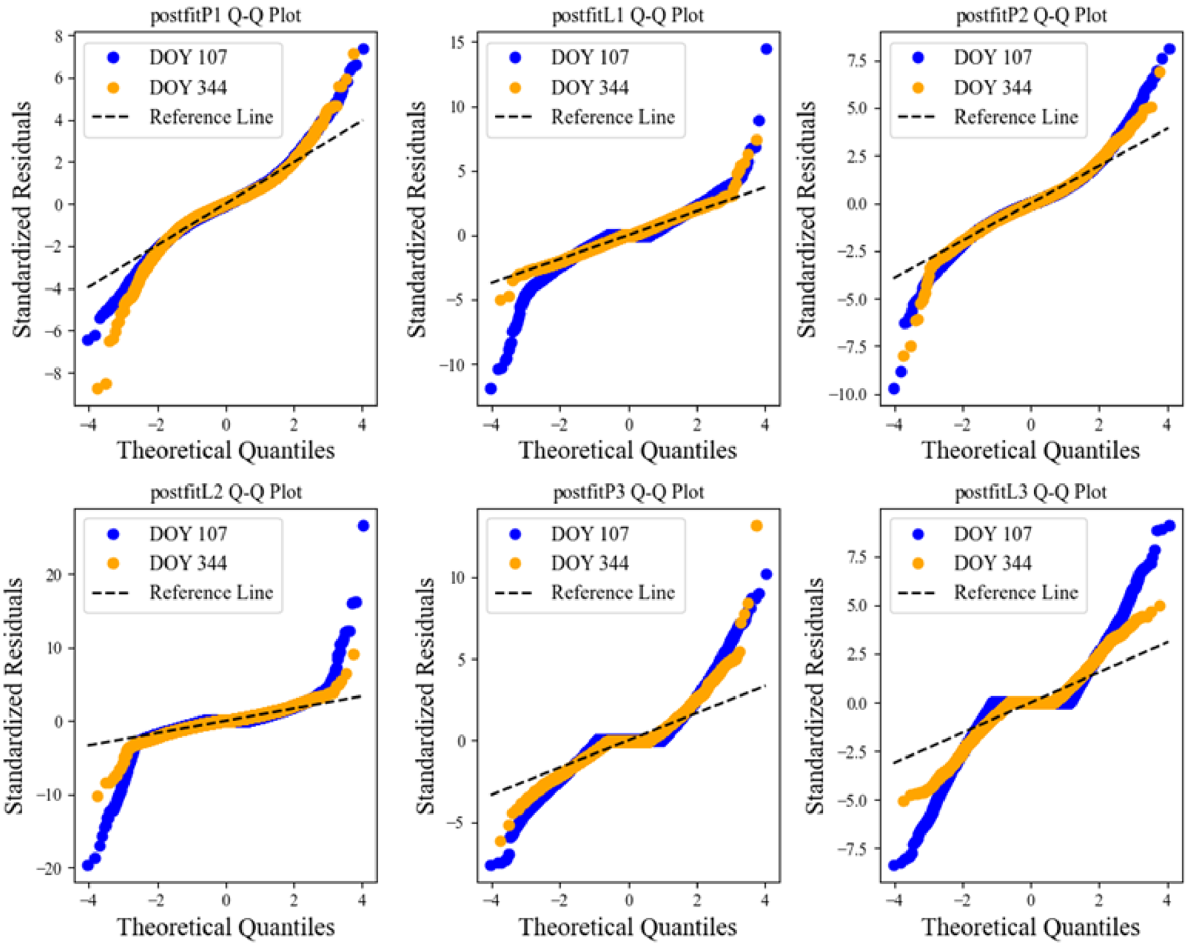

Figure 5.15: Comparison of Q-Q plots of standardized residuals for DOY 107 and DOY 344 across various post-fit parameters

To explore these deviations further, two statistical measures, skewness and kurtosis, can provide deeper insights into the shape of the residuals' distribution. Skewness measures the asymmetry of the distribution of data around its mean. It quantifies how much the data deviates from symmetry. If the skewness is zero, the data are perfectly symmetric. It involves finding the third moment of the distribution relative to the mean and normalizing it by the standard deviation. High kurtosis values, typically greater than 3, indicate the presence of outliers and a heavy-tailed distribution, where more data points reside in the tails compared to a normal distribution. It does not just measure outliers but also the overall shape of the distribution’s tails and peaks. The fourth moment of the distribution is taken to capture the extreme values in the tail. If Leptokurtic Kurtosis > 3, there is a heavy-tailed distribution, meaning more data points are in the tails. This suggests the presence of outliers. If Kurtosis = 3, the distribution is similar to a normal distribution. If Kurtosis < 3, then it indicates the light-tailed distribution, meaning fewer data points in the tails (fewer outliers).

Figure 5.16 provides visual insight into the skewness and kurtosis of the post-fit residuals for different variables (P1, L1, P2, L2, P3, and L3) across two days, DOY 107 (blue) and DOY 344 (orange). Here, P stands for pseudorange residuals, L stands for carrier-phase residuals, and 1, 2, and 3 are respective frequencies. From the comparative analysis, several critical observations can be made. For both DOY 107 and DOY 344, postfitL2 exhibits negative skewness, indicating a preponderance of negative residuals. However, while both days share this trait, DOY 107 also displays significantly high kurtosis for these variables, particularly in postfitL2, where kurtosis exceeds 60. This high kurtosis indicates a large number of extreme outliers, which could typically hinder convergence. Nevertheless, despite these extreme residuals, DOY 107 successfully converged to the 2.5 cm accuracy, suggesting that kurtosis, and hence the presence of outliers, may not be the sole determinant in preventing or achieving convergence. The ability of the residual distribution to remain symmetrical, even with outliers, likely played a more crucial role.

On the other hand, DOY 344 consistently shows lower kurtosis across most variables, indicating fewer extreme residuals. However, DOY 344 did not converge to the desired accuracy. The skewness values reveal the likely cause: several key variables, such as postfitP3, postfitP1, and postfitL3, exhibit positive skewness, which indicates a bias toward larger positive residuals. This skewness results in an imbalanced error distribution, which likely contributed to the failure of DOY 344 to achieve convergence. Although containing fewer outliers, the residuals for DOY 344 were systematically biased in the positive direction, leading to persistent directional errors that disrupted the overall fit.

In contrast, DOY 107's skewness values were closer to zero for most variables except for postfitL2 and postfitP3, indicating that the residuals were more symmetrically distributed around zero. Even in high kurtosis and extreme outliers, this symmetry in the residual distribution helped DOY 107 achieve convergence. Thus, not merely the presence or absence of outliers (as captured by kurtosis) but the overall symmetry of the residual distribution (skewness) plays a pivotal role in achieving precise horizontal accuracy. In comparing the post-fit residuals of DOY 107 and DOY 344, key differences emerge from the analysis of skewness and kurtosis, which impact their convergence to the 2.5 cm horizontal error. For both days, variables like postfitP2 and postfitL2 show negative skewness and high kurtosis (especially postfitL2, with kurtosis values exceeding 60 for DOY 107); however, for the postfitP1, postfitP3, and postfitL3 the skewness of the residuals for DOY 107 is minimal compared to DOY 344. The kurtosis value for the DOY 344 is minimal in all variables compared to DOY 107 except for the first frequency pseudorange. This analysis can help to conclude that kurtosis has minimal effects on horizontal error convergence.

The findings suggest that while kurtosis, which indicates the presence of an extreme and large number of outliers in one direction, can influence the stability of the residuals, its impact on convergence is secondary to skewness. A residual distribution with low skewness, even in high kurtosis, can still allow the model to converge to an accurate fit. Conversely, high skewness, particularly in key variables, can prevent convergence even when low kurtosis is present, as with DOY 344.

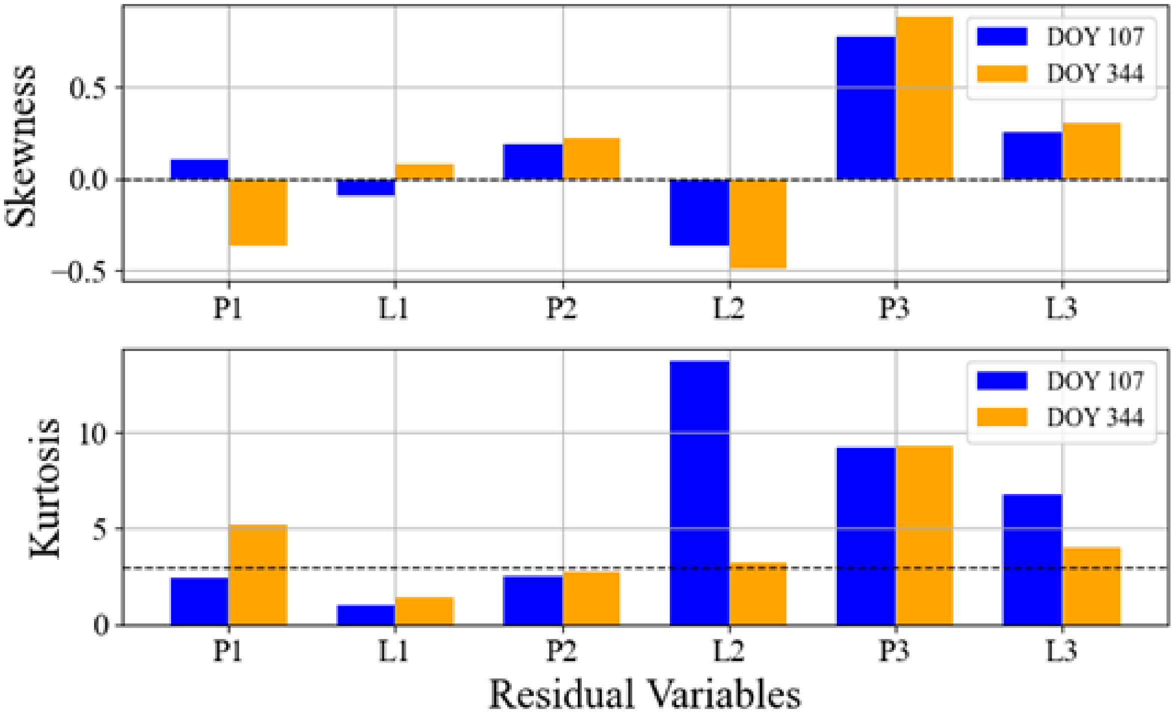

Figure 5.16: Skewness and kurtosis of post-fit residuals for different variables, comparing DOY 107 (blue) and DOY 344 (orange)

5.4.3 Resolved ambiguity solution analysis

Integer ambiguity resolution is a process that allows for higher precision in GNSS positioning by converting fractional cycle ambiguities into integer values. The success of this process is probabilistic in nature, as it relies on statistical techniques to validate the accuracy of the resolved ambiguities. This is because resolving ambiguities involves inherent uncertainties in measurements noise. By using statistical techniques, the probability of correct ambiguity resolution can be estimated, ensuring higher confidence in the results. Commonly used techniques include ratio tests, which compare the residuals of the best and second-best solutions to ensure reliability; validation tests, such as the F-test or Chi-square test, to confirm the consistency of the resolved ambiguities with the model; and bootstrapping, a method that repeatedly samples and estimates ambiguities to assess their stability. Resolving ambiguities is advantageous only when there is a strong likelihood that the estimated integer values are accurate. Consequently, the ambiguity success rate indicates the probability of accurately determining these integer ambiguities. Ratio tests, a commonly used statistical criterion in ambiguity resolution, validate whether the solution is robust by comparing the goodness-of-fit between competing integer candidates. Therefore, the ambiguity success rate captures how often the ambiguity resolution succeeds in various conditions. In PPP-AR, high ambiguity success rates directly correlate with faster convergence times and higher positional accuracy, as consistent success in resolving ambiguities minimizes errors (Teunissen, 2006). The accuracy of the GNSS solution relies not only on the success rate but also on the quality of the observations.

A high ambiguity success rate (often close to 1.0, or 100%) indicates that integer ambiguities are reliably resolved. This threshold signifies that the integer resolution process performs optimally under favorable conditions. In this study, the ambiguity resolution (AR) was not explicitly treated as a primary variable for adjustment or further modeling. However, the AR success rate was monitored as an output metric to evaluate the performance of the GNSS processing approach. While techniques like ratio testing and integer validation tests are common in the literature for evaluating AR reliability, the focus in this analysis was on observing the stability of the success rate over time to assess its impact on the convergence and overall accuracy of the GNSS solution.

Figure 5.17 presents the ambiguity success rates for two different DOYs, specifically DOY 344 in 2023 (left plot) and DOY 107 in 2024 (right plot). For DOY 344 (2023), the success rate shows considerable fluctuation, with several instances of pronounced drops below 0.9 and even reaching around 0.7 at certain points. According to the (Teunissen, 2006) theoretical framework, such drops in success rate could be due to suboptimal satellite geometry, adverse atmospheric conditions (such as increased ionospheric or tropospheric disturbances), or weaker signal-to-noise ratios. The inability of DOY 344 to maintain a stable ambiguity success rate throughout the period indicates challenges in achieving convergence to 2.5 cm positional accuracy. In contrast, DOY 107 (2024) presents a much more stable success rate, consistently remaining above 0.98 and nearing 1.0 for most of the period analyzed. This high and stable success rate suggests that ambiguity resolution was reliably achieved throughout the session. Consequently, DOY 107 successfully converges to the desired 2.5 cm accuracy threshold.

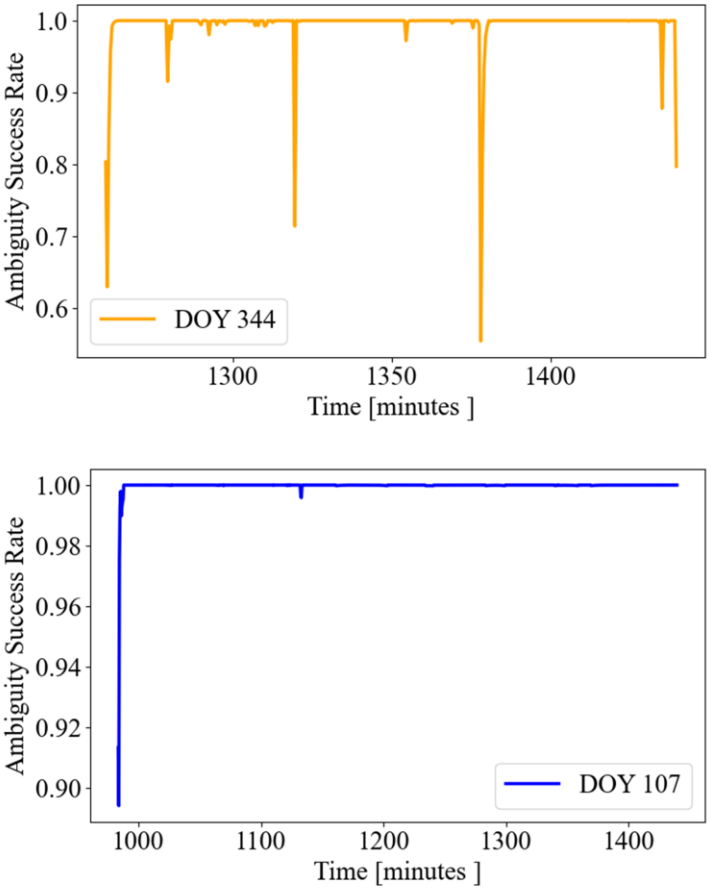

Figure 5.17: Ambiguity success rate for DOY 344, 2023(top), and DOY 107, 2024 (bottom)

Further, to analyze the fixed solution, the total number of successfully resolved satellites is counted per epoch and presented visually. A high number of resolved ambiguities will reduce the convergence time. Figure 5.18 illustrates the total number of fixed ambiguities and total number of processed over the observation period for DOY 344 in 2023 (top) and DOY 107 in 2024 (bottom). For DOY 344, the plot shows fluctuations in total number of fixed ambiguities, with values generally ranging from around 10 to 15, whereas the number rises to 15 to 18 for dataset DOY 107. There is a noticeable increase in fixed ambiguities around 22:00 on DOY 344, after which the number stabilizes to around 10-12 for a short period. This variability indicates intermittent challenges in consistently fixing ambiguities throughout the period. In contrast, DOY 107 exhibits a more stable number of fixed ambiguities, generally maintaining values between 15 and 20 throughout the observation period. Although minor fluctuations are present, they are less pronounced than those observed in DOY 344. The difference in the number of fixed ambiguities between DOY 344 and DOY 107 reflects their performance on convergence and accuracy, where DOY 344 did not converge to 2.5cm throughout the observation periods.

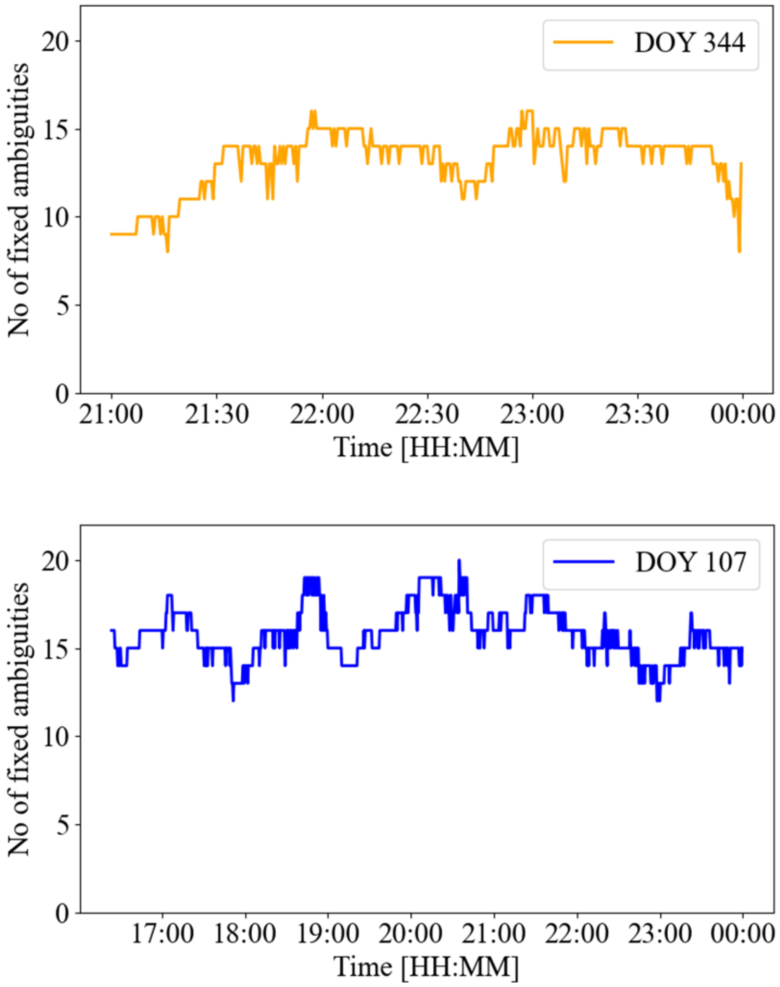

Figure 5.18: Total number of fixed ambiguities over the observation period for DOY 344, 2023 (top) and DOY 107, 2024 (bottom)

5.4.4 Number of satellites and position dilution of precision (PDOP)

The number of satellites and the PDOP indicate the spatial geometry of the GNSS solution. A well-distributed set of satellite signals strengthens the solution and improves the DOP. Figure 5.19 shows the number of processed satellites and the PDOP values over time for DOY 344 (2023) and DOY 107 (2024). The number of visible satellites is displayed in the top plot, with DOY 344 represented in blue and DOY 107 in orange. Throughout the observation period, DOY 107 consistently has a higher number of satellites, mostly staying above 25, whereas DOY 344 fluctuates more and generally maintains a lower satellite count, often between 20 and 25. The higher satellite visibility on DOY 107 indicates a stronger satellite geometry. The bottom plot shows the PDOP values for both DOY 344 and DOY 107. PDOP is a geometric measure of positioning precision, with lower values indicating stronger and more favourable satellite geometry. Throughout the observation period, DOY 107 (in orange) consistently maintains lower PDOP values, generally below 1.0 and rarely exceeding 1.25. In contrast, DOY 344 (in blue) shows a higher and more variable PDOP, frequently exceeding 1.0 and reaching peaks near 1.5. The higher PDOP values suggest a less optimal satellite geometry. The differences in satellite visibility and PDOP between DOY 344 and DOY 107 underscore their impact on convergence and positional accuracy. This finding explains the lower horizontal rms after convergence observed in DOY 344, 2023, compared to DOY 107, 2024 (Figure 5.8).

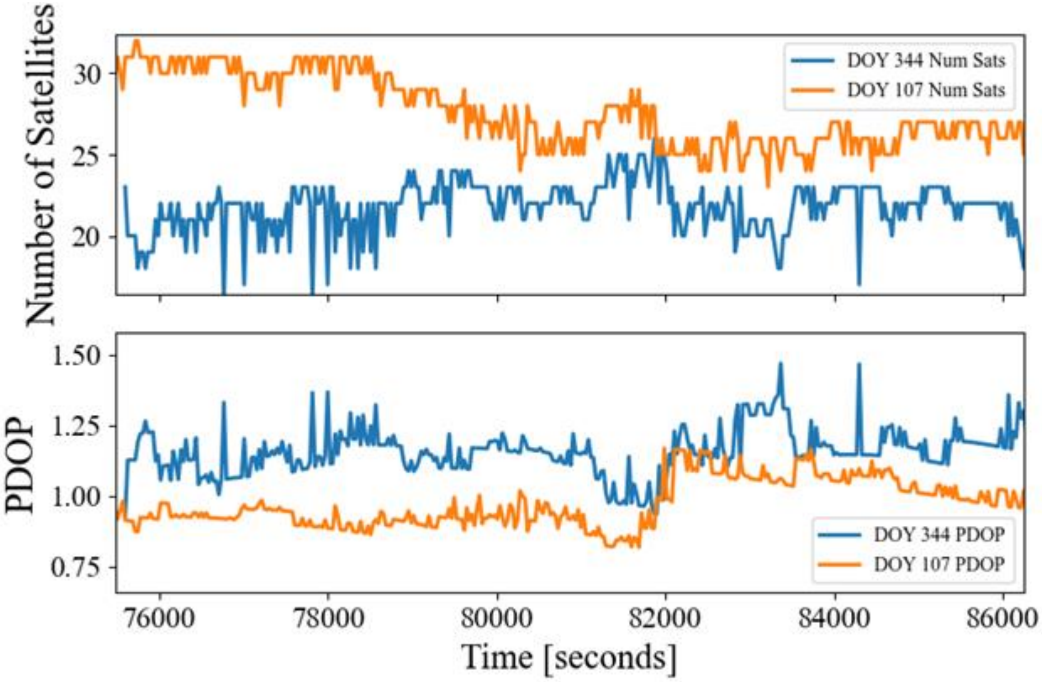

Figure 5.19: Number of satellites (top) and PDOP (bottom) for DOY 344, 2023 and DOY 107, 2024

5.5 Summary

This chapter compares the proposed C/N_0-based empirical model against two established weighting schemes: the elevation-based model and the analytical C/N_0-based model. The models are evaluated based on convergence time and root mean square error (rms) for horizontal and vertical positioning at the 100th, 95th, and 67th percentiles. The empirical model demonstrates substantial improvements, particularly in achieving fixed solutions for 5 cm horizontal accuracy by reducing convergence times by 71% at the 100th percentile. The empirical model consistently outperforms the elevation-based and analytical models, achieving successful convergence on multiple days where the other models failed for a 2.5 cm convergence threshold. Additionally, the empirical model processed more satellites and usually achieved lower PDOP values.

Seven of the analyzed datasets did not achieve the targeted 2.5 cm horizontal accuracy, while others successfully converged and hence, two datasets (DOY 344, 2023 and DOY 107, 2024) were chosen for detailed analysis. Summarizing the results from histogram distribution of standardized post-fit residuals plots (Figure 5.14) for post-fit residual comparison residuals for both DOY 107 and DOY 344 are largely centred around zero, though DOY 107 exhibits a narrower distribution. The Q-Q plots (Figure 5.15) show deviations from the reference line, especially in the tails, indicating that both datasets have non-normal distributions to varying extents. Deviations at the extremes (tails) suggest skewness and kurtosis, indicating that residuals might not be perfectly normally distributed. This deviation implies that the optimal estimation assumption of Gaussian residuals is not entirely met. The data shows positive and negative skewness across variables, notably higher for DOY 344 in postfitP3, indicating that the residuals have systematic biases (Figure 5.16). Low skewness is preferred for optimal estimation as it reflects symmetry in residual distribution. High kurtosis in certain residuals (especially postfitL2 for DOY 107) indicates the presence of outliers or heavy tails. While DOY 107 converged despite high kurtosis, this condition generally challenges optimal estimation since the assumption favours lower kurtosis (i.e., fewer outliers). Comparing these datasets reveals that factors such as satellite geometry, residual distribution, and ambiguity success rate significantly affect convergence and accuracy. The findings confirm that datasets with more consistent ambiguity resolution and optimal satellite configurations are better aligned with the assumptions of optimal estimation, resulting in improved convergence and accuracy.

Chapter 6 Conclusions and recommendations for future research

This chapter provides the concluding insights and recommendations derived from the research conducted in this study, which is organized into two main sections. The first section summarizes the key findings and conclusions from the analyses and results, while the second offers recommendations informed by these findings and suggests directions for future research. These sections present a comprehensive reflection on the study's outcomes and propose pathways for advancing knowledge and applications in this field.

6.1 Conclusions

This research investigates the potential of low-cost hardware as a cost-effective alternative for precise cm-positioning. A key finding of this study is that low-cost GNSS devices can achieve cm-level positioning accuracy when enhanced with suitable stochastic modelling techniques in an open-sky environment. These results highlight low-cost devices as viable solutions for budget-constrained applications and challenging terrain, such as mountainous areas, where RTK with geodetic hardware is prohibitively expensive. The study evaluates the performance of low-cost hardware against 2.5 cm and 5 cm accuracy thresholds, making it suitable for a wide range of applications. These applications include geodetic and cadastral surveying, scientific research and earth observations, autonomous systems in controlled environments, precision agriculture to fleet management and resources tracking, urban planning and utility management and many more.

Developing and implementing a novel C/N_0-based empirical weighting scheme effectively addresses the unique signal characteristics of low-cost GNSS devices, ensuring more accurate and reliable solutions. The proposed model improves convergence times and accuracy in a static medium multipath environment. However, its performance in more dynamic and high multipath environments such as urban canon remains uncertain. Further testing and potential adjustments are necessary to fully understand the model's applicability and reliability across diverse real-world scenarios. Overall, this research underscores the viability of low-cost GNSS technology as a powerful tool for cm-level accuracy, providing practical solutions that bridge technological and financial gaps, thereby enabling more inclusive and efficient applications across diverse industries.

6.1.1 Comparison between measurements from geodetic and low-cost hardware

The research highlights significant differences in measurement quality between low-cost and geodetic GNSS hardware. Key findings indicate that low-cost receivers consistently exhibit lower C/N_0 density ratios, averaging 4-10 dB Hz less than geodetic receivers across all GNSS frequencies. This discrepancy affects the performance, particularly at low elevation angles where noise and multipath interference are more pronounced. Low-cost receivers are significantly more susceptible to noise, with measurement noise levels 5-10 times higher than those of geodetic devices, and are highly impacted by multipath, experiencing errors up to three times greater. Furthermore, low-cost devices experience more cycle slips and substantial data gaps up to 16 times greater phase measurement gaps than geodetic devices. In conclusion, this research demonstrates notable differences in measurement quality between low-cost and geodetic GNSS hardware, with low-cost receivers facing considerable limitations in signal quality.

6.1.2 Observation weighting for low-cost hardware

Phase noise serves as a valuable indicator of measurement quality in GNSS, reflecting the inherent noise affecting carrier-phase measurements. Stochastic modelling leverages this indicator by assigning different weights to measurements based on noise levels. The analysis reveals a substantial impact of PLL bandwidth on phase noise in GNSS carrier-phase measurements, with marked differences between geodetic and low-cost receivers. The calculated standard deviation of carrier-phase lock loop noise, as shown in Table 4.2, confirms that phase noise remains minimal at narrow bandwidths (such as 0.2 Hz), typically below 0.5 mm, with negligible variation across frequencies L1, L2, and L5. However, as PLL bandwidth increases to levels commonly used by low-cost receivers (25 to 100 Hz), phase noise rises considerably, reaching up to 9.5 mm, or 2.5-5% of each frequency's wavelength. At these higher bandwidths, phase noise also varies more distinctly across frequencies, particularly between L1 and L5, due to differences in signal characteristics. In conclusion, while phase noise remains relatively consistent across L1, L2, and L5 at narrow bandwidths, it becomes more variable at wider PLL bandwidths. This suggests that phase noise, which is influenced by the C/N_0 density ratio, becomes frequency-dependent under high bandwidth conditions, underscoring the need for frequency-sensitive weighting in low-cost receivers that operate at broader bandwidths.

The code-minus-carrier (CMC) analysis reveals that the C/N_0 is a more consistent indicator of measurement noise, especially at lower elevation angles. A moderate negative correlation exists between noise and C/N_0, whereas noise shows almost no correlation with elevation at lower angles. However, at higher elevation angles, the negative correlations of noise with both C/N_0 and elevation become more similar. Additionally, the distribution of C/N_0 between geodetic and low-cost hardware shows significant differences. The maximum observed C/N_0 in low-cost measurements is around 50 dB Hz, approximately 10 dB Hz lower than that by geodetic receivers at a 60^{0}-90^{0} elevation range. In contrast, low-cost receivers show a minimum C/N_0 of about 30 dB Hz at these elevations, whereas geodetic receivers maintain a minimum of around 50 dB Hz.

Analyzing the C/N_0 density distribution of low-cost hardware measurements, this research introduces a C/N_0-based empirical weighting scheme to improve GNSS data processing for low-cost receivers. This scheme strategically assigns lower weights to signals with C/N_0 values below the 44 dB Hz threshold. The distribution analysis shows that most signals from low-cost receivers fall within the 40-50 dB Hz range, unlike geodetic hardware, which more frequently captures stronger signals above 50 dB Hz. The empirical model's focus on mid-range C/N_0 values (30-50 dB Hz) ensures weaker signals are not entirely excluded.

6.1.3 Assessment of a C/N_0-based empirical stochastic model

The comparative analysis between the proposed C/N_0-based empirical model with elevation-based and C/N_0-based analytical stochastic model reveals that the proposed model consistently outperforms both models across convergence time and horizontal and vertical rms. In terms of convergence, the empirical model achieves a 71% reduction from float to fixed solutions at the 100th percentile and an 84.1% improvement at the 95th percentile for the 5 cm horizontal accuracy. Further analysis of convergence time for achieving 2.5 cm horizontal accuracy underscores that on certain days, the empirical model was the only model capable of achieving cm-level performance across all percentiles, providing convergence times where the other models failed to produce results at similar levels. Summarizing the model's performance, the C/N_0-based empirical model showed greater improvement than other models in achieving 5 cm horizontal accuracy compared to 2.5 cm horizontal accuracy. The model also demonstrates superior performance under varying satellite geometry, with consistently lower PDOP values.

Extensive research was conducted to compare the performance of datasets that did not converge at all to 2.5 cm horizontal accuracy. The study identified key factors contributing to this issue: asymmetrical residual distributions, lower ambiguity resolution success rates, and suboptimal satellite geometry. For instance, datasets such as DOY 344 exhibited positively skewed residuals, and ambiguity resolution success rates frequently dropped below 90% and high PDOP values further contributed to weaker spatial geometry.

6.2 Recommendations

Based on the insights gained from this study, several recommendations are proposed to enhance the practical applications of low-cost GNSS technology and address the current model's identified limitations. These recommendations aim to improve the model's robustness, adaptability, and accuracy in a variety of real-world scenarios, including dynamic environments and challenging signal conditions. By implementing these recommendations, future work can build on the strengths of the proposed model, broadening its applicability for diverse applications. Additionally, these suggestions offer a pathway for refining low-cost GNSS solutions, making them even more viable as accessible, cost-effective alternatives to high-end geodetic systems.

6.2.1 Comparative analysis of signal quality in diverse environments

This research was conducted in a medium multipath environment using static data. Expanding testing to various multipath environments would yield valuable insights into hardware performance, enhancing understanding of the strengths and limitations of low-cost hardware. Additionally, extending the study to include kinematic scenarios would provide valuable insights into the performance of low-cost hardware under dynamic conditions. Comprehensive field testing across diverse and challenging terrains such as dense urban areas, forests, and mountainous regions would further enhance understanding of low-cost GNSS performance. This broader testing approach could reveal specific conditions where low-cost receivers excel and highlight areas where improvements are necessary.

6.2.2 Data-driven robust quality control

Future research could explore integrating density-based spatial clustering of applications with noise (DBSCAN) to analyze pre- and post-residuals from least squares adjustment filters. By leveraging DBSCAN's ability to detect patterns and isolate noise, dynamic, real-time post-fit rejection thresholds could be developed, allowing for more adaptive filtering and enhancing the accuracy of the adjustment process. This approach would enable more effective identification and rejection of outliers, adapting threshold levels based on current signal characteristics, thereby refining the reliability and precision of PPP-AR solutions in varying conditions.

6.2.3 Testing C/N_0 based-empirical model on various multipath environments

While the current research demonstrates the effectiveness of the proposed C/N_0-based empirical model in open-sky conditions, further studies should test the model across a range of multipath environments, including urban, forested, and mountainous regions. Evaluating the model's performance in these varied settings would allow for targeted stochastic adjustments that account for specific environmental characteristics, such as increased signal reflections in urban areas or canopy interference in forested regions. This testing would help identify the conditions under which the C/N_0-based model remains robust and situations where additional model adaptations may be necessary. Moreover, testing in diverse environments would provide insights into the model's flexibility and help refine weighting strategies for low-cost GNSS applications in challenging terrains, enhancing the model's adaptability and reliability across a broader spectrum of real-world conditions.

6.2.4 Partial ambiguity resolution (AR)

Given the variability in ambiguity resolution success rates, particularly on non-converging days, as presented in the analysis, future research could focus on implementing partial ambiguity resolution (AR) techniques for low-cost GNSS measurements. Unlike full AR, partial AR resolves only a subset of ambiguities with high confidence, enabling quicker convergence and improved positional accuracy when complete ambiguity resolution proves challenging. This approach can be especially valuable in environments with poor satellite geometry or low signal quality, where full AR might be impractical.

6.2.5 Enhancing partial PPP-AR with predictive ML approaches

Incorporating machine learning (ML) models could offer a significant advantage over the proposed empirical C/N0-based model. While the empirical model effectively enhances accuracy and convergence times by weighting signals based on carrier-to-noise density ratios, it relies on predefined thresholds and static rules that may not fully capture the dynamic nature of real-world GNSS environments. A machine learning approach, in contrast, could introduce a more adaptable and predictive layer to the ambiguity resolution process, optimizing performance across a broader range of conditions.

Machine learning models, such as decision trees, support vector machines (SVMs), or neural networks, could be trained on historical GNSS data to identify patterns and conditions under which partial AR will likely succeed. By analyzing factors like PDOP, C/N_0 values, satellite elevation angles, and environmental variables (e.g., multipath levels), an ML model could learn to predict the likelihood of successful ambiguity resolution. Once trained, the model could dynamically adjust weighting and resolution strategies based on real-time inputs, allowing the GNSS system to respond more effectively to varying signal conditions. Historical GNSS datasets with labelled outcomes (e.g., successful or unsuccessful ambiguity resolution under specific conditions) would be required to train the ML model, which can be challenging. Additionally, the model must be periodically retrained with new data to adapt to evolving GNSS conditions and satellite configurations.

6.2.6 Potential for combining weighting schemes for low-cost measurements

While the research demonstrates the advantages of the C/N_0-based empirical weighting scheme, there is potential to enhance further its effectiveness by exploring hybrid approaches that combine the strengths of different weighting schemes. Combining C/N_0-based empirical and elevation-based weighting will be a hybrid model which could leverage the proposed scheme's ability to handle mid-range signal strengths while incorporating elevation-based weighting to prioritize higher-elevation satellites, which typically have fewer errors. Hybrid approaches have the potential to mitigate the limitations of any single scheme, offering a versatile solution that performs well across diverse environments. Future research should explore the feasibility of such combinations while expanding testing to include dynamic and high-multipath scenarios.

References

Aggrey, J., Bisnath, S., Naciri, N., Shinghal, G., & Yang, S. (2019). *Accuracy Trend Analysis of Low-cost GNSS Chips: The Case of Multi-constellation GNSS PPP*. 3618–3635. https://doi.org/10.33012/2019.16971

Aggrey, J. E. (2015). *Multi-GNSS precise point positioning software architecture and analysis of GLONASS pseudorange biases* [MSc Thesis, York University]. https://yorkspace.library.yorku.ca/xmlui/bitstream/handle/10315/29969/Aggrey_John_E_2014_Masters.pdf?sequence=2&isAllowed=y

Amielh, C., Chabory, A., Macabiau, C., & Azoulai, L. (2017). *Validation of Existing GNSS Multipath Model*. 1772–1789. https://doi.org/10.33012/2017.15119

Arinc Research Corporation. (1993). *Navstar GPS Space Segment / Navigation User Interfaces* (No. ICD-GPS-2000, Revision C). GPS Joint Program Office, Space and Missile Systems Center, U.S. Air Force. https://www.gps.gov/technical/icwg/ICD-GPS-200C.pdf

Ashby, N. (2003). Relativity in the Global Positioning System. *Living Reviews in Relativity*, *6*(1), 1. https://doi.org/10.12942/lrr-2003-1

Banville, S., Lachapelle, G., Ghoddousi-Fard, R., & Gratton, P. (2019). Automated processing of low-cost GNSS receiver data. *32nd International Technical Meeting of the Satellite Division of The Institute of Navigation (ION GNSS+ 2019)*, 3636–3652. https://doi.org/10.33012/2019.16972

Bischoff, W., Heck, B., Howind, J., & Teusch, A. (2005). A procedure for testing the assumption of homoscedasticity in least squares residuals: A case study of GPS carrier-phase observations. *Journal of Geodesy*, *78*(7–8), 397–404. https://doi.org/10.1007/s00190-004-0390-5

Blewitt, G. (1990). An Automatic Editing Algorithm for GPS data. *Geophysical Research Letters*, *17*(3), 199–202. https://doi.org/10.1029/GL017i003p00199

Braasch, M. S., & van Dierendonck, A. J. (1999). GPS receiver architectures and measurements. *Proceedings of the IEEE*, *87*(1), 48–64. Proceedings of the IEEE. https://doi.org/10.1109/5.736341

Brodin, G., & Daly, P. (1998). GNSS code and carrier tracking in the presence of multipath. *International Journal of Satellite Communications*, *15*(1), 25–34. https://doi.org/10.1002/(sici)1099-1247(199701)15:1<25::aid-sat565>3.0.co;2-f

Brown, A. K., & Mathews, B. (2005). GPS Multipath Mitigation Using a Three Dimensional Phased Array. *Proceedings of the 18th International Technical Meeting of the Satellite Division of The Institute of Navigation (ION GNSS 2005)*, 659–666. http://www.ion.org/publications/abstract.cfm?jp=p&articleID=6260

Brunner, F. K., Hartinger, H., & Troyer, L. (1999). GPS signal diffraction modelling: The stochastic SIGMA-δ model. *Journal of Geodesy*, *73*(5), 259–267. https://doi.org/10.1007/s001900050242

Caamano, M., Crespillo, O. G., Gerbeth, D., & Grosch, A. (2020). Detection of GNSS Multipath with Time-Differenced Code-Minus-Carrier for Land-Based Applications. *2020 European Navigation Conference (ENC)*, 1–12. https://doi.org/10.23919/ENC48637.2020.9317340

Calian. (2023). TW7972 Triple Band GNSS Antenna with L-band. *Calian Advanced Technologies*. https://www.calian.com/advanced-technologies/gnss_product/tw7972-triple-band-gnss-antenna-with-l-band/https://www.calian.com/advanced-technologies/gnss_product/tw7972-triple-band-gnss-antenna-with-l-band/

Calian. (2024). GNSS Antenna Radio Frequency Characteristics. *Calian Advanced Technologies*. https://www.calian.com/advanced-technologies/gnss/information-support/gnss-antenna-radio-frequency-characteristics/

Chang, X. W., Yang, X., & Zhou, T. (2005). MLAMBDA: A modified LAMBDA method for integer least-squares estimation. *Journal of Geodesy*, *79*(9), 552–565.

Chen, K. (2004). *Real-Time Precise Point Positioning and Its Potential Applications*. 1844–1854. http://www.ion.org/publications/abstract.cfm?jp=p&articleID=5868

Chen, X., Dovis, F., Peng, S., & Morton, Y. (2013). Comparative Studies of GPS Multipath Mitigation Methods Performance. *IEEE Transactions on Aerospace and Electronic Systems*, *49*(3), 1555–1568. https://doi.org/10.1109/TAES.2013.6558004

Choy, S. (2009). *An investigation into the accuracy of single frequency Precise Point Positioning (PPP)* [PhD Dissertation, RMIT University]. https://researchbank.rmit.edu.au/eserv/rmit:6635/Choy.pdf

Collins, & Langley. (1999). *Possible weighting schemes for GPS carrier phase observations in the presence of multipath*. By Geodetic Research Laboratory, Department of Geodesy and Geomatics Engineering, University of New Brunswick, & The United States Army Corps of Engineers Topographic Engineering Center. http://gauss.gge.unb.ca/papers.pdf/acereport99.pdf

Collins, P., Lahaye, F., Heroux, P., & Bisnath, S. (2008). Precise point positioning with ambiguity resolution using the decoupled clock model. *Proceedings of the 21st International Technical Meeting of the Satellite Division of the Institute of Navigation (ION GNSS 2008)*, 1315–1322. http://www.ion.org/search/view_abstract.cfm?jp=p&idno=8043

Cui, Y., Meng, X., Chen, Q., Gao, Y., Xu, C., Roberts, S., & Wang, Y. (2017). Feasibility analysis of low-cost GNSS receivers for achieving required positioning performance in CAV applications. *2017 Forum on Cooperative Positioning and Service (CPGPS）*, 355–361. https://doi.org/10.1109/CPGPS.2017.8075154

De Bakker, P. F., Van Der Marel, H., & Tiberius, C. C. J. M. (2009). Geometry-free undifferenced, single and double differenced analysis of single frequency GPS, EGNOS and GIOVE-A/B measurements. *GPS Solutions*, *13*(4), 305–314. https://doi.org/10.1007/s10291-009-0123-6

Deng, Z., Nischan, T., & Bradke, M. (2017). Multi-GNSS Rapid Orbit-, Clock- & EOP-Product Series. *GFZ Data Services*. https://doi.org/10.5880/GFZ.1.1.2017.002

Dow, J. M., Neilan, R. E., & Rizos, C. (2009). The international GNSS service in a changing landscape of global navigation satellite systems. *Journal of Geodesy*, *83*(3–4), 191–198.

Erker, S., Thölert, S., Furthner, J., Meurer, M., & Häusler, M. (2009). *GPS L5 "Light's on!"—A First Comprehensive Signal Verification and Performance Analysis*. 1544–1551. http://www.ion.org/publications/abstract.cfm?jp=p&articleID=8562

Everett, T., Taylor, T., Lee, D.-K., & Akos, D. M. (2022). Optimizing the Use of RTKLIB for Smartphone-Based GNSS Measurements. *Sensors*, *22*(10), 3825. https://doi.org/10.3390/s22103825

Falco, G., Gutiérrez, M. C.-C., Serna, E. L., Zacchello, F., & Bories, S. (2014). *Low-cost Real-time Tightly-coupled GNSS/INS Navigation System Based on Carrier Phase Double Differences for UAV Applications*. 841–857. http://www.ion.org/publications/abstract.cfm?jp=p&articleID=12422

Gao, Y., & Shen, X. (2002). A New Method for Carrier-Phase-Based Precise Point Positioning. *Navigation*, *49*(2), 109–116. https://doi.org/10.1002/j.2161-4296.2002.tb00260.x

Ge, M., Gendt, G., Rothacher, M., Shi, C., & Liu, J. (2008). Resolution of GPS carrier-phase ambiguities in Precise Point Positioning (PPP) with daily observations. *Journal of Geodesy*, *82*(7), 389–399. https://doi.org/10.1007/s00190-007-0187-4

Geng, J., Teferle, F. N., Meng, X., & Dodson, A. H. (2011). Towards PPP-RTK: Ambiguity resolution in real-time precise point positioning. *Advances in Space Research*, *47*(10), 1664–1673. https://doi.org/10.1016/j.asr.2010.03.030

GNSS, I. (2016, November 13). Satellite Selection. *Inside GNSS - Global Navigation Satellite Systems Engineering, Policy, and Design*. https://insidegnss.com/satellite-selection/

Griffiths, J., & Ray, J. R. (2009). On the precision and accuracy of IGS orbits. *Journal of Geodesy*, *83*(3–4), 277–287. https://doi.org/10.1007/s00190-008-0237-6

Hamza, V., Stopar, B., Ambrožič, T., & Sterle, O. (2021). Performance Evaluation of Low-Cost Multi-Frequency GNSS Receivers and Antennas for Displacement Detection. *Applied Sciences*, *11*(14), 6666. https://doi.org/10.3390/app11146666

Hamza, V., Stopar, B., Sterle, O., & Pavlovčič-Prešeren, P. (2023). Low-Cost Dual-Frequency GNSS Receivers and Antennas for Surveying in Urban Areas. *Sensors*, *23*(5), 2861. https://doi.org/10.3390/s23052861

Hamza, V., Stopar, B., Sterle, O., & Pavlovčič-Prešeren, P. (2024). Observations and positioning quality of low-cost GNSS receivers: A review. *GPS Solutions*, *28*(3), 149. https://doi.org/10.1007/s10291-024-01686-8

Hartinger, H., & Brunner, F. K. (1999). Variances of GPS Phase Observations: The SIGMA Model. *GPS Solutions*, *2*(4), 35–43. https://doi.org/10.1007/PL00012765

Héroux, P., & Kouba, J. (2001). GPS precise point positioning using IGS orbit products. *Physics and Chemistry of the Earth, Part A: Solid Earth and Geodesy*, *26*(6–8), 573–578. https://doi.org/10.1016/S1464-1895(01)00103-X

Hexagon | NovAtel. (2020). *G-III Reference Receiver*. G-III Reference Receiver. https://hexagondownloads.blob.core.windows.net/public/Novatel/assets/Documents/Papers/WAAS-G-III-Receiver/G-III-Reference-Receiver-Product-Sheet.pdf

Hexagon | NovAtel. (2023, April 27). *GNSS-850 Product Sheet (D21528 Version 5)*. Hexagon AB. https://hexagondownloads.blob.core.windows.net/public/Novatel/assets/Documents/Papers/GNSS-850-Product-Sheet/GNSS-850-Product-Sheet.pdf

Hofmann-Wellenhof, B., Lichtenegger, H., & Wasle, E. (2007). *GNSS–global navigation satellite systems: GPS, GLONASS, Galileo, and more*. Springer Science & Business Media.

Hohensinn, R., Stauffer, R., Glaner, M. F., Herrera Pinzón, I. D., Vuadens, E., Rossi, Y., Clinton, J., & Rothacher, M. (2022). Low-Cost GNSS and Real-Time PPP: Assessing the Precision of the u-blox ZED-F9P for Kinematic Monitoring Applications. *Remote Sensing*, *14*(20), 5100. https://doi.org/10.3390/rs14205100

Hopfield, H. S. (1969). Two-quartic tropospheric refractivity profile for correcting satellite data. *Journal of Geophysical Research (1896-1977)*, *74*(18), 4487–4499. https://doi.org/10.1029/JC074i018p04487

Hou, H., Kuang, C., Zhou, Y., & Zhang, Y. (2018). Feasibility Study of Low Cost Receiver for Deformation Monitoring. In J. Sun, C. Yang, & S. Guo (Eds.), *China Satellite Navigation Conference (CSNC) 2018 Proceedings* (Vol. 497, pp. 129–138). Springer Singapore. https://doi.org/10.1007/978-981-13-0005-9_11

Hu, J., Li, P., & Bisnath, S. (2024). Enhancing smartphone precise point positioning to sub-meter accuracy in suburban environments: A new stochastic model and outlier diagnosis. *GPS Solutions*, *28*(3), 112. https://doi.org/10.1007/s10291-024-01651-5

IGS. (2024). *About*. International GNSS Service. http://www.igs.org/about/analysis-centers

Kim, D., Serrano, L., & Langley, R. B. (2005). *Compensation of the Effects of Phase Wind-up for Improving the Performance of a GPS RTK-Based Vehicle Navigation System*. 9.

Kouba, J. (2009a). *A guide to using International GNSS Service (IGS) products*. ftp://ftp.igs.org/pub/resource/pubs/UsingIGSProductsVer21.pdf

Kouba, J. (2009b). Testing of global pressure/temperature (GPT) model and global mapping function (GMF) in GPS analyses. *Journal of Geodesy*, *83*(3–4), 199–208. https://doi.org/10.1007/s00190-008-0229-6

Krzan, G., Dawidowicz, K., & Paziewski, J. (2024). Low-cost GNSS antennas in precise positioning: A focus on multipath and antenna phase center models. *GPS Solutions*, *28*(3), 103. https://doi.org/10.1007/s10291-024-01645-3

Kumar, A., Achanta, D., Mondal, A., & Kamatham, Y. (2010). A Wide Band Antenna for Multi-Constellation Gnss and Augmentation Systems. *Progress In Electromagnetics Research M*, *11*, 65–77. https://doi.org/10.2528/PIERM09100304

Laurichesse, D., & Blot, A. (2016). Fast PPP Convergence Using Multi-Constellation and Triple-Frequency Ambiguity Resolution. *Proceedings of the 29th International Technical Meeting of The Satellite Division of the Institute of Navigation (ION GNSS+ 2016)*, 2082–2088.

Laurichesse, D., Mercier, F., Berthias, J.-P., Broca, P., & Cerri, L. (2009). Integer ambiguity resolution on undifferenced GPS phase measurements and its application to PPP and satellite precise orbit determination. *Navigation*, *56*(2), 135–149.

Leclère, J., Landry, R., & Botteron, C. (2018). Comparison of L1 and L5 Bands GNSS Signals Acquisition. *Sensors*, *18*(9), 2779. https://doi.org/10.3390/s18092779

Leick, A., Rapoport, L., & Tatarnikov, D. (2015). *GPS satellite surveying* (4th ed). John Wiley & Sons.

Li, B., Shen, Y., & Xu, P. (2008). Assessment of stochastic models for GPS measurements with different types of receivers. *Science Bulletin*, *53*(20), 3219–3225. https://doi.org/10.1007/s11434-008-0293-6

Li, Y., Zhang, Z., He, X., Yuan, H., & Zang, N. (2023). An elevation stochastic model constrained by C/N $_0$ for GNSS real-time kinematic positioning in harsh environments. *Measurement Science and Technology*, *34*(1), 015011. https://doi.org/10.1088/1361-6501/ac900d

Luo, X., Mayer, M., & Heck, B. (2009). Improving the stochastic model of GNSS observations by means of SNR-based weighting. In *Observing our Changing Earth* (pp. 725–734). Springer. http://link.springer.com/chapter/10.1007/978-3-540-85426-5_83

Marut, G., Hadas, T., & Nosek, J. (2024). Intercomparison of multi-GNSS signals characteristics acquired by a low-cost receiver connected to various low-cost antennas. *GPS Solutions*, *28*(2), 82. https://doi.org/10.1007/s10291-024-01628-4

McCarthy, D. D., Petit, G., & International Earth Rotation and Reference Systems Service (Eds.). (2004). *IERS Conventions (2003)*. Verl. des Bundesamtes für Kartographie und Geodäsie.

Miletiev, R., Petkov, P. Z., Yordanov, R., & Brusev, T. (2024). Study of Global Navigation Satellite System Receivers' Accuracy for Unmanned Vehicles. *Sensors*, *24*(18), 5909. https://doi.org/10.3390/s24185909

Ministry of Natural Resources, Canada. (2024, January 26). *Ontario specification for Global Navigation Satellite Systems (GNSS)*. http://www.ontario.ca/page/ontario-specification-global-navigation-satellite-systems-gnss-geodetic-control-surveys

Mosaic-CLAS GNSS. (2024). https://www.septentrio.com/en/products/gnss-receivers/gnss-receiver-modules/mosaic-clas

Naciri, N., & Bisnath, S. (2021). An uncombined triple-frequency user implementation of the decoupled clock model for PPP-AR. *Journal of Geodesy*, *95*(5), 60. https://doi.org/10.1007/s00190-021-01510-y

Naciri, N., & Bisnath, S. (2023). *RTK-Quality Positioning with Global Precise Point Positioning Corrections*. 2546–2562. https://doi.org/10.33012/2022.18432

Nguyen, N. V., Cho, W., & Hayashi, K. (2021). Performance evaluation of a typical low-cost multi-frequency multi-GNSS device for positioning and navigation in agriculture – Part 1: Static testing. *Smart Agricultural Technology*, *1*, 100004. https://doi.org/10.1016/j.atech.2021.100004

Prange, L., Villiger, A., Sidorov, D., Schaer, S., Beutler, G., Dach, R., & Jäggi, A. (2020). Overview of CODE's MGEX solution with the focus on Galileo. *Advances in Space Research*, *66*(12), 2786–2798. https://doi.org/10.1016/j.asr.2020.04.038

Ramachandran, D., Din, A. H. M., Ibrahim, S. A., & Omar, A. H. (2019). Real-Time Precise Point Positioning (RT-PPP) for Positioning and Mapping. In B. Pradhan (Ed.), *GCEC 2017* (Vol. 9, pp. 891–913). Springer Singapore. https://doi.org/10.1007/978-981-10-8016-6_64

Romero-Andrade, R., Trejo-Soto, M. E., Vega-Ayala, A., Hernández-Andrade, D., Vázquez-Ontiveros, J. R., & Sharma, G. (2021). Positioning Evaluation of Single and Dual-Frequency Low-Cost GNSS Receivers Signals Using PPP and Static Relative Methods in Urban Areas. *Applied Sciences*, *11*(22), 10642. https://doi.org/10.3390/app112210642

Sanz Subirana, J., Juan Zornoza, J. M., & Hernández-Pajares, M. (2011). *Combination of GNSS Measurements*. https://gssc.esa.int/navipedia/index.php/Combination_of_GNSS_Measurements

Schmid, R., Dach, R., Collilieux, X., Jäggi, A., Schmitz, M., & Dilssner, F. (2016). Absolute IGS antenna phase center model igs08.atx: Status and potential improvements. *Journal of Geodesy*, *90*(4), 343–364. https://doi.org/10.1007/s00190-015-0876-3

Schmid, R., Steigenberger, P., Gendt, G., Ge, M., & Rothacher, M. (2007). Generation of a consistent absolute phase-center correction model for GPS receiver and satellite antennas. *Journal of Geodesy*, *81*(12), 781–798. https://doi.org/10.1007/s00190-007-0148-y

Seepersad, G. (2012). *Reduction of initial convergence period in GPS PPP data processing* [York University]. https://yorkspace.library.yorku.ca/server/api/core/bitstreams/862ec63b-8d29-4d0d-bd4b-cb030d29c033/content

Sennott, J. W. (1999). Receiver Architectures for Improved Carrier Phase Tracking in Atenuation, Blockage, and Interference. *GPS Solutions*, *3*(2), 40–47. https://doi.org/10.1007/PL00012790

Septentrio. (2020, December 3). *Mosaic-X5 Reference Guide*. https://media.digikey.com/pdf/Data%20Sheets/Septentrio%20PDFs/Mosaic-x5_Firmware_v4.8.2_Reference_Guide.pdf

Septentrio, M. (n.d.). *Mosaic-X5*. Retrieved June 10, 2021, from https://www.septentrio.com/en/products/gnss-receivers/rover-base-receivers/receivers-modules/mosaic

Shinghal, G., & Bisnath, S. (2021). Conditioning and PPP processing of smartphone GNSS measurements in realistic environments. *Satellite Navigation*, *2*(1), 1–17.

Skylark Cx | Swiftnav. (2024). https://www.swiftnav.com/skylark-cx

Strode, P. R. R., & Groves, P. D. (2015). GNSS multipath detection using three-frequency signal-to-noise measurements. *GPS Solutions*. https://doi.org/10.1007/s10291-015-0449-1

Tetewsky, A. K., & Mullen, F. E. (1993). Effects of antenna orientation on GPS carrier phase. *Manuscripta Geodaetica*, *18*(2), 91–98. https://doi.org/10.1007/BF03655303

Teunissen. (1994). *Integer least-squares estimation of the GPS phase Ambiguities*. International Symposium on Kinematic Systems in Geodesy, Geomatics and navigation, Benff, Alberta, canada. https://gnss.curtin.edu.au/wp-content/uploads/sites/21/2016/04/Teunissen1994Integer.pdf

Teunissen, & Amiri-Simkooei, A. R. (2008). Least-squares variance component estimation. *Journal of Geodesy*, *82*(2), Article 2. https://doi.org/10.1007/s00190-007-0157-x

Teunissen, & Montenbruck, O. (Eds.). (2017). *Springer Handbook of Global Navigation Satellite Systems*. Springer International Publishing. https://doi.org/10.1007/978-3-319-42928-1

Teunissen, P. J. G. (2000). *On the GNSS integer ambiguity success rate*. 10–108. https://gnss.curtin.edu.au/wp-content/uploads/sites/21/2016/04/Teunissen2000GNSS.pdf

Teunissen, P. J. G. (2007). Influence of ambiguity precision on the success rate of GNSS integer ambiguity bootstrapping. *Journal of Geodesy*, *81*(5), 351–358. https://doi.org/10.1007/s00190-006-0111-3

Teunissen, P. J. G., & Kleusberg, A. (Eds.). (1998). *GPS for Geodesy*. Springer. https://doi.org/10.1007/978-3-642-72011-6

Teunissen, P. J. G., & Montenbruck, O. (Eds.). (2017). *Springer Handbook of Global Navigation Satellite Systems*. Springer International Publishing. https://doi.org/10.1007/978-3-319-42928-1

Teunissen, P. J., Odijk, D., & Zhang, B. (2010). PPP-RTK: Results of CORS network-based PPP with integer ambiguity resolution. *Journal of Aeronautics, Astronautics and Aviation, Series A*, *42*(4), 223–230.

The SciPy Community. (2014). *Scipy.stats.pearsonr*. SciPy Documentation. https://docs.scipy.org/doc/scipy/reference/generated/scipy.stats.pearsonr.html

Tiberius, C. C. J. M., & Kenselaar, F. (2000). ESTIMATION OF THE STOCHASTIC MODEL FOR GPS CODE AND PHASE OBSERVABLES. *Survey Review*, *35*(277), 441–454. https://doi.org/10.1179/sre.2000.35.277.441

Tunini, L., Zuliani, D., & Magrin, A. (2022). Applicability of Cost-Effective GNSS Sensors for Crustal Deformation Studies. *Sensors*, *22*(1), 350. https://doi.org/10.3390/s22010350

u-blox. (2022). *PointPerfect: GNSS augmentation service*. https://www.u-blox.com/en/product/pointperfect

van Diggelen, F. (1997). *GPS and GPS+GLONASS RTK*. 139–144. http://www.ion.org/publications/abstract.cfm?jp=p&articleID=2744

Wielgocka, N., Hadas, T., Kaczmarek, A., & Marut, G. (2021). Feasibility of Using Low-Cost Dual-Frequency GNSS Receivers for Land Surveying. *Sensors*, *21*(6), 1956. https://doi.org/10.3390/s21061956

Wieser, A., & Brunner, F. K. (2014). An extended weight model for GPS phase observations. *Earth, Planets and Space*, *52*(10), 777–782. https://doi.org/10.1186/BF03352281

Willi, D., Meindl, M., Xu, H., & Rothacher, M. (2018). GNSS antenna phase center variation calibration for attitude determination on short baselines. *NAVIGATION: Journal of the Institute of Navigation*, *65*(4), 643–654. https://doi.org/10.1002/navi.273

Wu, Y., Liu, Y., Yi, W., & Ge, H. (2021). Impact of elevation mask on multi-GNSS precise point positioning performance. *Earth Science Informatics*, *14*. https://doi.org/10.1007/s12145-021-00619-0

Yuan, H., Zhang, Z., He, X., Li, G., & Wang, S. (2022). Stochastic model assessment of low-cost devices considering the impacts of multipath effects and atmospheric delays. *Measurement*, *188*, 110619. https://doi.org/10.1016/j.measurement.2021.110619

Zumberge, J. F., Heflin, M. B., Jefferson, D. C., Watkins, M. M., & Webb, F. H. (1997). Precise point positioning for the efficient and robust analysis of GPS data from large networks. *Journal of Geophysical Research: Solid Earth (1978–2012)*, *102*(B3), 5005–5017. https://doi.org/10.1029/96JB03860